Addis Ababa University
School of Graduate Studies

Dynamics of carbon dioxide flux over Africa: Insight from observations and model simulations

by
Anteneh Getachew Mengistu
Supervisor: Prof. Gizaw Mengistu Tsidu

A Dissertation Submitted to the School of Graduate Studies of the Addis Ababa University in Partial Fulfillment of the Requirements for the Degree of Doctor of Philosophy in Atmospheric Physics

Addis Ababa, Ethiopia

December 29, 2020

Declaration of Authorship

I, Anteneh Getachew Mengistu, declare that this thesis titled, “Dynamics of carbon dioxide flux over Africa: Insight from observations and model simulations” and the work presented in it are my own. I confirm that:

- This dissertation was done for the partial fulfillment of the requirements for the doctoral degree at the Addis Ababa University.
- This dissertation represents my own work and has not been previously included in a dissertation or thesis submitted to this university or any other institution for a diploma, degree or any other qualification.
- Where I have quoted from the work of others, the source is always given. Except for such quotations, this thesis is entirely my work.
- I have acknowledged all of the main sources of help.
- Where any part of this dissertation is based on work done by myself jointly with others, I have clearly stated what was contributed by others and what I have done myself.

Signed:

Date:

Addis Ababa University
School of Graduate Studies

Dynamics of carbon dioxide flux over Africa: Insight from observations and model simulations

by
Anteneh Getachew Mengistu

A Dissertation Submitted to the School of Graduate Studies of the Addis Ababa University in Partial Fulfillment of the Requirements for the Degree of Doctor of Philosophy in Atmospheric Physics

Examining Board: Prof. dr. ir. Sander Houweling

Signature:

Date:

Examining Board: Dr. Kassahun Ture

Signature:

Date:

Advisor: Prof. Gizaw Mengistu Tsidu

Signature:

Date:

Abstract

The carbon cycle of tropical terrestrial vegetation plays a vital role in the storage and exchange of atmospheric carbon dioxide (CO_2). However, large uncertainties surround the impacts of land-use change, climate warming, the frequency of droughts, and CO_2 fertilization. This culminates in poorly quantified carbon stocks and carbon fluxes even for the major ecosystems in Africa's carbon cycle (savannas and tropical evergreen forests). Contributors to this uncertainty are the sparsity of (micro-)meteorological observations across Africa's vast land area, a lack of sufficient ground-based observation networks and validation data for CO_2, and incomplete representation of important processes in numerical models. Satellite retrievals are strongly influenced by land-use changes, cloud cover, and aerosol loading. Moreover, Africa is a continent with wide extremes in surface type (which ranges from desert, rainforest, and Savannah) and aerosol loading. Therefore, the comparison of satellite observations with model and available in-situ observations will be useful to prove the performance of satellites and show how these systematic errors vary geographically over the continent. In this thesis, GOSAT column-averaged dry-air mole fraction of carbon dioxide (XCO_2) is compared with the NOAA CT2016 and six flask observations across Africa using five years of data covering the period from May 2009 to April 2014. Besides, XCO_2 from OCO-2 is compared with NOAA CT16NRT17 and eight flask observations across Africa using two years of data covering the period from January 2015 to December 2016. The analysis shows that the XCO_2 from GOSAT is higher than XCO_2 simulated by CT2016 by 0.28 ± 1.05 ppm, whereas OCO-2 XCO_2 is lower than CT16NRT17 by 0.34 ± 0.9 ppm on African landmass on average. The mean correlations of 0.83 ± 0.12 and 0.60 ± 0.41 and an average RMSD of 2.30 ± 1.45 and 2.57 ± 0.89 ppm are found between the model and the respective datasets from GOSAT and OCO-2 implying the existence of a reasonably good agreement between CT and the two satellites over Africa's land region. However, significant variations were observed in some regions. For example, OCO-2 XCO_2 is lower than that of CT16NRT17 by up to 3 ppm over some regions in North Africa (e.g., Egypt, Libya, and Mali) whereas it exceeds CT16NRT17 XCO_2 by 2 ppm over Equatorial Africa (10°S - 10°N).

This regional difference is also noted in the comparison of model simulations and satellite observations with flask observations over the continent. For example, CT shows a better sensitivity in capturing flask observations over sites located in Northern Africa. In contrast, satellite observations have better sensitivity in capturing flask observations in lower altitude island sites. CT2016 shows a high spatial mean of seasonal mean RMSD of 1.91 ppm during DJF from GOSAT, while CT16NRT17 shows RMSD of 1.75 ppm during MAM from OCO-2. On the other hand, the low RMSD of 1.00 and 1.07 ppm during SON in model XCO_2 from GOSAT and OCO-2, respectively, indicate better agreement during autumn. The model simulation and satellite observations exhibit similar seasonal cycles of XCO_2 with a small discrepancy over Southern Africa (35° - 10°S) and during wet seasons over all regions. Two remotely sensed vegetation products that have been shown to correlate highly with Gross Primary Productivity (GPP): Sun-Induced Fluorescence (SIF) and Near-Infrared Reflectance of vegetation (NIRv) are also analyzed to further understand the dynamics of carbon dioxide flux. A comparison against flux tower observations of daytime-partitioned Net Ecosystem Exchange (NEE) from six major biomes in Africa shows that SIF and NIRv reproduce the seasonal patterns of GPP well, resulting in correlation coefficients of $>$0.9 (N=12 months, 4 sites) over savannas in the northern and southern hemisphere. These coefficients are slightly higher than for the widely used MPI-BGC GPP products and Enhanced Vegetation Index (EVI). Similar to SIF signals in the neighbouring Amazon, peak productivity occurs in the wet season coinciding with peak soil moisture, and is followed by an initial decline during the early dry season that reverses when light availability peaks. This suggests similar leaf dynamics are at play. Spatially, SIF and NIRv show a strong linear relation (R $>$0.9, N=250+ pixels) with multiyear MPI-BGC GPP even within single biomes. Both MPI-BGC GPP and EVI show saturation relative to peak NIRv and SIF signals during high productivity months, which suggests that GPP in the most productive regions of Africa might be larger than suggested. Africa's biome integrated productivity is strongly controlled by the seasonality of soil moisture, with a weak influence of light availability superimposed, indicating that the biome productivity of Africa strongly depends on spatiotemporal drivers. Therefore, an understanding of the spatiotemporal ecosystem dynamics together with its relation to meteorological variables is paramount to quantify the responsiveness of the carbon cycle to climate variability. For that reason, an Empirical Ensemble Mode Decomposition (EEMD) was applied on 17 years monthly time series of natural CO_2 flux covering the period from January 2000 to December 2016. The EEMD depicts natural CO_2

flux has six periodicities over tropical Africa corresponding to seasonal, interannual, and decadal-scale variabilities which are likely driven by atmospheric and oceanic processes. Seasonal variabilities at quasi-3 months, quasi-6 months, and quasi-12 months contribute about 91.41% of the variability of natural CO_2 flux, suggesting that CO_2 flux has a strong variability at the seasonal scale. Moreover, high atmospheric CO_2 flux was observed during warm and dry conditions. Precipitation is found to be a dominating driver of CO_2 flux at the seasonal scale over the west coast of tropical Africa and East Africa. In addition to the six periodicities, the application of EEMD to a monthly time series of CO_2 flux indicates the existence of either a nonlinear downward trend or a possible multi-decadal periodicity that cannot be captured by the limited length of the current data set. The later is more likely as revealed by a slight reversal at the beginning of 2013. Moreover, analysis of different regions of tropical Africa shows reduced CO_2 uptake over most regions since 2000, with exception for tropical North Africa which is found to have increased CO_2 uptake most likely due to enhanced vegetation which exceeds deforestation. At the interannual scale, a quasi-2 year and quasi-5 year fluctuations were obtained from the EEMD with a contribution of 6.93% to the total CO_2 flux variability. This interannual fluctuation has a significant correlation with Niño 3.4 index, El Niño induced temperature, precipitation, soil moisture, and enhanced vegetation index. A significant positive correlation between a warming temperature and interannual CO_2 flux over tropical North Africa and rainforest regions suggests that temperature is the major driver of CO_2 fluctuation at the interannual scale over these regions. Conversely, over Western and Tropical East Africa, precipitation was found as the most dominant driver. The anomalously high interannual CO_2 flux was found in response to strong El Niño (Niño 3.4 index greater than 1.0) in the years 2009 and 2015/16 over most of Equatorial Africa. During the peak of 2015/16 El Niño, tropical Africa releases 0.2 $mol/m^2/month$ CO_2 into the atmosphere due to interannual variability. The strongest (0.5 $mol/m^2/month$) contribution was from the tropical rainforest, most likely driven by the rising temperature. Besides, Ethiopian highlands also release 0.4 $mol/m^2/month$ CO_2 flux due to dry and warm conditions during this strong El Niño event. The CO_2 flux mean over 17 years (2000-2016) shows that tropical Africa is a net CO_2 sink (-7.02 gC/m^2/*year*). However, during the 2015/16 El Niño years, tropical Africa releases 29.12 gC/m^2/*year* leading to 487.49 TgC/year which is twice the estimated carbon flux of Africa (240 Tg C y^{-1}) for the period covering from 2000 to 2005.

Acknowledgements

Foremost, I would like to thank my advisor, Professor Gizaw Mengistu. He has been a model of scientific excellence and generous mentorship. I deeply appreciate his guidance, support, patience, and understanding, as a teacher, researcher, and friend. I admire his incommensurable knowledge, his real zest for science, and unmatched modesty. Most of all, I am grateful that he allowed me to visit and study with him in one of the most prestigious Earth and Environmental department at Botswana International University of Science and Technology. He also opens the way to visit and get further guidance from one of the most prestigious Environmental Sciences Institute, Department of Meteorology and Air Quality, Wageningen University and Research, The Netherlands.

I am happy to thank Addis Ababa University for hosting me to pursue my Ph.D. studies. Particularly, I would like to thank the physics department head, Dr. Teshome Senbeta for the efforts and the facilitation he did to finalize my study. I would also like to acknowledge Addis Ababa Science and Technology University, Botswana International University of Science and Technology, The Coimbra Scholarship, University of Groningen, Wageningen University and Research, KNMI, FMI, and EUMETSAT for their founds and scholarship opportunity. It is my pleasure to acknowledge NOAA, NASA, and flask and Flux Tower PI's for their data.

I would like to extend my gratitude to the thesis examining committee, Prof. Dr. Ir. S. Houweling and Dr. Kassahun Ture, for reading my thesis and for providing me with very useful comments and suggestions. I have no words to express my sincere thanks and gratitude to Professor Peter Wouter, Piet Stammes, and Koonman Mourits, who invited me to visit the Netherlands. They provide me a chance to join and collaborate with experts in the field of carbon cycle and satellite remote sensing from the University of Groningen, Royal Netherlands Meteorological Institute (KNMI), and Wageningen University. I also enjoyed very much my interaction and collaboration with Koren Gerbrand, Olaf Tender, and K. Folkert Boersma which resulted in a published paper together; we had many interesting talks and I want to thank you all for that valuable experience.

Professor Habtu Zegeye, Dr. Semu Kassa, Dr. Sherif, Mulugeta, Getachew, Tsilat . . . have proved to be the nicest people I have ever meet, very considerate,

helpful and fun. Thank you to my excellent friends Nika, Tamirat, Sintayehu, Gezahagn, Abera, . . . , who have made my life inside and outside of school, a lot more fun, and a lot more interesting time we spend frightful times together. They have been a constant support and a source of a good time. Special Nika goes to my closest friend.

This thesis would never have been completed without the continuous moral support, unconditional love, and total devotion of my wife Awot Asefa. She always was there for me ready to listen to all my problems, giving me well-thought advice. I want to thank my beautiful daughters Marda Anteneh and Fetina Anteneh, their smile gives me courage and strength which can never be expressed in words. Special thanks go to my sisters and brothers for always encouraging me and building up my confidence. I am very happy to thank my brothers Abiy and Nika in particular. They have been more than a father to my daughters while I was not there. I don't know what I would have done without them. I am grateful to my Mother Asnakech and Father Getachew for making me who I am, teaching me how to live my life in good spirits and how to achieve any goal through much work, persistence, and resilience. I dedicate this Ph.D. thesis to them! Who, unfortunately, are no longer with us. Thank you Awot for the love and support you have surrounded me with all this time, for making me happy and bringing joy into my everyday life. Any achievement I may have won't make much sense if I didn't share it with you.

Contents

Declaration of Authorship **i**

Abstract **iii**

Acknowledgements **vi**

1 Introduction **1**
- 1.1 Motivation 1
- 1.2 The global carbon cycle 4
- 1.3 Seasonal variation of CO_2 flux 9
- 1.4 Drivers of carbon dioxide 10
  - 1.4.1 Effects of El Niño and La Niña on CO_2 concentration . . . 10
  - 1.4.2 The role of temperature on CO_2 concentration 13
  - 1.4.3 The role of rainfall on CO_2 concentration 15
  - 1.4.4 Soil moisture and CO_2 concentration 15
- 1.5 Observations and modeling of carbon cycles 16
  - 1.5.1 Estimation of GPP from fluorescence 16
  - 1.5.2 Flux partitioning algorithm 19
  - 1.5.3 Modeling of carbon flux 20
- 1.6 Past attributes of the study 22

2 Study area and Datasets **28**
- 2.1 Description of the study area 28
- 2.2 Data Sets 31
  - 2.2.1 Carbon Tracker Model and Data 31
  - 2.2.2 GOSAT measurements 32
  - 2.2.3 OCO-2 measurements 32
  - 2.2.4 GOME-2 SIF 33
  - 2.2.5 Flask observations 34
  - 2.2.6 Eddy covariance flux data 35
  - 2.2.7 MPI-BGC GPP 35
  - 2.2.8 Satellite-based vegetation indices from MODIS 35

2.2.9 Other datasets 37
2.3 Basic statistics 38

3 On the performance of satellite-based observations of CO_2 in capturing the NOAA Carbon Tracker model and ground-based flask observations over Africa land mass 39
3.1 Background 39
3.2 Analysis methods 40
3.3 Validation of CT XCO_2 41
3.3.1 Comparison of XCO_2 mean climatology from NOAA CT2016 and GOSAT 41
3.3.2 Comparison of monthly average time series of NOAA CT2016 and GOSAT XCO_2 46
3.3.3 Comparison of seasonal climatology 50
3.3.4 Comparison of GOSAT and CT2016 with flask observations 53
3.3.5 Comparison of mean XCO_2 from NOAA CT16NRT17 and OCO-2 55
3.3.6 Comparison of monthly average time series of NOAA CT16NRT17 and OCO-2 XCO_2 58
3.3.7 Comparison of seasonal means of NOAA CT16NRT17 and OCO-2 XCO_2 60
3.3.8 Comparison of OCO-2 and CT16NRT17 with flask observations 63
3.4 Summary 64

4 Sun-induced Fluorescence and Near-Infrared Reflectance of vegetation track the seasonal dynamics of gross primary production over Africa 66
4.1 Background 66
4.2 Analysis methods 67
4.3 Seasonal dynamics of gross primary productivity 69
4.3.1 GPP proxies and eddy-covariance derived GPP estimates 69
4.3.2 GPP proxies across the major biomes of Africa 73
4.3.3 SIF-GPP/NIRv-GPP Estimation for the Major Biomes . . . 76
4.4 Summary 80

5 Trends, periodicity and associated drivers of natural carbon dioxide flux over tropical Africa land mass 82
5.1 Background 82

5.2 Analysis methods 83
5.3 Spatiotemporal variability of CO_2 86
  5.3.1 CO_2 Periodicity over tropical Africa 86
  5.3.2 Trends and variability of CO_2 flux 89
  5.3.3 Seasonal variability of natural CO_2 flux with temperature, precipitation, soil moisture and EVI 91
  5.3.4 Relation between Interannual natural CO_2 flux variability and ENSO events 93
  5.3.5 Influence of El Niño induced temperature on CO_2 flux fluctuation 96
  5.3.6 Influence of El Niño induced precipitation on CO_2 flux fluctuation 98
  5.3.7 Influence of El Niño induced soil moisture on CO_2 flux fluctuation 98
  5.3.8 Influence of El Niño induced enhanced vegetation index on CO_2 flux fluctuation 99
5.4 Summary 100

6 Conclusions **102**

Bibliography **108**

List of Figures

1.1 Illustration of the carbon cycle shows the movement of carbon between ocean, land and atmosphere. Red numbers refer to the human contribution, yellow numbers refer for amount natural fluxes, and white numbers shows stored carbon in gigatons of carbon per year. (This diagram is adapted from U.S. DOE, Biological and Environmental Research Information System.) 5
1.2 Illustration from the fifth IPCC report (2014) showing the different global carbon budgets. With 123 $PgCyr^{-1}$. Gross photosynthesis is one of the major atmospheric carbon sinks. 6
1.3 Illustrative diagram for the Earth heat balance. (Diagram adapted from Environmental Initiative climate change support materials, University of Lehigh.) 7
1.4 Spatio-temporal distributions of CO_2 flux components from CT2017-flux averaged over 2000-2016 at 1^0X1^0 resolution. The white color refers to near zero CO_2 flux. 8
1.5 Seasonal amplitudes of NOAA Carbon Tracker CO_2 flux over Northern (10.5^0 *to* 35.5^0), Equatorial (-10.5^0 *to* 10.5^0) and Southern (-35.5^0 *to* -10.5^0) Africa during 2000-2016. a) CO_2 flux due to the biosphere atmosphere exchange. b) CO_2 flux due to the forest fire. c) net CO_2 flux due to the biosphere atmosphere exchange and forest fire. 10
1.6 Trailing twelve-month average of year-over-year change in parts per million of atmospheric CO_2 versus El Niño (red) and La Niña (blue). Covering the periods from January 1960 - 2016. This figure is adapted from Political Calculations 2016. 11
1.7 Schematic of the mechanistic differences between normal (upper panel) and El Niño conditions (bottom panel) and associated carbon response over the tropical Pacific Ocean. Warm ocean surface temperatures are denoted in red, cooler waters in blue. This figure is adopted from Chatterjee et al. (2017). 12

1.8 Monthly and running 37 months average of global temperature estimates and atmospheric CO_2 concentration. Blue zigzag line indicates a steady rise in CO_2 and five multicolored lines are global average temperature anomaly from five datasets. This figure is adopted from Boretti and Florentine (2019) 14

1.9 Photosynthetic mechanism within the chloroplast of plant cell emitting fluorescence in the process of sunlight to energy conversion. This diagram is adopted from NASA Goddard's Conceptual Image Lab/T. Chase. 17

1.10 Simulated terrestrial spectra on its way through the atmosphere in a wavelength rage from 600-800 nm. This figure is adopted from Joiner et al. (2016) 18

2.1 Annual mean SIF and NIRv averaged over the years 2007-2016 at $0.5^\circ \times 0.5^\circ$ resolution, shown in (a) and (b) respectively. c) Climatology of gross primary production (Beer et al., 2010) at $0.5^\circ \times 0.5^\circ$ resolution. d) Simple precipitation anomaly (SPA) computed from the multi-year GPCC monthly averaged precipitation covering the period from 1951 to 2000 for the major vegetation types of Africa. The red lines indicate thresholds for wet months SPA ≥ 0.7 mm month^{-1} and dry months SPA ≤ -0.6 mm month^{-1} and e) vegetation types from the terrestrial biosphere model SiB-CASA and the white colour refers to none vegetated regions. The rectangle window with a pentagon star at the center in a) and e) shows the distribution of flask and flux towers respectively. The rectangular box in c) shows regions with the same climate according to the K*ö*ppen climate classification (Kottek et al., 2006). The letters represent subregions in tropical Africa; 'A' refers to tropical western Africa, 'B' refers to tropical North Africa, 'C' refers to Ethiopian Highlands, 'D' refers to tropical rainforest, 'E' refers to tropical Southern Africa and 'F' refers to tropical East Africa. . . . 29

3.1 Distribution of five-years averages of CT2016 **(a)** and GOSAT **(b)** XCO_2 and their difference **(c)** gridded in $3^0 \times 2^0$ bins over Africa's Land mass; and the total number of datasets at each grid from the GOSAT observations(d). 43

3.2 Histogram of the difference of CT2016 relative to GOSAT (left panel) and color code scatter diagram of XCO_2 concentration as derived from CT2016 and GOSAT (right panel). Color indicates the relative distance in unit of degrees as shown in colorbar between datasets. 44
3.3 Spatial patterns of bias (a), correlation (b), RMSD (c) of the two data sets, and mean posteriori estimate of XCO_2 uncertainty from GOSAT (d). 44
3.4 The monthly mean time series of CT2016 and GOSAT from May 2009 to April 2014 averaged over North Africa (a), bias associated with the monthly means (b), the histogram of difference in XCO_2 computed as CT2016-GOSAT XCO_2 in units of ppm (change in CO_2) (c) and the annual growth rate obtained by subtracting the mean from the mean of the next year (d). The error bars in (a) show the GOSAT a posteriori XCO_2 uncertainty. 47
3.5 The same as Fig. 3.4 but over Equatorial Africa. 47
3.6 The same as Fig. 3.4 but over Southern Africa. 48
3.7 Seasonal climatology of XCO_2 for NOAA CT2016 (left panels) and GOSAT (midel panels) and their difference (right panels). . . 51
3.8 Histogram of difference for the seasonal XCO_2 climatology for DJF (a), MAM(b), JJA (c) and SON (d) seasons. 51
3.9 CO_2 time series for the coincident period for CT2016 (red), GOSAT (green) and flask (black). The standard deviation in computing the monthly mean is indicated by the vertical error bar. 53
3.10 De-trended seasonal cycles of near surface CO_2 mixing ratio during 2009-2014 from CT2016 (red), GOSAT (green), and flask (black) observations. The standard deviation of the monthly variables is indicated by error bars. 54
3.11 Distribution of two years average XCO_2 of CT16NRT17 **(a)** and OCO-2 **(b)** XCO_2 and their difference **(c)** gridded in $3^0 \times 2^0$ bins; and **(d)** the total number of datasets at each grid 55
3.12 Histogram of the difference of CT16NRT17 relative to OCO-2 (left panel) and color code scatter diagram of XCO_2 concentration as derived from CT16NRT17 and OCO-2 (right panel). Color indicates the relative distance in unit of degrees as shown in colorbar between datasets. 57
3.13 The bias (a), correlation (b), RMSD (c) of model and OCO-2 XCO_2 and mean posteriori estimate of XCO_2 error from OCO-2 (d). . . . 58

3.14 The monthly mean time series of CT16NRT17 and OCO-2 from January 2015 to December 2016 averaged over North Africa (a), bias associated with the monthly means (b), the histogram of difference (c) and the annual growth rate obtained by subtracting the mean from the mean of the next year (d). The error bars in (a) shows the OCO-2 a posteriori XCO_2 uncertainty. 59
3.15 The same as in Fig. 3.14 but over Equatorial Africa. 61
3.16 The same as in Fig. 3.14 but over Southern Africa. 61
3.17 Seasonal mean of CO_2 for NOAA CT16NRT17 (left panels) and OCO-2 (middle panels) and their difference (right panels). 62
3.18 Histogram of difference for the seasonal CO_2 climatology for DJF (a), MAM(b), JJA (c) and SON (d) seasons. 63
3.19 CO_2 from CT16NRT17, OCO-2 and flask observations. 64

4.1 The skill of NIRv, SIF, EVI and MPI-BGC GPP in capturing the seasonal cycle of GPP from flux towers. The shaded area indicates the standard deviation around the monthly means. Note that NIRv, SIF and EVI do not have the same unit as GPP and their values are provided on the secondary y-axis. 69
4.2 Comparison of eddy covariance GPP with NIRv, SIF, MPI-BGC GPP, NDVI and EVI for major biomes around the flux-tower. To obtain sufficient data the comparison is made by averaging monthly values within a 4° × 4° window enclosing the tower. Furthermore, to account for vegetation heterogeneity of the land, grid cells with a different vegetation type than for the tower location were masked. 71
4.3 Comparison of coarse NIRv at 0.5° × 0.5° (left panels) and high resolution NIRv at 0.05° × 0.05° (right panels) with flux tower measured GPP (EC-GPP) for a selection of three African flux towers (GH-Ank, SD-Dem and ZM-Mon). The temporal correlation between NIRv and EC-GPP is given in each panel. 73
4.4 Seasonal cycles of NIRv, SIF, precipitation, short wave radiation (SWR), EVI and MPI-GPP at 0.5° × 0.5° resolution over major biomes of Africa covering the period from 2007 to 2011. The error bars provided for precipitation denote the standard deviation around the mean. 75
4.5 Seasonal values SIF verses EVI as a response of C3 grass and shrub vegetation types of Africa a) Northern of the equator and b) South of the equator. 75

4.6 Relation between SIF/NIRv with incoming downward shortwave radiation (left panels), root zone soil moisture (right panels) for major African biomes. Upper panels show results over the vegetated regions of Northern Africa (north of the equator) while the bottom shows the results for Southern Africa (south of the equator). The numbers in the plot, and the colour of the markers, refer to the month of the year. 76
4.7 Comparison of aggregated MPI-BGC GPP, SIF-GPP and NIRv-GPP for major biomes in Africa. N is the number of grid box of size $0.5^{\circ} \times 0.5^{\circ}$ used in the aggregation. 78
4.8 Comparison of eddy covariance GPP with NIRv and SIF around the Brazil BR-Sa1 flux tower. To obtain sufficient data the comparison is made by averaging monthly values within a $4^{\circ} \times 4^{\circ}$ window enclosing the tower. Furthermore, to account for vegetation heterogeneity of the land, grid cells with a different vegetation type than for the tower location (evergreen broad-leaf forest) were masked. The regression slope and intercepts are used to infer GPP from NIRv and SIF over African broad-leaf evergreen forest. 78
4.9 Seasonal cycles of GPP derived from FLUXNET2015 GPP (black), SIF-GPP (green), NIRv-GPP (blue) and MPI-BGC GPP (red) averaged for the available months of the flux site. Flux tower site IDs are indicated as a title over each box. Shaded areas are the standard deviations of the monthly means. 80

5.1 Ensemble empirical mode decomposition of CT2017-flux at seasonal (IMF1-IMF3), inter-annual (IMF4 and IMF5), and inter-decadal (IMF6 and Trend) scale covering the period from 2000 to 2016 in tropical Africa. A negative value implies that the biosphere is a sink of CO_2. 87
5.2 Spatial distribution of periodicity for each IMF in the natural CO_2 flux (Periodicity) and the associated variance contribution rate (VCR) covering the period from 2000 to 2016 at a resolution of 1^0X1^0. 88
5.3 Statistical significance of each IMFs averaged over tropical Africa. The results were computed as the natural logarithm of CO_2 flux (fc) versus the natural logarithm of the mean period in months (T) for each IMFs. 89

5.4 Statistical significance of each IMFs averaged over subregions tropical Africa. a) tropical Western Africa, b) Tropical North Africa, c) Ethiopian Highlands , d) tropical rainforest, e) tropical Southern Africa and f) Tropical East Africa F). 90
5.5 Time series of total natural CT2017-flux (black line), seasonal variability (blue line), interannual variability (green line) and the trend component (red line) during 2000-2016 over tropical Africa. . . . 91
5.6 The same as Fig. 5.5 but over a) tropical Western Africa, b) Tropical North Africa, c) Ethiopian Highlands , d) tropical rainforest, e) tropical Southern Africa and f) Tropical East Africa. 92
5.7 Correlation of seasonal fluctuation in the natural CO_2 flux with seasonal fluctuation of: a) Temperature, b) Precipitation, c) Root zone soil moisture and d) EVI. 93
5.8 a) Correlation of interannual fluctuation in the natural CO_2 flux with Niño 3.4 index and b) the corresponding lag time in units of months over tropical Africa covering the period from January 2000 to December 2016. 94
5.9 Time series of interannual variability of temperature (red line), Niño 3.4 index (black line), precipitation (green line), natural CO_2 flux (blue line) during 2000-2016 over a) tropical Western Africa, b) Tropical North Africa, c) Ethiopian Highlands , d) tropical rainforest, e) tropical Southern Africa and f) Tropical East Africa F). . 95
5.10 a) Correlation of interannual temperature fluctuation with Niño 3.4 index, and c) the corresponding lag time in units of months; b) correlation of interannual fluctuations of temperature with CO_2 flux and d) the corresponding lag time in units of months. 97
5.11 The same as Fig. 5.10 but with interannual fluctuation of precipitation. 99
5.12 The same as Fig. 5.10 but with root zone soil moisture. 99
5.13 The same as Fig. 5.10 but with enhanced vegetation index. 100

List of Tables

2.1 Some basic information on the satellites used for the study. *After July 2013, the GOME-2(a) swath is half the size, pixels are 40x40 km^2 and repeat cycle is increased to 3 days. 34
2.2 Information on flask observation sites near and within Africa land mass. * indicates discontinued site or project. 34
2.3 Information on flux-tower sites in Africa. 35

3.1 Summary of statistical relation between CT2016 and GOSAT observation. The statistical tools shown are the mean correlation coefficient (R), the spatial average of bias (Bias), the spatial average root mean square deviation (RMSD), the standard deviation in bias (std of Bias), GOSAT posteriori estimate of XCO_2 error (GOSAT err), the standard deviation in CT2016 XCO_2 (CT2016 std) and the standard deviation in GOSAT XCO_2 (GOSAT std). . 45
3.2 Summary of statistical relations between CT2016 and GOSAT observations. The statistical analysis were made using a monthly averaged time series of 60 months (i.e., months from May 2009 to April 2014). 46
3.3 Five years monthly averaged XCO_2 concentration in ppm obtained from CT2016 (CT) and GOSAT (GO) and their difference $CT - GO$ (D) in ppm over Africa (A), North Africa (NA), Equatorial Africa(EA) and Southern Africa (SA). 49
3.4 Summary of statistical relations between CT2016 and GOSAT XCO_2: Bias, correlation (R), Root mean square deviation (RMSD), standard deviation of XCO_2 from CT2016 simulation (CT2016 std), standard deviation of XCO_2 from GOSAT observation (GOSAT std), aggregate number of coincident observations (number of data) and number of grids over the region (grid). 52
3.5 Summary of statistical relations of CT2016 and GOSAT observations with respect to flask observations. The statistical analysis was made using the monthly averaged covering the period from May 2009 to April 2014). 54

3.6 Summary of statistical relation between CT16NRT17 and OCO-2 observation. 56
3.7 Annual growth rate (AGR) of XCO_2 over Africa land mass from CT16NRT17 and OCO-2. The results are obtained as the mean annual difference of 2015 and 2016 values 60
3.8 Summary of statistical relation between CT16NRT17 and OCO-2 observations with respect to flask observations. The statistical analysis were made using the monthly averaged covering the period from May 2009 to April 2014). 63

4.1 Linear regression results for NIRv and SIF with MPI-BGC GPP from Beer et al. (2010) over major biomes of Africa. y is the GPP inferred from NIRv/SIF and x is the NIRv/SIF signal. R is the spatial correlation coefficient between these signals and MPI-BGC GPP. n refers to the number of data points used in the regression analysis. 77
4.2 comparison of biome specific estimates of five years mean GPP covering the period from 2007 to 2011 for major biomes of Africa as derived from: leaner regression of SIF/NIRv-vs-EC-GPP and Max-Planck Ensemble GPP (MPI-GPP). 79

5.1 Mean periodicity of each IMF in the natural CO_2 flux and the associated contribution rate for the variation in the total natural CO_2 flux during 2000 - 2016 in tropical Africa. 86
5.2 CO_2-flux balance of tropical Africa in units of $gCm^{-2}y^{-1}$. Carbon balance covering the period from 2000 to 2016 (17 years mean), during the strong El Niño event of 2015/16 (2015/16). Contribution from seasonal variability (CSV) and Contribution from interannual fluctuation (CIV). 94

List of Abbreviations

$\mathbf{A}_s$	surface **A**lbedo
APAR	**A**bsorbed **P**hotosynthetically **A**ctive **R**adiation
$\mathbf{CO}_2$	**C**arbon dioxid
CT2016	**C**arbon **T**racker release version CT**2016**
CT-NRT.v2017	**C**arbon **T**racker **N**ear **R**eal **T**ime release **v**ersion CT**2017**
$\mathbf{E}_0$	solar irradiance at the top of atmosphere
EC	**E**ddy **C**ovariance
EEMD	**E**mpirical **E**nsemble **M**ode **D**ecomposition
ENSO	**E**l **N**iño **S**outhern **O**scillation
ECMWF	**E**uropean **C**entre for **M**edium-Range **W**eather **F**orecasts
ESRL	**E**arth **S**ystem **R**esearch **L**aboratory
EVI	**E**nhanced **V**egetation **I**ndex
GOME-2	**G**lobal **O**zone **M**onitoring **I**nstrument 2
GOSAT	**G**reenhouse gas **O**bserving **SAT**ellite
GPCC	**G**lobal **P**recipitation **C**limatology **C**enter
GPP	**G**ross **P**rimary **P**roduction
GtCarbon	**G**iga **t**one of **Carbon**
$\mathbf{I}_F$	fluorescence emission
IMFs	**I**ntrinsic **M**ode **F**unctions
ITCZ	**I**nter-**T**ropical **C**onvergence **Z**one
LUE	**L**ight **U**se **E**fficiency
MODIS	**M**oderate **R**esolution **I**maging **S**pectroradiometer
$Kmolm^{-2}day^{-1}$	**K**ilo **mol**e per **m**eter square per **d**ay
NASA	**N**ational **A**eronautics and **S**pace **A**dministration
NASA GSFC	**NASA G**oddard **S**pace **F**light **C**enter
NEE	**N**et **E**cosystem **E**xchange
NBP	**N**et **B**iome **P**roductivity
NDVI	**N**ormalized **D**ifference **V**egetation **I**ndex
MPI	**M**ax **P**lanck **I**nstitute
NIRv	**N**ear **I**nfra-red **R**eluctance of **V**egetation
NOAA	The **N**ational **O**ceanic and **A**tmospheric **A**dministration
OCO-2	**O**rbiting **C**arbon **O**bservatory-2

$PgCyr^{-1}$	**P**eta **g**ram of Carbon per year
ppm	**p**articles **p**er **m**illion (1ppm CO_2= 2.12 GtCarbon)
SibCasa	**S**imple iosphere model
SIF	**S**un-**I**nduced **F**lorescence
SIFTER	**S**un-**I**nduced **F**luorescence of **T**errestrial **E**cosystems **R**etrieval
SPA	**S**imple **P**recipitation **A**nomaly
SPEI	**S**tandard **P**recipitation and **E**vaptranspiration **I**ndex
SSTs	**S**ea **S**urface **T**emperatures
TER	**T**errestrial **E**cosystem **R**espiration
TM5	global two-way nested **T**ransport **M**odel
XCO_2	column-average dry-ar mole fraction of carbon dioxide

Chapter 1

Introduction

1.1 Motivation

Carbon is an element necessary for life on Earth. It has both anthropogenic and natural sources. Carbon is a backbone for our civilizations, economies, homes, and means of transport, but that demand results in a global climate change which is one of the most momentous problems encountered us today. Carbon dioxide (CO_2) is one of the most important Earth's long-lived greenhouse gases. It absorbs less heat per molecule than the greenhouse gases methane or nitrous oxide, but a more abundant and longer lifetime in the atmosphere makes it the most influential greenhouse gas. On the other hand, CO_2 is less abundant and less powerful than water vapour on a molecule per molecule basis, but it absorbs wavelengths of thermal energy that water vapour does not, which means it adds to the greenhouse effect uniquely (Goody and Yung, 1995). The increases in atmospheric CO_2 concentration are responsible for about two-thirds of the total energy imbalance that is causing the air temperature to rise (Lindsey, 2009; Ekwurzel et al., 2017).

The wide acceptance of the existence of human-induced climate change, together with the dominant role of CO_2 as a greenhouse gas has led to increasing interest in characterizing the regional contributions of CO_2 source and sink, their underlying drivers, and their historical trends. The two main CO_2 fluxes are emissions from the fossil fuels combustion and net emissions from land-use change. The latter is largely driven by deforestation of the tropical forests (Canadell et al., 2007; Houghton, 2007). An understanding of the regional trends and contributions of CO_2 emissions is essential to design mitigation strategies to regulate the atmospheric concentration of greenhouse gases.

Therefore, it is timely and critical to study Africa's carbon budget. However, estimating African carbon stocks is a challenge due to significant uncertainties in meteorological driver data, lack of sufficient ground-based observation networks and validation data, and potentially uncertain representation of important processes in major ecosystems. The satellite CO_2 retrievals depend on the details of the land surface that they are taken over (albedo, surface type, land/water) as well as the local scatters affecting the scene (clouds, aerosols) (Chevallier, 2015). Africa is a continent with wide extremes in topography (which ranges from desert, savannah, and rainforest) and aerosol loading (Sayer et al., 2014). Since these are quite local variations in the satellite column CO_2 retrievals do reflect local conditions strongly. Thereby, indicating the source of systematic error in satellite observations will help to understand the geographical distribution of systematic errors over the continent (Lin et al., 2011). Once the biases in the satellite retrievals are understood and removed, the corrected satellite data can be assimilated into model flux inversion systems to calculate the African CO_2 fluxes in a more robust way. The National Oceanic and Atmospheric Administration (NOAA) Carbon Tracker model is one of the reliable dataset in the study of global CO_2 flux as it assimilates observations from in situ flask observations (Peters et al., 2007). Inter-comparison of these independent atmospheric CO_2 mole fraction (XCO_2) has a significant advantage to improve the model and satellite retrievals. We, therefore, motivated to test the performance of the most widely used NOAA's Carbon Tracker model against independent CO_2 dedicated satellites such as Greenhouse gas Observing SATellite (GOSAT) and Orbiting Carbon Observation 2 (OCO-2) and also with the existing limited flask observations in capturing the XCO_2 at a regional scale.

As XCO_2 retrievals are still in very active development, and previous versions of these products have displayed various biases despite enormous efforts and great diligence from the retrieval experts (O'Dell et al., 2018). An important next step is to understand the dynamics of CO_2 fluxes (GPP, TER, and NEE) using ground-based direct measurements, satellite observations, and model simulations. Especially, the gross primary production (GPP) is known to be one of the major CO_2 flux. Moreover, significant uncertainties in the carbon cycle study arose from an inefficient estimation of CO_2 flux (GPP). For example, the estimated global mean GPP, by Ardö (2015) shows a significant difference in ($1.7 PgCyr^{-1}$) between the estimated continental GPP from MOD17 and LPJ-GUESS. Besides, Fisher et al. (2013) estimated the mean GPP of the tropical forest of Africa to range from about 1.4 to 4.0 $kg\ C\ m^{-2}\ yr^{-1}$, indicating there is a large difference among nine applied global dynamic vegetation models. Thereby, it is difficult to evaluate the absolute magnitude of plant productivity without in-situ validation data. GPP estimation from the state-of-the-art models like the Max Planck Institute for Biogeochemistry may also be influenced in Africa as there are very sparse and limited observations that were included in the model assimilation. Remotely sensed vegetation reflectances have been recently investigated as a robust GPP proxy. Therefore, it has great importance to deal with how good are these products in tracking the seasonal dynamics of vegetation productivity over the continent in comparison with the limited available in-situ flux observations from FLEXNET2015.

The efficiency of the terrestrial ecosystem at absorbing atmospheric carbon dioxide depends on the availability of sunlight, soil moisture, and air temperature (Churkina and Running, 1998; Nemani et al., 2003). Thus, drought and high temperature associated with El Niño reduce the ability of the terrestrial ecosystem to assimilate carbon, while additional release by the frequent occurrence of fires further reduces the carbon uptake of the terrestrial biosphere (Bacastow et al., 1980; Werf et al., 2010). Therefore, it is essential to gain further insight into the processes involving CO_2 exchanges among the atmosphere, the biosphere, and the ocean to estimate the carbon sources and sinks and to comprehend the global and regional carbon cycle. For these reasons, a study is needed to investigate CO_2 trends and the underlying drivers, as well as to determine its correlation with temperature and the effect of El Niño and La Niña events on its concentration over Africa.

Inspired by these motivational elements, our work aims to address the following questions to the largest extent possible:

- How good enough are the XCO_2 data from satellite observations in comparison with an accurate model and in-suit flask observations over Africa?

- How consistent are XCO_2 from the model simulation and satellite observations in capturing the amplitudes and phases of observed seasonal cycles over different parts of the continent?

- How good is the agreement between the modelled spatiotemporal variability and the known seasonal climatology of the regions that determines carbon source and sink levels?

- How good are Sun-Induced Fluorescence (SIF) and Near-Infrared Reflectance of Vegetation (NIRv) in comparison with GPP from the eddy covariance flux towers?

- How good is SIF and NIRv in capturing the seasonal dynamics of GPP in comparison with the widely used greenness indices from the Moderate Resolution Imaging Spectroradiometer in Africa?

- How SIF and NIRv respond to the amount of soil moisture and shortwave radiation?
- How sensitive are SIF and NIRv in capturing the seasonal amplitudes of GPP from the Max Plank Institute of Biogeochemistry (MPI-BGC)?

- How accurate is the gross primary production estimated from SIF and NIRv for the major vegetation types of Africa?

- What is the response of terrestrial-atmospheric exchange of CO_2 flux at various localities over tropical Africa to ENSO events?

- What are the main drivers responsible for the observed CO_2 fluctuation?

- How much is the carbon dioxide stock of different subregions of equatorial Africa during the strongest El Niño (2015/16) event and what are their most probable drivers?

- What is the concurrent and lag correlation of temperature, precipitation, soil moisture, EVI, and Niño 3.4 indices with an interannual variation of CO_2 flux over Equatorial Africa landmass?

1.2 The global carbon cycle

The carbon cycle is the flow of carbon between each reservoir in an exchange, which has slow and fast components. The carbon cycle involves the flux or flow of carbon between different earth systems (atmosphere, land-biosphere, and oceans). The gaseous form of carbon is produced by the metabolism activity of living things, or by an inorganic process and becomes part of the carbon cycle. The change in the carbon cycle is due to drivers that can remove carbon out of one reservoir and put more carbon into the other reservoirs (see Fig. 1.1). An object or process that stores or absorbs carbon is termed as a sink, whereas the one that produces or releases carbon is called a source.

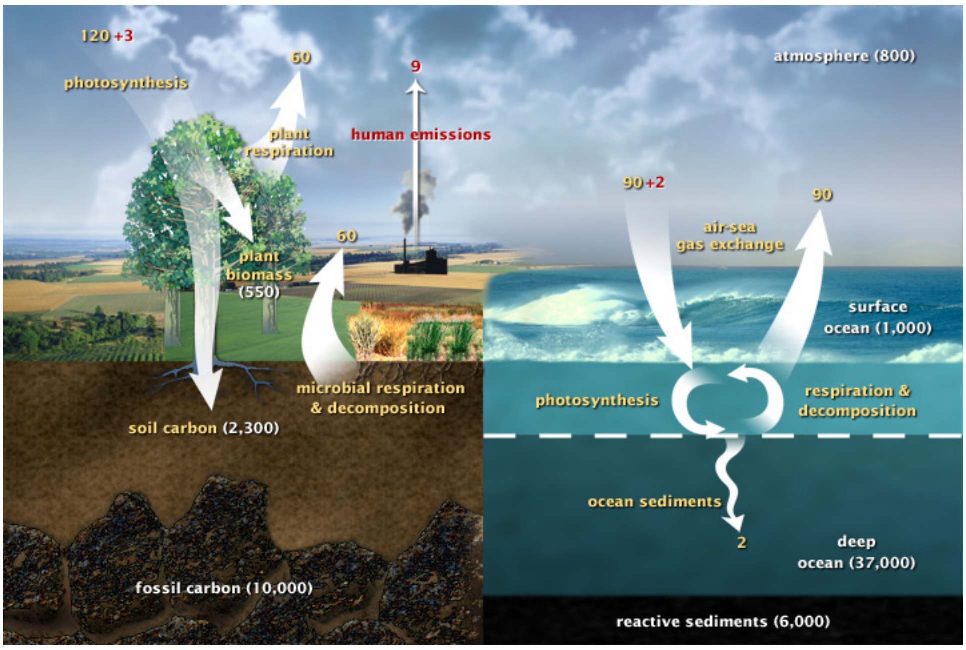

FIGURE 1.1: Illustration of the carbon cycle shows the movement of carbon between ocean, land and atmosphere. Red numbers refer to the human contribution, yellow numbers refer for amount natural fluxes, and white numbers shows stored carbon in gigatons of carbon per year. (This diagram is adapted from U.S. DOE, Biological and Environmental Research Information System.)

In the atmosphere, carbon dioxide (CO_2) is the dominant carbon-bearing trace gas with a recent (2018) concentration of approximately 407 ppm (Blunden and Arndt, 2019), which corresponds to a mass of 862.84 GtC (1PPM CO_2 = 2.12 Gt Carbon) (Prather, Holmes, and Hsu, 2012; Joos et al., 2013). Additional trace gases include methane (CH_4, current content mass $\approx$ 3.7 PgC) and carbon monoxide (CO, current content mass $\approx$ 0.2 PgC), and a small amount of hydrocarbons, black carbon aerosols, and organic compounds are also present in the atmosphere. The terrestrial biosphere stores about 450 to 650 Pg of carbon as an organic compound in the living vegetation biomass (Prentice et al., 2001). CO_2 is removed from the atmosphere by plant photosynthesis (Gross Primary Production (GPP), $123 \pm 8PgCyr^{-1}$, (Beer et al., 2010)) and carbon fixed into plants is then cycled through plant tissues, litter, and soil carbon and can be released back into the atmosphere by autotrophic (plant) and heterotrophic (soil microbial and animal) respiration and additional disturbance processes on a very broad time interval which ranges from seconds to millennia (e.g., occasional fires). Because CO_2 uptake by photosynthesis occurs only during the growing season, whereas CO_2 release by respiration occurs nearly year-round, the greater landmass in the Northern hemisphere imparts a characteristic 'sawtooth' seasonal cycle in atmospheric CO_2 (Keeling, 1960).

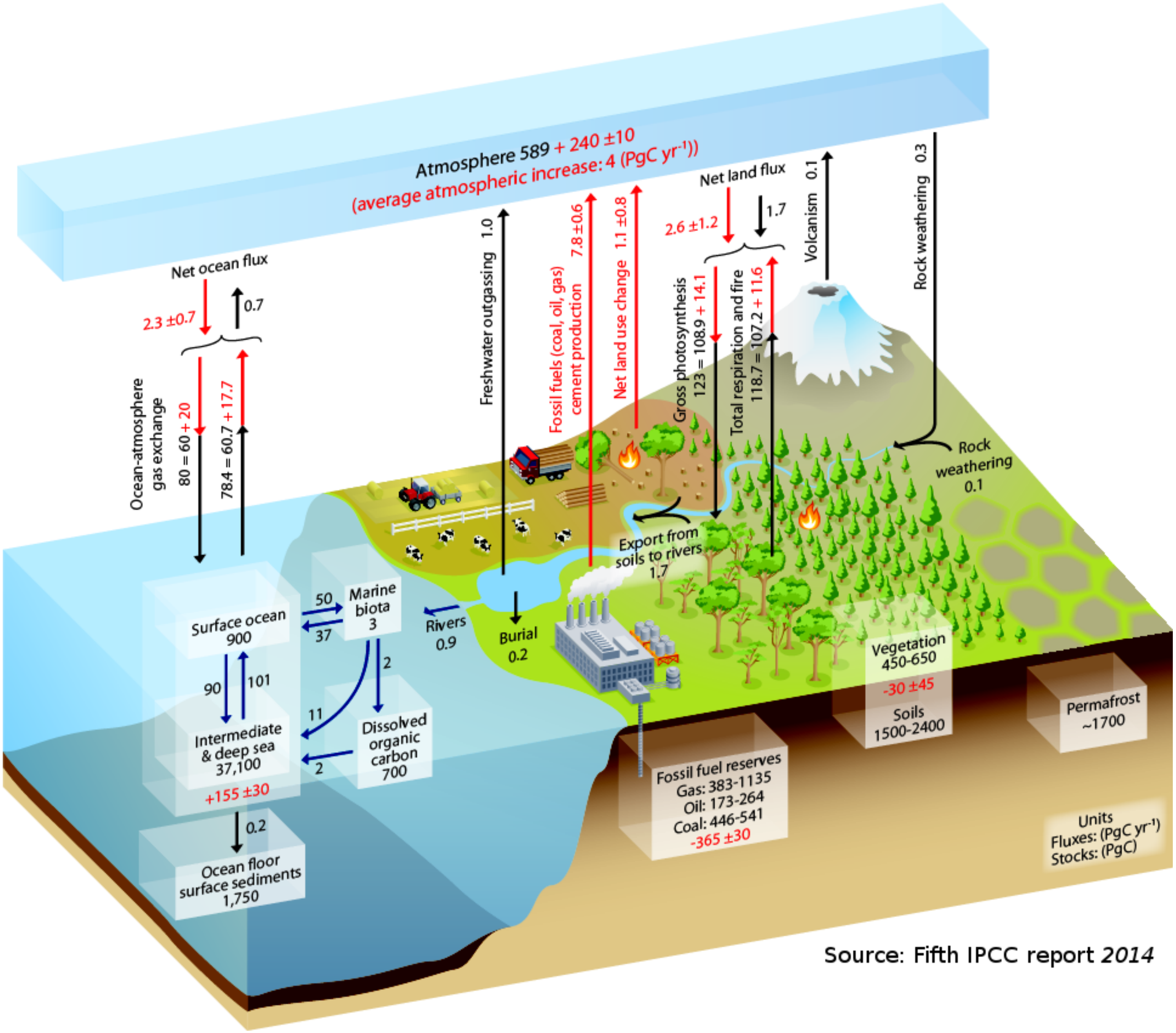

Source: Fifth IPCC report *2014*

FIGURE 1.2: Illustration from the fifth IPCC report (2014) showing the different global carbon budgets. With 123 $PgCyr^{-1}$. Gross photosynthesis is one of the major atmospheric carbon sinks.

The present-day concentration of atmospheric CO_2 continues to rise and ongoing emissions of CO_2 and other greenhouse gases will influence the global climate for the next decades and centuries. Approximately one-half of the CO_2 emissions from human activities are accumulating in the Earth's atmosphere, whereas the remaining portion of the emitted CO_2 is absorbed by sink processes in the ocean and on land (Raupach et al., 2007). The fifth IPCC report shows that the land biosphere is a net sink for about 2.6 PgC/year while the emission from fossil fuel is a source for about 7.8 PgC/year in the year 2014 (Fig 1.2). The net atmospheric growth of carbon flux has been calculated by the difference of net emissions from fossil fuels and land-use change, and the net uptake by the land and ocean. For example, the fifth IPCC report calculates the approximate atmospheric CO_2 growth of 4 PgC/year: fossil emission (7.8 PgC/year) + land-use change (1.1 PgC/year) - ocean uptake (2.3 PgC/year) - land uptake (2.6 PgC/year).

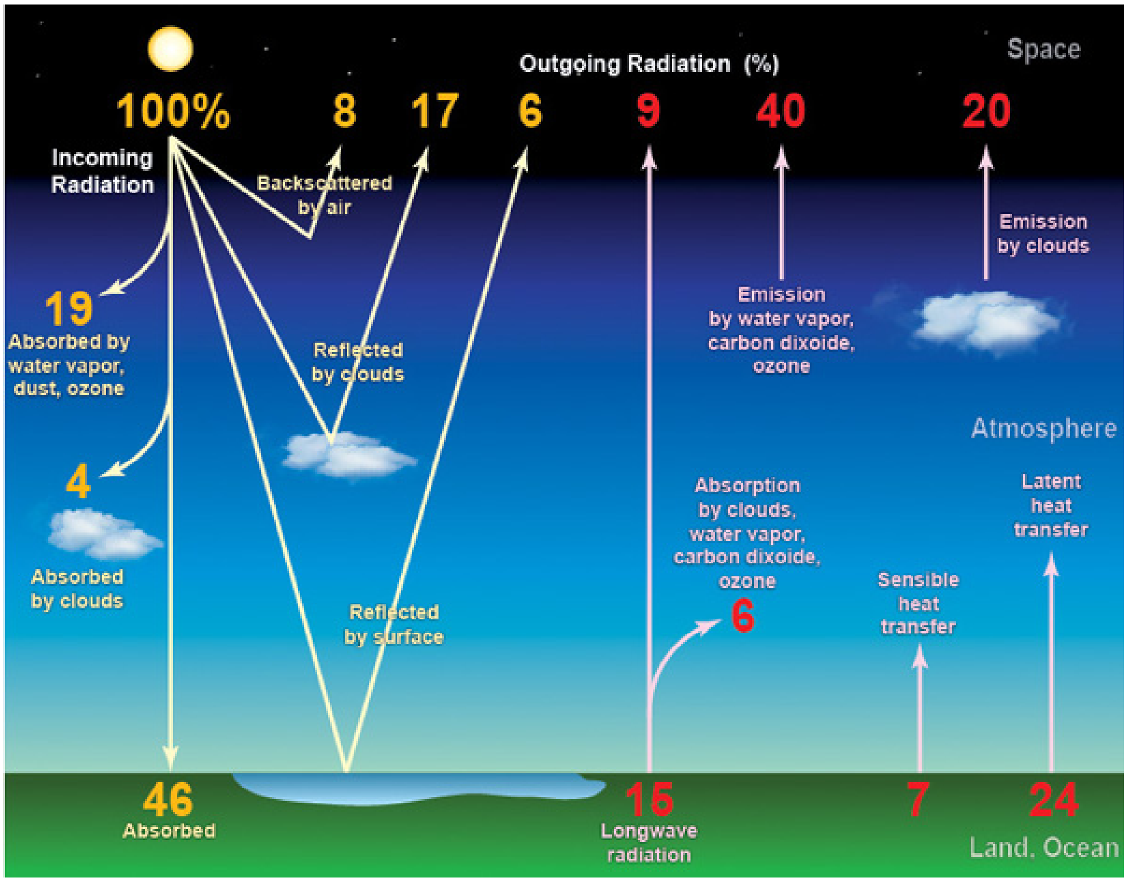

FIGURE 1.3: Illustrative diagram for the Earth heat balance. (Diagram adapted from Environmental Initiative climate change support materials, University of Lehigh.)

Changes that put CO_2 into the atmosphere cause the Earth's temperature to rise and potentially influence the climate. Carbon dioxide is the major greenhouse gas that absorbs and re-emits the outgoing long-wave radiation causing an increase of the Earth's heat content (see Fig. 1.3). CO_2 forces the Earth's energy budget out of balance by absorbing long-wave radiation radiated from the surface. It is a strong absorber of thermal infrared radiation with a wavelength of $> 12\ \mu$m, thereby increasing the concentration of carbon dioxide, partially closing the atmospheric window.

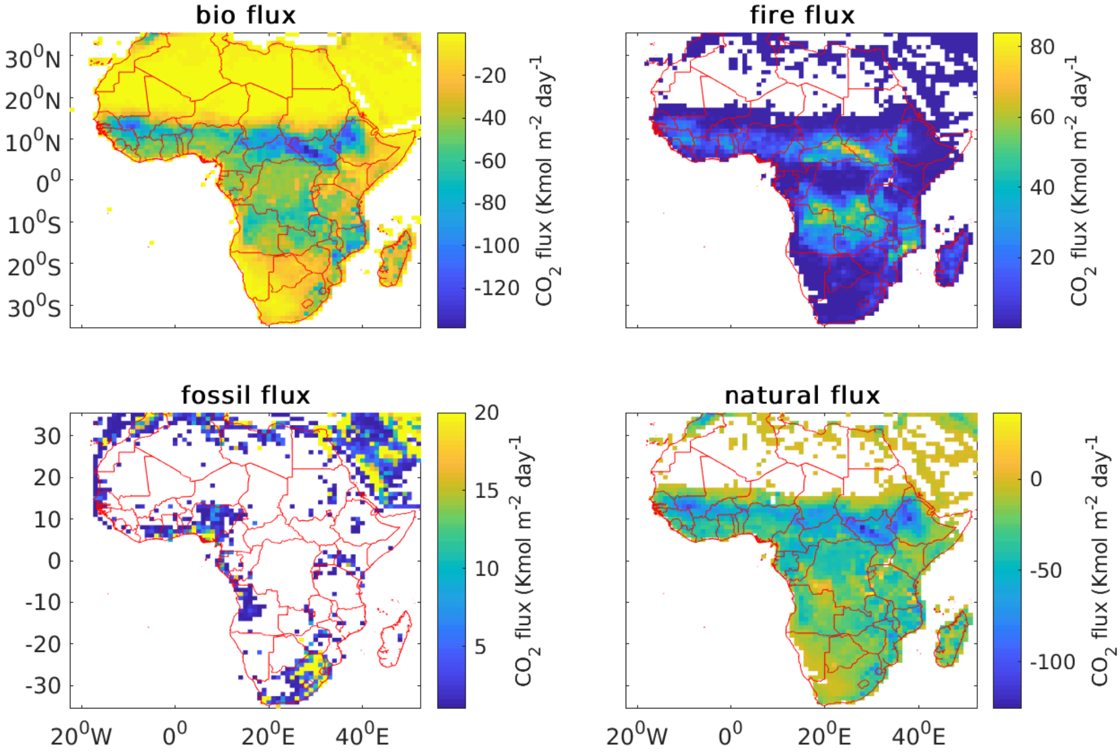

FIGURE 1.4: Spatio-temporal distributions of CO_2 flux components from CT2017-flux averaged over 2000-2016 at $1^0 X 1^0$ resolution. The white color refers to near zero CO_2 flux.

Africa is a net sink for CO_2 with a small fossil emission from countries like South Africa and Nigeria and forest fire emissions from the African savannas (Fig. 1.4). This uptake, however, varies significantly from year to year, and our understanding is limited to what causes these interannual variations (Peters et al., 2012). Some of the factors that contribute to the interannual variability include changes in fossil fuel emissions, natural variability in climate and weather patterns, fires, and volcanic eruptions. For example, it has been shown that interannual variability is correlated with the occurrence of El Niño/Southern Oscillation (ENSO) (Trenberth and Hoar, 1996). However, many fundamental questions about the driving mechanisms and the resulting carbon fluxes remain open (Pacala et al., 2007). We do not know in enough detail what the driving mechanisms are, how large the resulting carbon fluxes are, and how they vary on regional scales.

1.3 Seasonal variation of CO_2 flux

All the CO_2 time series show a well-known and dramatic global increase that is ascribed mostly to fossil fuel combustion and, less so, to land-use changes and deforestation (Sundquist, 1993). In addition to this trend, CO_2 concentrations generally have seasonal cycles that vary from place to place, as well as modest interannual fluctuations (Keeling et al., 1989; Lambert et al., 1995). Seasonal cycles in CO_2 concentrations are ascribed to seasonal changes in terrestrial ecosystems and, less so, marine CO_2 uptake (Ciais et al., 1996); they have increased in amplitude in recent decades, perhaps as a reflection of increasing mean concentrations or mean global-scale temperature (Myneni et al., 1997). Interannual fluctuations are attributed to changes in the upwelling of CO_2-rich ocean waters in the tropics and changes in terrestrial ecosystems associated with regional climate expression of El Niño and volcanic eruptions (Keeling et al., 1995). Understanding these small CO_2 changes should help provide insights into the mechanisms controlling atmospheric CO_2 concentrations and the partitioning of CO_2 changes between terrestrial and marine sources and sinks.

CO_2 seasonal behaviour changes with the seasonal pattern and intensity of photosynthesis, respiration, fossil fuel use, forest fire, and ocean temperature. Photosynthesis on land removes CO_2 from the atmosphere, whereas respiration and combustion return CO_2 to the atmosphere. On average, the oceans constitute a CO_2 sink (Siegenthaler and Sarmiento, 1993), but that average includes large regional and interannual differences. Tropical-ocean surface waters typically are warm and have low CO_2 solubility, but, in the eastern tropical Pacific, they are cool and CO_2 rich; so that CO_2 generally is released into the atmosphere from tropical oceans. Higher latitude waters are cooler, have higher CO_2 solubility, and thus they are CO_2 sinks. On seasonal time scales, CO_2 variations mostly reflect the metabolic activity of terrestrial plants and soils (Nemry et al., 1996), especially in the Northern hemisphere. In summer, photosynthesis dominates and decreases CO_2 concentrations, whereas, in winter, respiration dominates and increases CO_2 (see Fig. 1.5a). The terrestrial biosphere is a source of atmospheric CO_2 in winter and a sink in summer. Regardless of the season, however, the contribution of the terrestrial biosphere is always a difference between photosynthetic sinks and respiration sources. Photosynthesis by land plants increases with temperature but not as much, typically, as do plant and soil respiration (Keeling, Chin, and Whorf, 1996). Conversely, CO_2 from fire is more during the autumn (see Fig. 1.5b). Thus, warmer climates and longer growing seasons can lead to increased CO_2 concentrations. In contrast, (Knorr

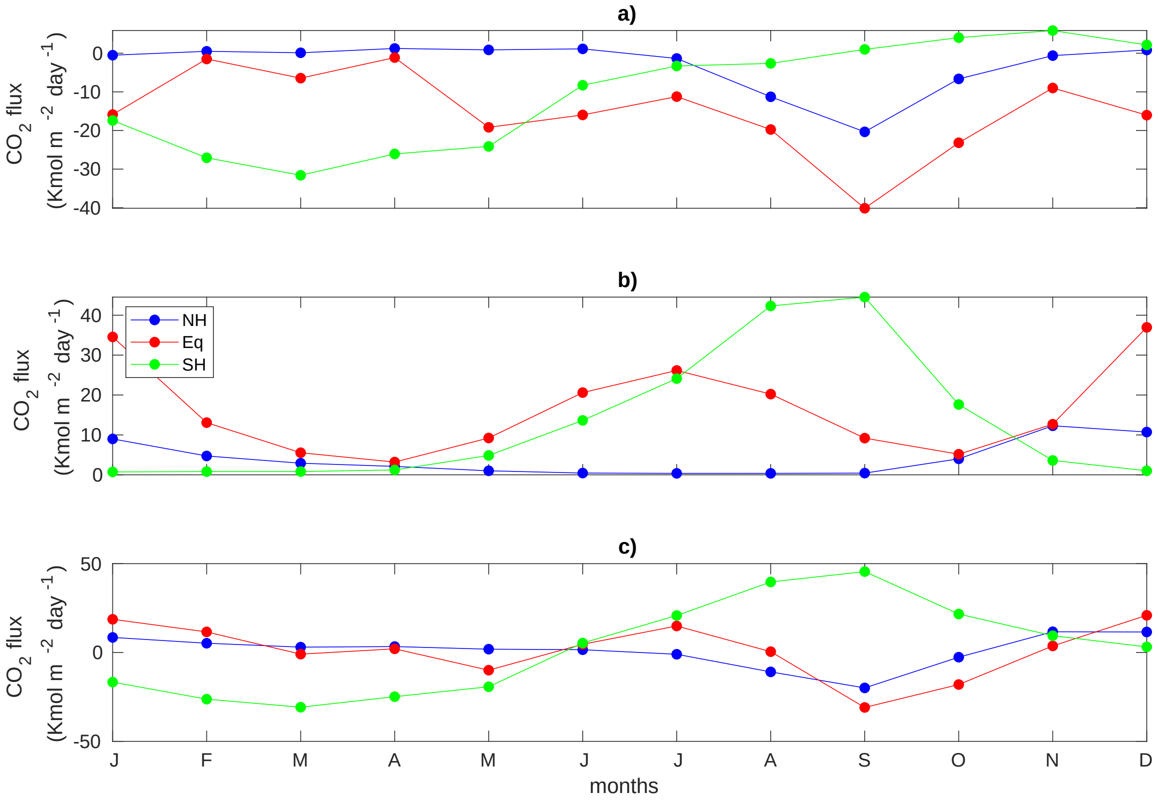

FIGURE 1.5: Seasonal amplitudes of NOAA Carbon Tracker CO_2 flux over Northern (10.5^0 *to* 35.5^0), Equatorial (-10.5^0 *to* 10.5^0) and Southern (-35.5^0 *to* -10.5^0) Africa during 2000-2016. a) CO_2 flux due to the biosphere atmosphere exchange. b) CO_2 flux due to the forest fire. c) net CO_2 flux due to the biosphere atmosphere exchange and forest fire.

and Heimann, 1995) finds that water availability has a limited net impact on the CO_2 seasonal cycle at mid-to-high latitudes. Ocean uptake of CO_2 varies seasonally (being a stronger net sink in summer when atmospheric CO_2 partial pressures are highest), but these variations are smaller than the terrestrial contributions (Ciais et al., 1996).

1.4 Drivers of carbon dioxide

1.4.1 Effects of El Niño and La Niña on CO_2 concentration

The tropical climate variability has largely impacted by ENSO at the interannual time scale. ENSO has a warm phase called El Niño and a cold phase called La Niña (Cane, 2005). Understanding the response of CO_2 flux to this natural climate phenomenon has a significant contribution in carbon cycle studies related to climate variability and, by extension, to the climate in general (Cox et al., 2013a). Due to the response of the terrestrial carbon cycle to El Niño induced changes in weather patterns, the global atmospheric CO_2 concentration increases substantially. More CO_2 has been added to the atmosphere during the strong El Niño events. In addition to the terrestrial component, the tropical Pacific Ocean also plays an important role in the carbon budget. Although the ENSO cycle starts from the equatorial Pacific region, it impacts the global carbon cycle through its regional teleconnection (Trenberth et al., 1998) and significantly influences the atmospheric and oceanic circulation, precipitation patterns and intensity, temperature, and fire emissions (Page et al., 2008). El Niño causes a rise in the temperature of the eastern Pacific Ocean, thus causing warming and drying of the tropical rainforest, which in turn affects the air-land CO_2 exchange. This phenomenon enhances carbon decomposition and forest fires, resulting a decrease in carbon-storing capacity of the tropical ecosystem. Particularly, fires are bad because they destroy the ecosystem and at the same time release high quantities of CO_2 to the atmosphere.

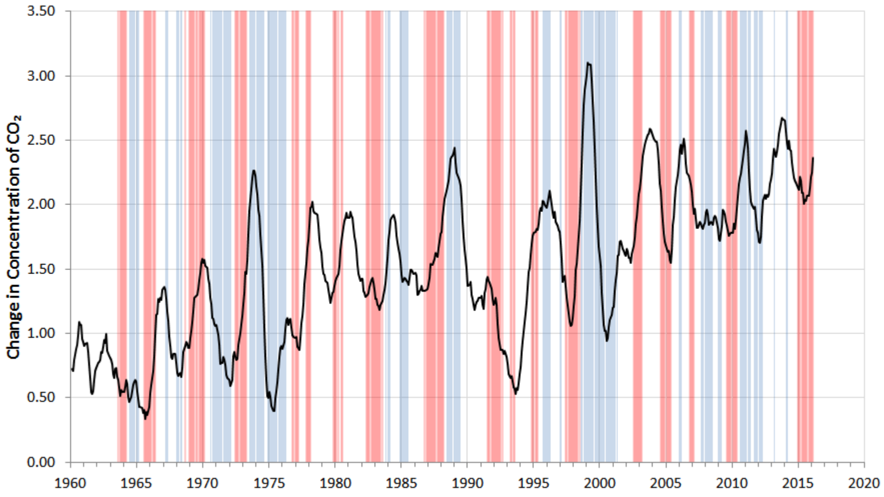

FIGURE 1.6: Trailing twelve-month average of year-over-year change in parts per million of atmospheric CO_2 versus El Niño (red) and La Niña (blue). Covering the periods from January 1960 - 2016. This figure is adapted from Political Calculations 2016.

Increases in terrestrial CO_2 sources during El Niños have been attributed to overall continental warming and (mostly tropical) drought associated with the warm tropical episode (Keeling, 1960); the opposite effects are attributed to La Niñas. Warmer than normal surface waters dominate the tropical Pacific during El Niños and displace the cooler but CO_2-rich waters that typically upwell from the equatorial undercurrent beneath the eastern equatorial Pacific (Murray et al., 1994). The influence of this displacement can reduce or even reverse CO_2 release from the tropical oceans and increase the net global oceanic uptake of CO_2 (Francey et al., 1995). As a consequence, the oceans are a stronger CO_2 sink. Usually, however, the increases in terrestrial sources of CO_2 during El Niños dominate and atmospheric CO_2 concentrations increase during the warm episodes (see Fig. 1.6). Overall, during El Niños and thus, when tropical SSTs are warm, the oceans contribute to lower CO_2 concentrations.

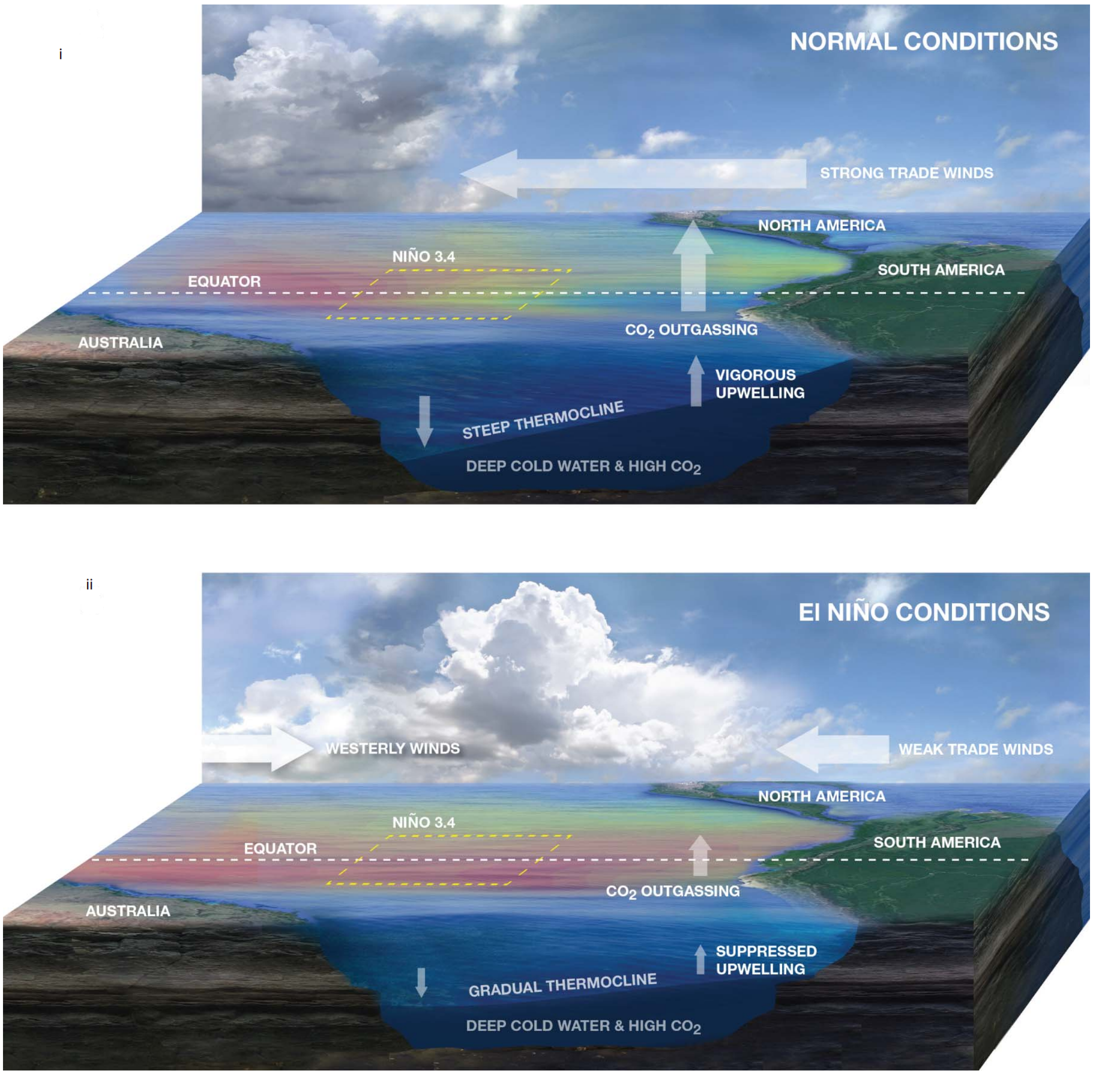

FIGURE 1.7: Schematic of the mechanistic differences between normal (upper panel) and El Niño conditions (bottom panel) and associated carbon response over the tropical Pacific Ocean. Warm ocean surface temperatures are denoted in red, cooler waters in blue. This figure is adopted from Chatterjee et al. (2017).

During strong El Niño events, there is a large-scale weakening of the easterly trade winds and suppression of eastern equatorial Pacific up-welling that can potentially reduce the supply of cold carbon-rich waters to the surface (Fig. 1.7). During El Niño conditions, easterly trade winds weaken and westerly wind bursts occur. Following the shift in wind direction, the western tropical Pacific warm water moves towards the east and the slope of the thermocline becomes flat in the eastern and central tropical Pacific. This suppresses up-welling of the cold carbon-rich waters in the eastern and central tropical Pacific, decreasing the amount of CO_2 out-gassing into the atmosphere. Fig. 1.7 also shows there is a change in atmospheric convection during El Niño event, wherein convection shifts eastward in response to the eastward displacement of the western tropical Pacific warm water pools. This strongly reduces the usual outgassing of CO_2 from the region (Feely et al., 1995), typically on the order of 0.4 to 0.6 Pg C year^{-1} to the atmosphere by $\approx$ 40 to 60% reduction (Takahashi et al., 2003). Understanding these variations in atmospheric CO_2, and the primary processes that cause the variation to become a great interest in the study of carbon cycle (Bousquet et al., 2000). In this thesis, we investigated the response of natural CO_2 flux over tropical Africa during El Niño.

1.4.2 The role of temperature on CO_2 concentration

The change in the Earth's surface global temperature is commonly considered to be driven by an increase of CO_2. However, the situation is more complicated and controversial conclusions have been suggested by the field experts. For example, Keeling et al. (1995) showed that the atmospheric concentration of CO_2 does not follow the rate of its industrial emissions. There had no growing trend in the global mean temperature estimated from the five datasets in the years (2000-2013) (see Fig. 1.8), despite the observed growing trend in CO_2 (Le Quere et al., 2013). Humlum, Stordahl, and Solheim (2013) also shows such an inverse phase relation between the trends of temperature and atmospheric CO_2, suggesting the temperature changes were not strongly caused by changes in the atmospheric CO_2 concentration. In contrast, Richardson (2013) investigated the temperature trend followed the trend of atmospheric CO_2. The time series of the globally averaged atmospheric CO_2 and the global temperature anomaly shows the temperature trend in the 21^{st} century that does not follow the rise of CO_2, although it has been close to the CO_2 trend during the previous 30 years. Fig.1.8 also depicts warming has not been significant, nor does it follow with CO_2 rise, especially in the years 2002-2014 when it has flatlined and some reviewers see a cooling trend until the recent 2015/16 El Niño occurred.

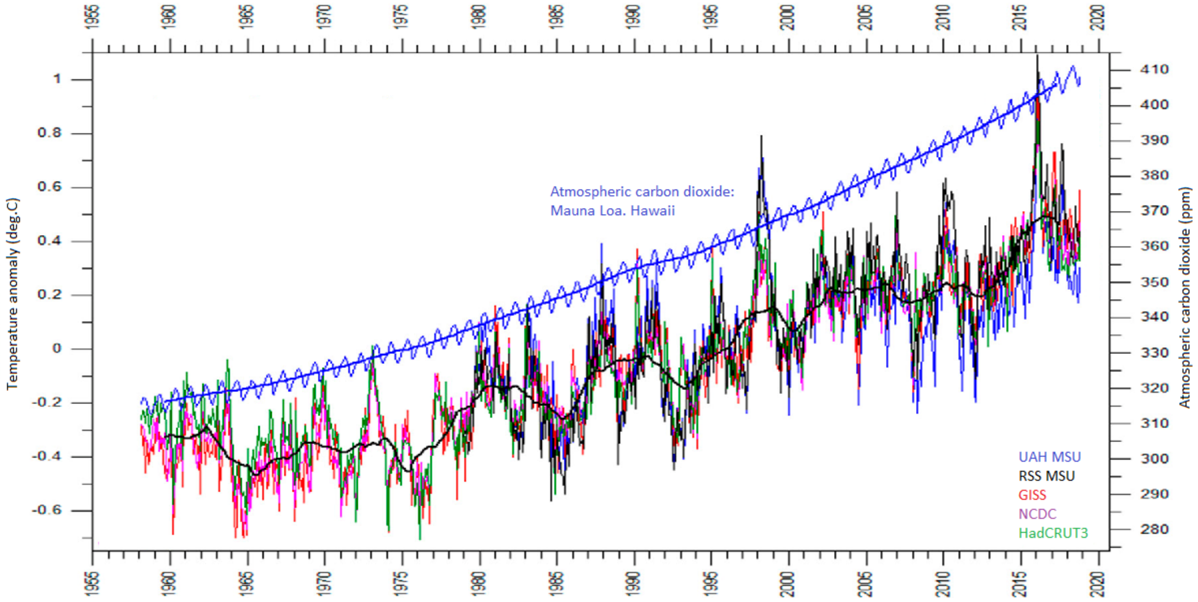

FIGURE 1.8: Monthly and running 37 months average of global temperature estimates and atmospheric CO_2 concentration. Blue zigzag line indicates a steady rise in CO_2 and five multicolored lines are global average temperature anomaly from five datasets. This figure is adopted from Boretti and Florentine (2019)

The land vegetation controls carbon fluxes between the atmosphere and terrestrial exchange (Bonan, 2008) and has a significant role in regulating the climate. Plant photosynthesis and respiration are the most dominant terrestrial carbon fluxes, and the net balance of these two processes determines carbon-based ecosystem (Beer et al., 2010) and can buffer Earth's climate from anthropogenic CO_2 emissions. For whole-plant or canopy gas exchange, it has been investigated that photosynthesis (GPP, carbon sink) and autotrophic respiration (TER, carbon source) are sensitive to temperature (Houghton and Woodwell, 1989). The concept that plant respiration is highly temperature-dependent is primarily based on short-term responses of plants to changes in temperature. Temperature can significantly affect most of the plant physiological processes. For example, it has a direct influence on stomatal conductance, particularly at high temperatures (Teskey et al., 2015). Stomatal conductance plays a key role in determining the rate of net photosynthesis and, therefore, the global carbon cycle and plant carbon metabolism. As a result, stomatal stabilization is one of the main factors which determine the local growth and survival of plants and global cycles of mass and energy.

1.4.3 The role of rainfall on CO_2 concentration

Rainfall and atmospheric temperature are among the major drivers of the terrestrial carbon cycle, and can strongly affect ecosystem processes such as photosynthesis and respiration (Guntinas et al., 2013). Climate change is commonly manifested by changes in precipitation's pattern and intensity (Smith et al., 2008). The intensity and patterns of precipitation affect the biological activity of plants and soil moisture content, which in turn influence atmospheric CO_2 balance. Spatio-temporal variability in rainfall strongly controls CO_2 source and sink strength of the biosphere and therefore also contributes to climate change (Cox et al., 2000). Spatio-temporal variability in rainfall patterns affects the eco-physiological processes. Generally, plant productivity increases following relatively larger rainfall pulses or a series of small pulses, which results in a larger CO_2 uptake by the vegetation (Wu et al., 2016). In contrast, periods of inadequate rainfall leading to drought conditions bring about a progressive decrease in soil water availability to plants and cause premature plant death, drought stress can enhance plant metabolism activity to adjust for water stress, driving to intensify plant respiration (Bhargava and Sawant, 2013).

1.4.4 Soil moisture and CO_2 concentration

The global carbon stock of soils is estimated at 1500 Pg. This amount is about double to that of atmospheric CO_2 concentration and three times the amount estimated in the vegetation (Batjes, 1996). Therefore, a small emission from this large carbon reservoir could have significant impacts on the concentration of atmospheric CO_2. Soil moisture condition is one of the major abiotic factors that drive the exchange of carbon, water, and energy between the land surface and atmosphere (Gentine, Entekhabi, and Polcher, 2011; Jung et al., 2010).

Soil can be a major sink or source of atmospheric CO_2 with soil moisture being a main driving force. The emission of CO_2 from the soil is mainly caused by the decomposition of decaying plant and organic matters in the soil by bacteria and microorganisms which produces a small amount of hummus and a large amount of CO_2 in the subsurface. Soil moisture can also determine how much water can be extracted by plant roots. Along with temperature and concentration of organic matter, soil moisture influences the transport of carbon from the land into the atmosphere. Moreover, it can regulate stomatal conductance, which in turn determines plant carbon uptake and their water status (Anderegg et al., 2012; Stocker et al., 2018); indicating the rate of photosynthesis is largely driven by the root zone soil moisture content.

Soil moisture condition also controls heterotrophic respiration which is responsible for about half of the atmospheric CO_2 emissions from soils (Yan et al., 2018; Zhang et al., 2018a); much of the CO_2 generated by heterotrophic respiration will diffuse from the soil into the atmosphere whereas some of the CO_2 partitions into groundwater affecting the carbonate chemistry and as a result lowering the pH. When the CO_2 saturated groundwater comes in contact with water that is exposed to the atmosphere, and then CO_2 will equilibrate and outgas into the atmosphere just like opening a bottle of carbonated soft drink. Low soil moisture can trigger microbial dormancy and reduce the transport of solute matters; which potentially limit the rate of heterotrophic respiration (Yan et al., 2018; Zhang et al., 2018a).

Soil moisture also plays a role in regulating surface temperature as evaporation is a more effective cooling mechanism than sensible heating (Bateni and Entekhabi, 2012). Low soil moisture causes the surface temperature to rise and thereby enhance respiration (Green et al., 2019). For example, in arid desert regions where soil moisture is very low, microbial activity in soil decreases. Overall, the response of soils plays a significant role when assessing the climate-feedback of carbon. Therefore, it is important to gain further insight into the dynamics of CO_2 flux from the soil. Despite, model estimates of soil moisture may be prone to large uncertainties due to the limited understanding of the land-atmosphere feedback mechanism (Taylor, Stouffer, and Meehl, 2012) studies relay on it to study trends and dynamics of soil moisture (Zhu, Cavazos, and Lettenmaier, 2007; Sheffield and Wood, 2008).

1.5 Observations and modeling of carbon cycles

1.5.1 Estimation of GPP from fluorescence

Top-of-atmosphere radiance measurements contain the contributions of many components. Space-based spectrometers observing this spectral region with sufficient spectral resolution and signal-to-noise ratio can detect the SIF signatures in top-of-atmosphere (TOA) reflectance spectra. During photosynthesis, most of $\approx$ 80% of the harvested energy (bright minus dark yellow) is used for photosynthesis. $\approx$ 19% is dissipated as heat (purple) and a small fraction of energy $\approx$ 1% is reemitted as fluorescence at a higher wavelength compared to the absorption (Schlau-Cohen and Berry, 2015) (red). (Fig. 1.9). This Sun-Induced

Fluorescence has a spectrally smooth signature with peaks around 683 (red fluorescence) and 736 nm (far-red fluorescence). Chlorophyll itself reabsorbs radiation of wavelengths below 700 nm. Photons that escape reabsorption and travel through the atmosphere and can be detected by satellites (see Fig. 1.10). As a result of recent advancements in space-borne observatories, numerous methods have been developed to separate the small sun-induced fluorescence fingerprints from earth-shine spectra (Frankenberg et al., 2011; Frankenberg et al., 2012; Joiner et al., 2016; Köhler et al., 2018). Initially, the retrieval method relied on measuring the filling-in of solar Fraunhofer lines, which needs a very high spectral resolution technique (typically $< 0.05\ nm$) to resolve the individual Fraunhofer line structure. This method has been applied to space-based instruments like the Global Ozone Monitoring Instrument 2 (GOME-2) (Joiner et al., 2013).

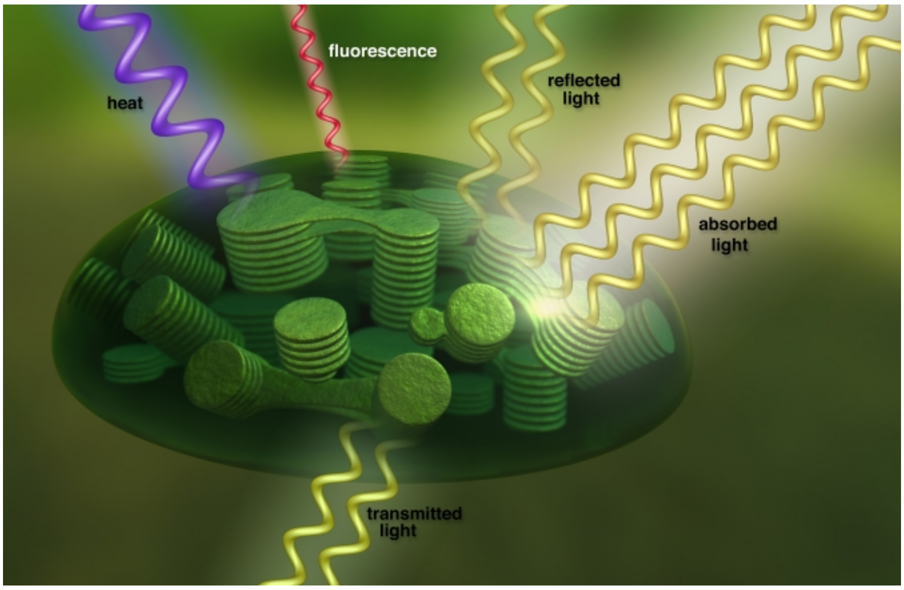

FIGURE 1.9: Photosynthetic mechanism within the chloroplast of plant cell emitting fluorescence in the process of sunlight to energy conversion. This diagram is adopted from NASA Goddard's Conceptual Image Lab/T. Chase.

The SIF retrieval used in this thesis is based on a statistical algorithm, developed by (Joiner et al., 2013). A forward model is constructed to explain the top-of-atmosphere reflectance spectrum in the near-infrared (NIR) region (in clear-sky situations) as a superposition of an isotropic fluorescence emission term, an isotropic reflecting ground surface, and atmospheric transmittance (from e.g. water vapor). Rayleigh scattering is assumed to be negligible in the NIR wavelength region (Frankenberg et al., 2012) The monochromatic reflectance (R) can be written as:

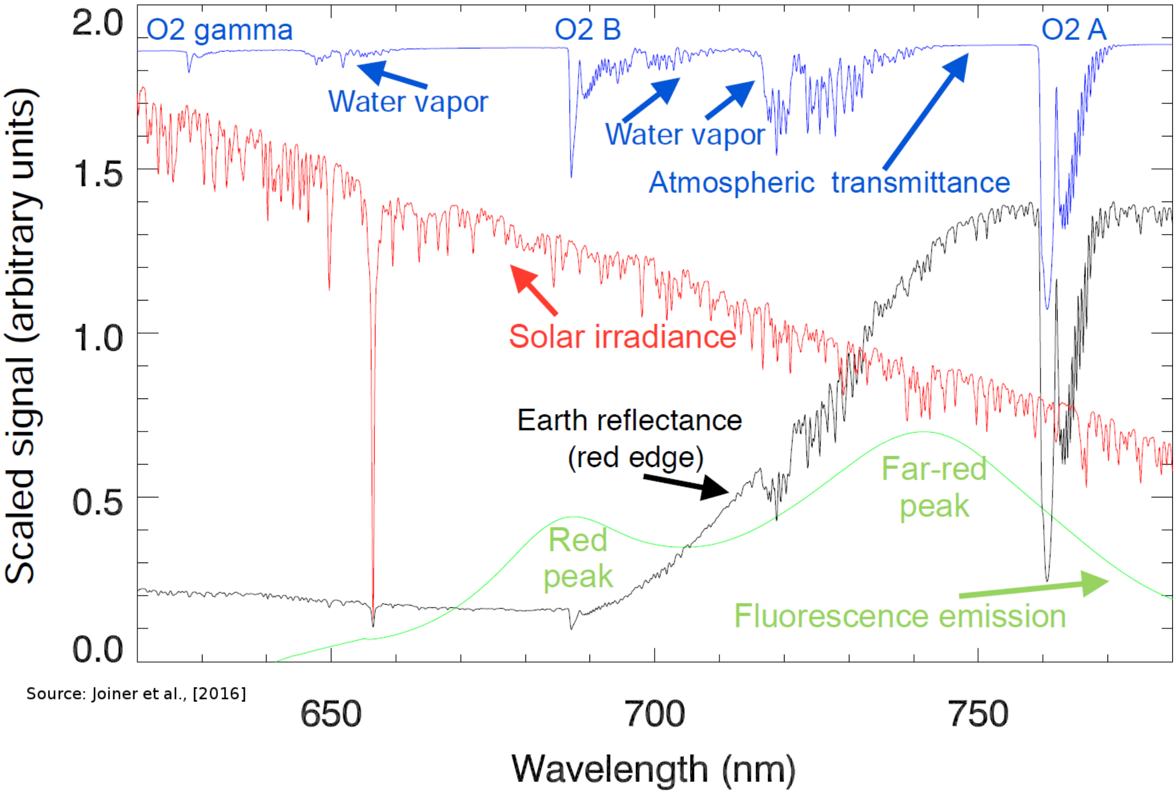

Source: Joiner et al., [2016]

FIGURE 1.10: Simulated terrestrial spectra on its way through the atmosphere in a wavelength rage from 600-800 nm. This figure is adopted from Joiner et al. (2016)

$$R(\lambda, \mu, \mu_0) = A_s(\lambda)T^{\uparrow}(\lambda, \mu)T^{\downarrow}(\lambda, \mu) + \frac{\pi I_F(\lambda)T^{\uparrow}(\lambda, \mu)}{\mu_0 E_0(\lambda)} \tag{1.1}$$

where A_s is the surface albedo; $T^{\downarrow}$ and $T^{\uparrow}$ are the downward and upward atmospheric transmission factors, I_F is the fluorescence emission, μ_0 and μ are the cosines of solar zenith and the viewing angles respectively; E_0 is the solar irradiance at the top of the atmosphere.

The upwelling fluorescence radiance is parameterized as Gaussian curve with its peak located at $(\lambda_F) = 737.0nm$ and a sigma-width $(\sigma_F)(F) = 33.9nm$ following (Zarco-Tejada et al., 2000). Hence,

$$I_F(\lambda_i) = I_{F0}\exp(\frac{-1}{2}[\frac{\lambda_i - \lambda_f}{\sigma_f}]) \tag{1.2}$$

The above procedure provides a level-2 SIF data. A linear relationship can be established between SIF and GPP with the formulation based on the concept of light use efficiency (Monteith, 1972):

$$GPP = APAR \times LUE_p \tag{1.3}$$

where APAR is the absorbed photosynthetically active radiation expressed in radiance units and LUE_p is the light use efficiency of photosynthesis, which represents the efficiency of energy conversion for gross CO_2 assimilation. Similarly, SIF can be expressed as:

$$SIF = APAR \times LUE_f \tag{1.4}$$

where LUE_f is the effective light use efficiency of canopy fluorescence, which accounts for both the fluorescence yield and the fraction of emitted photons escaping the canopy (Damm et al., 2015).

A more recently developed index, NIRv, is the product of the total scene near-infrared reflectance (NIRT) and the NDVI is found to be less sensitive to background contamination and is well related to GPP (Badgley, Field, and Berry, 2017).

1.5.2 Flux partitioning algorithm

Eddy covariance technique measures the net fluxes of CO_2 and other trace gases, as well as energy and water fluxes at the ecosystem level. However, particularly for CO_2 exchange, a lot more understanding of the biosphere is gained, when the net ecosystem flux is partitioned into the main components: gross primary production and terrestrial ecosystem respiration. Based on the fact that plant photosynthesis is zero during night time, flux partitioning algorithms separate the net carbon exchange into photosynthetic uptake and respiratory release. The first step in the flux partitioning algorithm is to estimate the temperature sensitivity E_0 in (°C) using nighttime data when the global radiation (R_g) is below 4 W m^{-2}. Here, to account for seasonality, a moving window approach is proffered to estimate the parameter. For example, estimating parameters every two days with a 4-day moving window when using the daytime data and a 12-day moving window when using nighttime data is the recommended approach (Lloyd and Taylor, 1994). Then the seasonal course reference temperature (T_{ref}) is usually kept to 15°C throughout the year. Finally, the net ecosystem fluxes (NEE) are partitioned into GPP and R_{eco} using the estimated E_0 and T_{ref}. There are two widely used approaches for flux partitioning: Nighttime partitioning (Reichstein et al., 2005) fits nighttime NEE data with a respiration model and daytime partitioning (Lasslop et al., 2010) combination of a light response curve and a respiration model to fit daytime NEE. Both flux partitioning algorithms described here are also available as online tools at `http://www.bgc-jena.mpg.de/~MDIwork/eddyproc/`. Here, we present the daytime partitioning approach. NEE was modelled using the common principles of the rectangular hyperbolic light response curve (Falge et al., 2001) as:

$$NEE = \frac{\alpha \beta R_g}{\alpha R_g + \beta} + \gamma \tag{1.5}$$

where α (μmol C J^{-1}) is the canopy light utilization efficiency and represents the initial slope of the light response curve, β (μmol C m^{-2} s^{-1}) is the maximum CO$_2$ uptake rate of the canopy at light saturation, γ (μmol C m^{-2} s^{-1}) is the ecosystem respiration and R$_g$ is the global radiation (W m^{-2}). The light response curve is extended to account for the temperature sensitivity of respiration by replacing the constant respiration γ in Eq. 1.5 with a respiration model, in this case, the (Lloyd and Taylor, 1994) model and a drought limitation of GPP (Gilmanov, Johnson, and Saliendra, 2003). The hyperbolic light response curve is modified as:

$$NEE = \frac{\alpha \beta R_g}{\alpha R_g + \beta} + r_b exp(E_0(\frac{1}{T_{ref} - T_0} - \frac{1}{T_{air} - T_0})) \tag{1.6}$$

where r$_b$ (μmol C m^{-2} s^{-1}) is the base respiration at the T$_{ref}$ computed as the mean of nighttime NEE, T$_{air}$ is the air temperature, and T$_0$ is a temperature constant parameter kept at -46.02°C) and the accepted values of the above parameters during the estimation procedure can be found in (Lasslop et al., 2010).

Furthermore, to account the Vapor Pressure Deficiency (VPD) limitation of GPP. The fixed parameter β in Eq. 1.6 was replaced with an exponential decreasing function (Körner, 1995) for β at high VPD as:

$$\beta = \left\{ \begin{array}{ll} \beta_0 exp(-k(VPD - VPD_0)), & \text{for } VPD > VPD_0 \\ \beta = \beta_0, & \text{for } VPD < VPD_0 \end{array} \right\}$$

where k is the response of the maximum carbon uptake to VPD computed from daytime data and VPD$_0$ was the threshold VPD set to 10 hPa in accordance with previous findings at leaf level (Körner, 1995).

1.5.3 Modeling of carbon flux

The direct measurement of carbon flux requires either an eddy covariance measurement technique at multiple height levels or measurements of concentration changes in a sealed volume of air (Foken, Aubinet, and Leuning, 2012). These bottom-up approaches of direct observation are only representative for a given collection of biomes in a limited region. Therefore, inverse modelling of the CO$_2$ concentration gradients observed in the Earth's atmosphere is important to quantify the spatiotemporal distribution of the net CO$_2$ fluxes (Peters et al., 2007; Peylin et al., 2013; Chevallier, 2015). For that reason, different data assimilation techniques were developed. For example, the NOAA's state-of-the-art data assimilation system for carbon dioxide, called Carbon Tracker, estimates the surface carbon flux from a set of CO_2 mole fraction observations in the global atmosphere. The Carbon Trackers start data assimilation by forecasting global atmospheric XCO_2 from a combination of CO_2 surface exchange models and an atmospheric transport model driven by meteorological fields from the European Centre for Medium-Range Weather Forecasts (ECMWF) (Peters et al., 2007). Then a three-dimensional CO_2 distribution is sampled both in time and location where observations are available, and then the difference between the model forecasts and observations is minimized.

The aim of data assimilation techniques is to infer a state vector x[dimension s] that contains spatiotemporal binned surface fluxes or a related quantity such as scaling factors for an initial guess flux field. The systems exploit measurements of the atmospheric concentration from an observation vector y[m] with covariance R[m x m] and a priori knowledge contained in the background state variable x^b[m] with covariance B[s x s]. Fluxes and measured concentrations are linked through the observation and transport operator H, which is linear for the case of CO_2 flux inversion. The observation operator H samples the state vector x[s] and returns a vector [m] to be compared to the observations. The maximum probable solution of the unknown variables in the state vector of fluxes x[s] is determined by minimizing a cost function J that typically consists of two terms, the mismatch between measured and modelled observations and the mismatch between the fluxes to be estimated and the background estimate:

$$J = (y - Hx)^T R^{-1} (y - Hx) + (x - x^b)^T B^{-1} (x - x^b) \tag{1.7}$$

with R and B define the relative weights of the observation and background mismatch respectively.

Minimizing Eq. 1.7 by means of matrix algebra (Rodgers, 2000) gives the optimized flux and its covariance:

$$x^a = x^b + BH^T (HBH^T + R)^{-1} (y - Hx^b) \tag{1.8}$$

$$B^a = B - BH^T (HBH^T + R)^{-1} HB \tag{1.9}$$

where x^a is the a posteriori state vector and B^a the respective covariance matrix.

The principle behind Carbon Tracker data assimilation is an inverse modelling approach based on Ensemble Square Root Filter (EnSRF) developed by Peters et al. (2005). EnSRF determines optimized surface flux sequentially in a time step with x_t defines a subset of x for a certain time window instead of minimizing in one step. The Kalman gain matrix K[s x m] commonly defined as:

$$K_t = (B_t H_t^T)(H_t B_t H_t^T + R_t)^{-1} \tag{1.10}$$

with the gain matrix Eqs. 1.8 and 1.9 read as

$$x_t^a = x_t^b + K_t(y - H_t x_t^b) \tag{1.11}$$

$$B_t^a = B_t - K_t H_t B_t \tag{1.12}$$

where t is a subscript for time, indicates quantities of reduced dimensions for the time step under investigation, the superscript b refers to background quantities and a to the analyzed variable. Once the variable is analyzed for time slice t, it is used as a background to estimate the next time slice $t + 1$. such as:

$$x_t^b + 1 = x_t^a \tag{1.13}$$

Therefore, given an initial guess for the first background state allows sequential calculation of the state vector x.

1.6 Past attributes of the study

There have been many previous studies examining the dynamics of CO_2 flux (Reichstein et al., 2005; Peters et al., 2007; Stocker et al., 2013), but almost all of them have focused on a global scale or on the developed countries and ignored or poorly considered the role of Africa in the carbon-climate feedback. Africa was responsible for an average emission of 500 Tg C y^{-1} for the period covering from 2000 to 2005 (Canadell, Raupach, and Houghton, 2009). These emissions are mainly anthropogenic CO_2 from fossil fuels and cement manufacturing industries (260 Tg C y^{-1}) and land degradation (240 Tg C y^{-1}). Africa's stock of global emissions from land-use change was estimated at 17%. This suggests that Africa has a significant and growing role in the global carbon budget, and it is likely that a sizable fraction of the observed interannual variability of the global carbon cycle (Cox et al., 2013b; Ballantyne, Ciais, and Miller, 2018) can be attributed to the African continent (Williams et al., 2007). Despite its global and regional importance, this continent has few environmental observation networks (Fisher et al., 2013) leaving so-called global atmospheric CO_2 inversions (Peters-Lidard et al., 2007; Peylin et al., 2013; Gaubert et al., 2019) poorly constrained. This leaves Africa as the most uncertain and most error-prone part of such flux estimates.

Changes in atmospheric temperature, hydrology, sea ice, and sea levels are attributed to climate forcing agents dominated by CO_2 (Santer et al., 2013; Stocker et al., 2013). However, understanding the climate response to anthropogenic forcing in a more traceable manner is still difficult due to a major uncertainty in carbon-climate feedback (Friedlingstein et al., 2006). Part of this uncertainty is due to a lack of sufficient data on the regional and global carbon cycle. This is compounded with inappropriate modelling practices to capture the spatiotemporal variability of the carbon cycle. These problems can be solved through strengthening carbon monitoring networks, setting up proper modelling, and reducing uncertainties in satellite retrieval.

Towards this, a number of national and international efforts have been initiated in the recent past by different governments and non-government agencies across the globe. Among these efforts, ground-based observations of greenhouse gas using Total Carbon Column Observing Network (TCCON) are a notable one since it provides accurate and high-frequency measurements of column-integrated CO_2 mixing ratio. For example, it has been established that TCCON has a precision of 0.25% for measurements taken under clear sky conditions (Wunch et al., 2011). However, the number of TCCON sites is limited and cannot establish an accurate CO_2 amount and flux on a subcontinental or regional scale. Moreover, some studies show that the large uncertainty is amplified due to the uneven global distribution of TCCON sites (Velazco et al., 2017). In addition, none of these ground-based observation networks was found in Africa's landmass. However, there are few TCCON sites around the continent plus some flask observations in and around Africa. For example, the TCCON station on Ascension Island records the direct solar absorption spectra of the atmosphere in the near-infrared and retrieved accurate and precise column-averaged abundances of atmospheric constituents including CO_2, CH_4, N_2O, HF, CO, H_2O, and HDO (Feist et al., 2014).

On the other hand, the CO_2 concentration retrieved from the satellite-based CO_2 absorption spectra has the advantages of being unified, long-term, and global observation as compared to ground-based measurements. Recently, satellite observations of XCO_2 have received much attention because of their nearly global coverage and high temporal and spatial resolution (e.g., Kulawik et al., 2016; Yoshida et al., 2011; Crisp et al., 2012; O'Dell et al., 2012) and satellite-retrieved $\mathrm{CO_2}$ data are now used together with ground-based observations in inverse modelling studies for regional carbon flux estimation (e.g., Maksyutov et al., 2013; Saeki et al., 2013). It has been established from theoretical studies that accurate and precise satellite-derived atmospheric CO_2 can appreciably minimize the uncertainties in the estimated CO_2 surface flux (Rayner and O'Brien, 2001; Chevallier, 2007). Other studies have revealed that significant improvement in the estimation of weekly and monthly CO_2 fluxes can be achieved subject to CO_2 retrieval error of less than 4 ppm from the satellite and a modelling scheme, whereby CO_2 concentration is an independent parameter of the carbon cycle model (Houweling et al., 2004; Hungershoefer et al., 2010). However, XCO_2 shows temporal variability on different time scales: diurnal, synoptic, seasonal, inter-annual, and long-term (Olsen and Randerson, 2004; Keppel-Aleks, Wennberg, and Schneider, 2011). More recent missions such as GOSAT (Hamazaki et al., 2005), OCO-2 (Boesch et al., 2011), and planned missions such as the Active Sensing of CO_2 Emissions over Night, Day, and Season (ASCENDS) (Dobbs et al., 2008) have been and are being developed specifically to resolve surface sources and sinks of CO_2 and provide information on these different scales of temporal variability. For example, GOSAT observations started in 2009 and provide XCO_2 based on spectra in the Short-Wavelength InfraRed (SWIR) region with a standard deviation of about 2 ppm with respect to ground-based and in-situ air-borne observations (Yokota et al., 2009; NIES GOSAT Project, 2012). The performance and bias of XCO_2 retrieval from an algorithm could change in different regions with differing land surfaces and anthropogenic emissions (Bie et al., 2018).

Interannual climate variability also induces a considerable change in net biomass productivity and African's savanna fire emissions. Considering the African's sizeable carbon stock, its seemingly high vulnerability to anticipated climate and land-use change, as well as growing populations and industrialization, Africa's carbon emissions and its interannual variability are likely to undergo substantial increases through the 21^{st} century (Williams et al., 2007). Although anthropogenic CO_2 releases have been rising since the industrial revolution, only about half of these remained in the atmosphere (Menon et al., 2007; Peters et al., 2012). The remainder of anthropogenic CO_2 emissions have been taken up by so-called carbon sinks, mainly the oceans and land biosphere (Peters et al., 2012). However, this CO_2 intake by the terrestrial biosphere and the Ocean significantly varies from year to year. Therefore, anthropogenic carbon dioxide emissions and its changes in the atmosphere require an excellent estimate of the associated source and sinks, together with the attribution factors responsible for the change.

Terrestrial gross primary production, the amount of carbon absorbed by terrestrial plants via photosynthesis, constitutes the largest CO_2 flux between the terrestrial biosphere and the atmosphere (Quéré et al., 2015; Beer et al., 2010). It dominates the interannual variability of the terrestrial ecosystem carbon uptake and as a consequence of fertilization, it is likely to continue its substantial increase and play an important role in the carbon-climate coupling (Vermote et al., 1997; Le Quéré et al., 2015). Therefore, quantification of the spatiotemporal variations in GPP is important to assess biogeochemical cycling in the terrestrial biosphere, ecosystem functioning, carbon budget, and food production in the context of global climate change. Accurate quantification of GPP is still a challenge, although it scales beyond that of a single ecosystem, due to the lack of a reliable GPP signal that can be observed worldwide. Especially in highly productive tropical regions, the lack of both large-scale GPP signals and local measurements leads to a lack of understanding of how environmental changes drive carbon exchange. As a result, we can only crudely describe the carbon balance of these regions in the current and future climate.

Arguably, the most reliable measurements of NEE come from the eddy covariance technique (Baldocchi et al., 2001). However, there are still uncertainties in the partitioning of the measured net ecosystem exchange flux into GPP and respiration (Reichstein et al., 2005; Lasslop et al., 2012). Furthermore, the eddy covariance technique only provides measurements over a restricted area covered by its observation footprints with sizes and shape that vary with tower height, canopy physical characteristics, and wind velocity and by the limited and biased spatial distribution of towers across the globe (Schimel et al., 2015). In Africa, there are relatively few eddy covariance measurement sites and the data from these towers often suffer from gaps in their observational records. On the other side, terrestrial and ecosystem models can simulate GPP over varied spatial and temporal scales all over the globe, but the reliability of such calculations heavily depends on both the input data and the model formulation, which often are not specific for African (or Tropical) biomes. For example, Fisher et al. (2013) estimated the average GPP of the African tropical forest ranged from 1.4 to 4.0 kgC m^{-2} yr^{-1} (Ardö, 2015), indicating a large variability among nine global dynamic vegetation models.

On the modelling front, the Max Planck Institute of Biogeochemistry and FLUXCOM are notable. Model products have good spatio-temporal coverage, but they are highly susceptible to uncertainties due to their background modelling assumptions and uncertainties in the input meteorological data. This fuels the need for GPP estimation from direct measurements that have higher accuracy and do not rely on other meteorological inputs. Satellites measure the light emitted by chlorophyll and bypass through the atmosphere. The remotely sensed vegetation reflectances show a strong linear correlation with gross primary productivity and the linear relation also strongly diverges across biomes (Badgley, Field, and Berry, 2017; Joiner et al., 2013). This biome dependent relation between fluorescence and GPP is a challenge for empirical estimation of GPP from these signals at a regional scale and therefore strengthening the ground network observation across biomes provides an opportunity to directly estimate vegetation productivity and crop reduction over different localities (Duveiller et al., 2019). Most recent satellite missions such as OCO-2, GOSAT, GOME-2, TROPOMI, and in the future FLEX, put numerous efforts into inferring GPP from SIF with the goal of creating a global map of biosphere-atmosphere interaction at high resolution and accuracy. With the objective of improving the modelled biogeochemical processes in Earth System Models and monitoring the response of the biosphere to disturbance, recent efforts focus on acquiring persistent measurements of SIF at a regional scale from Geostationary Carbon Cycle Observatory (GeoCarb) (Duveiller et al., 2019).

In addition, atmospheric CO_2 concentration exhibits a very distinct seasonal cycle, which is mainly driven by the terrestrial biosphere uptake and release processes (Idso, Idso, and Balling Jr, 1999). For example, the seasonal variability of atmospheric CO_2 is mainly influenced by the weather conditions and associated CO_2 exchange processes over the terrestrial biosphere (Mengistu and Mengistu Tsidu, 2018; Idso, Idso, and Balling Jr, 1999).

In addition, atmospheric CO_2 exhibits interannual and decadal variability associated with a large-scale disturbance of the terrestrial biosphere. Some of the factors that contribute to the interannual variability are changes in fossil fuel emissions, natural irregularities in climate and weather patterns, forest fires, droughts, floods, and volcanic eruptions, (Jiang et al., 2010; Zimov et al., 1999; Francey et al., 1995; Keeling et al., 1995). It has been shown that interannual variability is correlated with the occurrence of ENSO (Gurney et al., 2008). For example, previous strong El Niño events in the years 1982-1983, 1997-1998 and 2015-16 severely disrupted global weather, leading to major natural disasters (Zhang et al., 2018c; Chatterjee et al., 2017; Liu et al., 2017, and references therein). In addition, moderate to weak El Niño events during 2002-2003, 2004-2005, 2006-2007, 2009-2010 and 2014-2015 have driven the global carbon cycle

(Pomposi et al., 2018). Recently, Palmer et al. (2019) suggested that tropical Africa is an unexpectedly large net source of CO_2 to the atmosphere, maximizing at nearly 1.5 PgC/yr during the 2015/2016 El Niño event. According to satellite products that retrieve column integrated CO_2 from the observed radiance, the northern hemisphere contributes most to the African carbon source. Hot-spots of emissions in the Congo basis and western Ethiopia, tentatively associated with high soil carbon densities, are partly responsible for this source. Suggesting that ENSO is the dominant driver of tropical climate variability at interannual (2 to 8 years) time scales and lasts for 3-12 months (Zhang et al., 2018b). The interannual fluctuation of atmospheric CO_2 is mainly driven by ENSO with a lag time of up to 6 months (Trenberth et al., 2002).

Even if the net exchange of carbon between land and atmosphere in individual regions is known to be affected during El Niño years, our understanding is limited to what causes these interannual variations (Field, Sarmiento, and Hales, 2007; Sabine et al., 2004) and many fundamental questions about the driving mechanisms and the resulting carbon fluxes remain open (Michalak et al., 2011; Peters et al., 2007). Moreover, it is not yet known in sufficient detail what the driving mechanisms are, how large the resulting carbon fluxes, and how they vary on regional scales. Previous studies on the relations of African climate and ENSO consider long time periods (usually more than 50 years). This is partly because these teleconnections are subjected to decadal fluctuations (e.g., Hoerling and Kumar, 2000; Philippon et al., 2007). Malhi and Wright (2004) noted that the number of temperature and precipitation from in-situ station climate data has become more scarce and less reliable in Africa than ever. In addition, satellite data do not adequately capture the climatology and variabilities of carbon flux (Mascorro et al., 2015; Doney and Schimel, 2007; Baldocchi et al., 1996). Moreover, high-resolution products are hard to find for a sufficiently long period of time. Therefore, model products that are sufficiently tuned by observation are more reasonable to study climatology in Africa. For these reasons, this study uses the NOAA Carbon Tracker CO_2 products to address some of the above scientific questions. CO_2 data from Carbon Tracker were found to exhibit excellent agreement with observations of TCCON (Kulawik et al., 2015) and latest CO_2 dedicated satellite results (e.g., GOSAT and OCO-2) (Mengistu and Mengistu Tsidu, 2019).

Chapter 2

Study area and Datasets

2.1 Description of the study area

Africa is under the influence of semipermanent high-pressure cells which lead to the Sahara Desert in the North and the Kalahari in the South. The equatorial low-pressure cell, which allows the formation of the seasonally migrating Inter-Tropical Convergence Zone (ITCZ), is part of the major large-scale atmospheric circulation systems. These large-scale pressure systems, oceanic circulations, and their interaction with the atmosphere coupled with the diverse topographies of the region allow for the formation of different climates (e.g., equatorial, tropical wet, tropical dry, monsoon, semi-desert (semi-arid), desert (hyper-arid), subtropical high climates). Geographically, the Sahel, a narrow steppe, is located just south of Sahara; the central part of the content constitutes the largest rainforest next to Amazon, whereas most southern areas contain savanna plains.

The continent gets rainfall from the migrating ITCZ, west Africa monsoon, the intrusion of mid-latitude frontal systems, travelling low-pressure systems (Mitchell, 2001, and references therein). Therefore, tropical Africa is characterized by a double rainfall maximum. However, in Tropical East Africa, the effect of altitude associated with the local topography results in a decrease of temperature and complex distribution of rainfall (Plisnier, Serneels, and Lambin, 2000). Vegetation response of tropical Africa is strongly controlled by this climatic condition (Stephenson, 1990) through the key processes of photosynthesis, respiration, and transpiration. Mainly the length of the dry seasons has a strong control of vegetation dynamics in the tropical regions (Ngomanda et al., 2009; Vincens, Garcin, and Buchet, 2007).

The concentration of CO_2 fluctuates in response to seasonal vegetation dynamics and associated climatic conditions of the region. Vegetation sensitivity of tropical Africa's landmass to climate extremes like EL Niño depends considerably on the vegetation type (Propastin, 2009). For example, Propastin (2009)

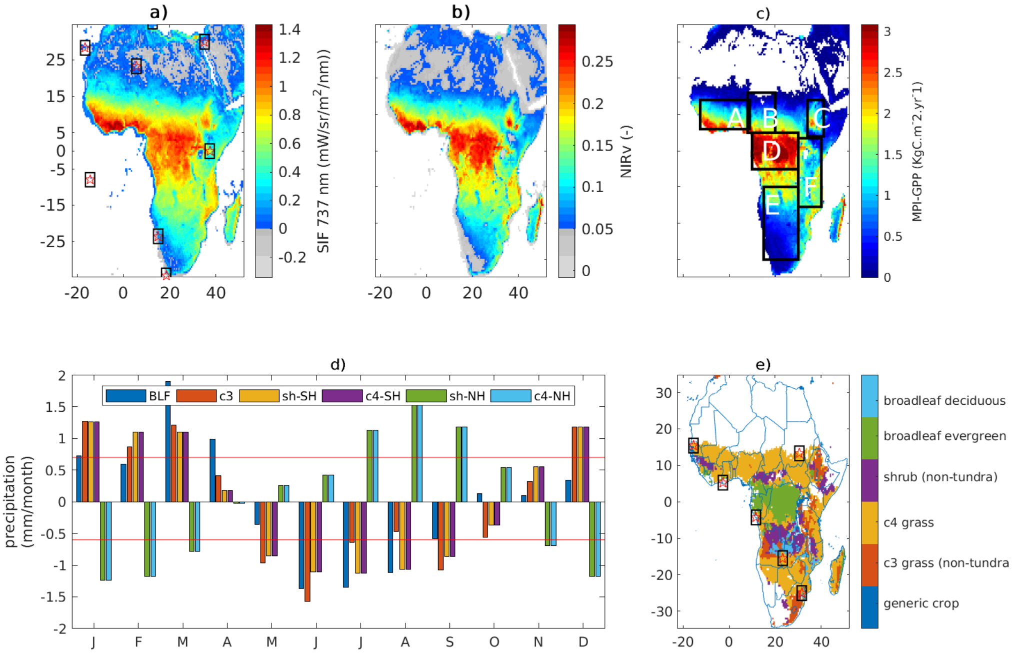

FIGURE 2.1: Annual mean SIF and NIRv averaged over the years 2007-2016 at 0.5° × 0.5° resolution, shown in (a) and (b) respectively. c) Climatology of gross primary production (Beer et al., 2010) at 0.5° ×0.5° resolution. d) Simple precipitation anomaly (SPA) computed from the multi-year GPCC monthly averaged precipitation covering the period from 1951 to 2000 for the major vegetation types of Africa. The red lines indicate thresholds for wet months SPA $\geq$ 0.7 mm month^{-1} and dry months SPA $\leq$ -0.6 mm month^{-1} and e) vegetation types from the terrestrial biosphere model SiBCASA and the white colour refers to none vegetated regions. The rectangle window with a pentagon star at the center in a) and e) shows the distribution of flask and flux towers respectively. The rectangular box in c) shows regions with the same climate according to the Köppen climate classification (Kottek et al., 2006). The letters represent subregions in tropical Africa; 'A' refers to tropical western Africa, 'B' refers to tropical North Africa, 'C' refers to Ethiopian Highlands, 'D' refers to tropical rainforest, 'E' refers to tropical Southern Africa and 'F' refers to tropical East Africa.

showed that tropical forest areas are more vulnerable to drought stress than other wooded and nonwooded vegetation categories. Zhang et al. (2018b) also showed that, at the interannual time scale, Net Biome Productivity (NBP) variability is dominant over semi-arid regions than over tropical forests. Vegetation types of Tropical East Africa range from tropical rainforest to desert. However, the region is mainly dominated by arid or semi-arid vegetation, and these arid and semi-arid vegetation types can tolerate aridity for several months as a result of the exceedingly low seasonal rainfall (Bobe, 2006). On the other hand, Western Africa is dominated by deciduous and semideciduous species with a herbaceous stratum, tree to shrub savannas, steppes and semidesert vegetation. While the central Africa regions are dominated by tropical rainforest (see Fig. 2.1c). Moreover, CO_2 fluxes exhibit seasonal variability and Africa experiences different seasons as noted above, it is important to divide Africa into three major regions, namely, North Africa (10 to 35 ^0N), Equatorial Africa (10 ^0S to 10 ^0N), and Southern Africa (35 to 10 ^0S). Based on their similarity in climate conditions according to the Kӧppen climate classification (Kottek et al., 2006), the amount of plant productivity per meter square, and the dominant vegetation type, we further clustered tropical Africa into six climatic zones labelled from A to F as shown in Fig. 2.1c.

Vegetation types from the terrestrial biosphere model SiBCASA show that there are four major biomes in Africa (see Fig. 2.1e). Consistent with this change in vegetation $\mathrm{CO_2}$ concentration shows a fluctuation in response to the seasonal vegetation dynamics and associated climatic conditions of the region. Amplitudes of the seasonal precipitation anomalies also vary across biomes (see Fig. 2.1d).

The wet/dry season anomalies about mean values during wet and dry months. Wet and dry months of the region are identified by applying a simple precipitation anomaly (SPA) on multiyear precipitation data from GPCC as:

$$SPA_i = (x_i - \bar{x})/\sigma \tag{2.1}$$

where the $\bar{x}$ is mean precipitation and x_i is precipitation at the i^{th} month and σ is the standard deviation. Then, months with a SPA_i less than -0.6 were considered as dry months while months with SPA_i above 0.7 are considered as wet months (Maheras, Xoplaki, and Kutiel, 1999). The analysis of multi-year GPCC precipitation data shows that December to April are wet months over broadleaf evergreen, C3 grass, Shrub southern, and C4 grass Southern while March - September are the dry months. On the other hand Shrub, North and C4 North have wet months from July to September while dry months are from December to March (see Fig. 2.1d).

2.2 Data Sets

2.2.1 Carbon Tracker Model and Data

Carbon Tracker is an annually updated analysis of atmospheric carbon dioxide distributions and their surface fluxes (Peters et al., 2007). Carbon Tracker is a data assimilation system that combines observed atmospheric CO_2 concentrations from about 81 ground-based sites across the globe with the model and forecasts what atmospheric CO_2 concentrations would be based on a preliminary set of assumptions about the sources and sinks of carbon dioxide. Carbon Tracker compares the model predictions with observations and then systematically adjusts and evaluates the preliminary assumptions until it finds the best combination that matches with the real-world data. It uses modules for atmospheric transport of $\mathrm{CO_2}$ via weather systems, for air-sea exchange, photosynthesis and respiration, fires, and fossil fuel combustion. Transport of atmospheric CO_2 is simulated by using the global two-way nested transport model (TM5). TM5 is an offline atmospheric tracer transport model (Krol et al., 2005) driven by meteorology from the ECMWF operational forecast model and from the ERA-Interim reanalysis (Dee et al., 2011) to propagate surface emissions. TM5 is based on a global $3^0 \times 2^0$ and at $1^0 \times 1^0$ spatial grid over North America.

The data from CT (version:CT2015) (`http://carbontracker.noaa.gov`; Peters et al. (2007)) were used to systematically extend aircraft profiles into the stratosphere and top of the atmosphere (Inoue et al., 2013; Frankenberg et al., 2016) and to quantify co-location error (Kulawik et al., 2016). The older data versions have been used and compared with different data sets over other parts of the globe in previous studies (Peters et al., 2007; Nayak et al., 2014; Kulawik et al., 2016; Krishnapriya et al., 2017). Most of the studies confirm that CT XCO_2 captures the observations reasonably well. In this study, we use Carbon Tracker release version CT2016, hereafter (CT2016) and near-real-time version (CT-NRT.v2017). Both versions of NOAA CT provide 3 hourly $\mathrm{CO_2}$ mole-fractions data for the global atmosphere at 25 pressure levels in a $3^0 \times 2^0$ spatial resolution for a period covering 2000 to 2016. The data can be accessed freely in the public domain (`ftp://aftp.cmdl.noaa.gov/products/carbontracker`).

The National Oceanic and Atmospheric Administration Earth System Research Laboratory (ESRL) Carbon Tracker provides a globally optimized $\mathrm{CO_2}$ flux at a spatial resolution of 1^0X1^0. Monthly product of $\mathrm{CO_2}$ flux from CT2017 output was extracted for tropical Africa covering the period from January 2000 to December 2016. The natural components of $\mathrm{CO_2}$ flux (i.e., $\mathrm{CO_2}$ flux due to biosphere exchange, forest fire, and Ocean-atmosphere interaction) are also extracted (hereafter referred to as CT2017-flux) and used in this study.

2.2.2 GOSAT measurements

GOSAT is the world's first spacecraft fully dedicated to measuring the concentrations of carbon dioxide and methane, the two major greenhouse gases, from space. It was launched successfully on January 23, 2009, and has been operating properly since then. GOSAT records reflected sunlight using three near-infrared band sensors. The field of view at nadir allows a circular footprint of about 10.5 km diameter (Kuze et al., 2009; Yokota et al., 2009; Crisp et al., 2012). GOSAT consists of two instruments. The sensors for the two instruments can be broadly labelled as thermal, near-infrared, and imager. The first two sensors are used as part of Fourier Transform Spectrometer for carbon monitoring which is referred to as TANSO-FTS, while the imager for cloud and aerosol observations is referred to as TANSO-CAI. The details on the spectral coverage, resolution, field of view, and different products of TANSO-FTS in the three SWIR bands can be found in a number of previous studies (Kuze et al., 2009; Saitoh et al., 2009; Yokota et al., 2009; Yokota et al., 2011; Crisp et al., 2012; Nayak et al., 2014; Deng et al., 2016a, and references therein). In this study, ACOS B3.5 Lite XCO_2 from GOSAT Level 2 (L2) retrieval based on the SWIR spectra of FTS observations and made available by Atmospheric CO_2 Observations from Space (ACOS) of NASA is used. ACOS B3.5 Lite XCO_2 has lower bias and better consistency than NIES GOSAT SWIR L2 CO_2 globally (Deng et al., 2016a). However, this version of ACOS XCO_2 is found to suffer systematic retrieval errors over the dark surfaces of high latitude lands and African savanna (Chevallier, 2015). Chevallier (2015) shows systematic errors in the African savanna associated with underestimating the intensity of fire during March at the end of the savanna burning season. Therefore, our choice of the ACOS B3.5 Lite, hereafter (GOSAT) XCO_2 is motivated by these differences.

2.2.3 OCO-2 measurements

OCO-2, the world's second full-time dedicated CO_2 measurement satellite. It was successfully launched by the National Aeronautics and Space Administration (NASA) on 2 July 2014. OCO-2 measures atmospheric carbon dioxide with the accuracy, resolution, and coverage required to detect CO_2 sources and sinks on a global and regional scale. OCO-2 has three-band spectrometer, which measures reflected sunlight in three separate bands. The O_2 A-band measures the molecular absorption of oxygen from reflected sunlight near 0.76 μm, while the CO_2 bands are located near 1.61 μm and 2.06 μm (Liang et al., 2017). In this study, OCO-2 XCO_2 V7 lite level 2 covering the period from January 2015 to December 2016, hereafter referred to as OCO-2 XCO_2, are used. Due to the scarcity of data, CT values from the two releases CT2016 for the year 2015 and CT-NRT.v2017 for the year 2016, hereafter (CT16NRT17) are employed in this study. The OCO-2 project team at Jet Propulsion Laboratory, California Institute of Technology, produced the OCO-2 XCO_2 data used in this study. The data can be accessed from NASA Goddard Earth Science Data and Information Service Center.

2.2.4 GOME-2 SIF

The Global Ozone Monitoring Experiment-2 (Munro et al., 2006) senses the Earth's backscattered radiance and extraterrestrial solar irradiance. It is a nadir-scanning medium-resolution ($\sim$0.5 nm) spectrometer that operates between 240 and 790 nm in four detector channels. Currently, there are three GOME-2 instruments operating onboard EUMETSAT's polar-orbiting Meteorological Operational Satellites (MetOp-A, -B and -C) launched on respectively 19 October 2006, 17 September 2012 and 7 November 2018. These sun-synchronous polar orbit satellites fly at an altitude of approximately 820 km and have an equator crossing (descending node) around 09:30 equator crossing local time. The wide spectral range allows GOME-2 to measure a large number of atmospheric trace constituents, with the emphasis on global ozone distributions. The fourth channel in the near-infrared (593 -790 nm) encompasses the SIF wavelength region. The channel has a spectral sampling of approximately 0.2 nm and a spectral resolution of 0.5 nm with a signal-to-noise ratio up to 2000 (Callies et al., 2000). The large GOME-2 default swath width of 1920 km with a footprint size of 80 x 40 km^2 enables a global coverage within 1.5 days.

Based on the statistical approach developed by Joiner et al. (2013) (see Sec. 1.5.1), the retrieval code developed at KNMI/WUR (Sanders et al., 2016; Schaik et al., 2020) uses a much larger dataset to construct the reference atmospheric spectra used to distinguish the small SIF signals from the complex structure of transmittance and reflectance from other atmospheric constitutes such as water vapour. Based on the improved algorithm, KNMI estimates the global SIF from GOME-2A covering the period from 2007 to 2020.

To study the African biosphere, we use Level 3 GOME-2 instrument Sun-Induced Fluorescence of Terrestrial Ecosystems Retrieval SIF (v2.0) at 735 nm monthly data at a spatial resolution of 0.5° ×0.5° covering the period from 2007 to 2016. For fair comparability of the SIF with vegetation indices, we normalized SIF by the cosine of the solar zenith angle. Note that we did not use the popular NASA GOME-2 SIF retrieval (Joiner et al., 2013; Joiner et al., 2016), but we used the KNMI/WUR SIF retrieval, which is particularly suited for tropical conditions (Koren et al., 2018). TROPOMI SIF is a promising alternative for future studies of the African carbon cycle. TROPOMI SIF has a higher spatial resolution than GOME-2 SIF and a more frequent coverage. Global TROPOMI SIF data was first shown by Köhler et al. (2018). Their study also included a detailed view of the North-African Nile Delta. In addition, Doughty et al. (2019) used TROPOMI to study the seasonality of the Amazon, showing the capability of this instrument to capture the seasonal dynamics of tropical ecosystems.

TABLE 2.1: Some basic information on the satellites used for the study. *After July 2013, the GOME-2(a) swath is half the size, pixels are 40x40 km^2 and repeat cycle is increased to 3 days.

	GOME-2	**OCO-2**	**GOSAT**
Temporal coverage	01/2007 to present	09/2014 to present	04/2009 to present
Spatial resolution	40 x 80 km^2*	1.3 x 2 km^2	10 km diameter
Equator crossing time	~9:30 hrs	~13:36 hrs	~13:00 hrs
Repeat cycle	1.5 days*	16 days	3 days
Spatial resolution for global monthly mapping	0.5° x 0.5°	1° x 1°	2° x 2°

2.2.5 Flask observations

Measurements of CO_2 from nine ground-based flask observations near and within Africa landmass (see Fig. 2.1a, for their distribution) were accessed from the NOAA/ESRL/GMD CCGG cooperative air sampling network (`https://www.esrl.noaa.gov/gmd/ccgg/flask.php`). Sites description is given in Table 2.2.

TABLE 2.2: Information on flask observation sites near and within Africa land mass. * indicates discontinued site or project.

Code	**Name**	**Country**	**Latitude (^0N)**	**Longitude (^0E)**	**Altitude (masl)**	**Air pressure at T = 25^0C (Pa)**
ASC	Ascension Island	Ascension Island	-7.97	-14.40	85.00	100342.02
ASK	Assekrem	Algeria	23.26	5.63	2710.00	73571.64
CPT	Cape Point	South Africa	-34.35	18.49	230.00	98682.99
IZO	Izana, Canary Islands	Spain	28.31	-16.50	2372.90	76650.84
LMP	Lampedusa	Italy	35.52	12.62	45.00	100803.63
MKN*	Mt. Kenya	Kenya	-0.062	37.30	36.00	65579.92
NMB	Gobabeb	Namibia	-23.58	15.03	456.00	96141.54
SEY	Mahe Island	Seychelles	-4.69	55.53	2.00	101301.78
WIS	Weizmann, Ketura	Israel	29.97	35.06	151.00	99584.09

2.2.6 Eddy covariance flux data

A collection of eddy covariance flux data from six regions in Africa (see Fig. 2.1e for their distribution) was used in this study to assess the correlation of SIF-GPP and NIRv-GPP at an ecosystem level. Specifically, available monthly GPP products from daytime partitioning (see Sec. 1.5.2) of fluxes (GPP_DT_VUT_REF) from FLUXNET 2015 were compared to SIF-GPP and NIRv-GPP averaged in 4^0X4^0 window centring the flux-tower. The daytime data-based estimate uses an approach described in detail in Lasslop et al. (2010). It is based on a light response curve extended to account for the temperature sensitivity of respiration by including the Lloyd and Taylor model (Lloyd and Taylor, 1994) and a drought limitation of GPP. Sites description is given in Table 2.3.

TABLE 2.3: Information on flux-tower sites in Africa.

Site_ID	**Site_Name**	**Country**	**Latitude (°N)**	**Longitude (°E)**	**Start_date**	**End_date**
CG-Tch	Tchizalamou	Congo	-4.29	11.66	01/2006	12/2009
GH-Ank	Ankasa	Ghana	5.27	-2.69	01/2011	12/2014
SD-Dem	Demokeya	Sudan	13.28	30.48	01/2005	12/2009
SN-Dhr	Dahra	Senegal	15.40	-15.43	01/2010	12/2013
ZA-Kru	Skukuza	Zambia	-25.02	31.50	01/2000	12/2013
ZM-Mon	Mongu	Zimbabwe	-15.44	23.25	01/2009	12/2009

2.2.7 MPI-BGC GPP

Monthly global ecosystem estimation of terrestrial GPP was made available by the Max Planck Institute's Biogeochemistry integration group (Jung et al., 2011). Which is constructed using a machine learning method to upscale information from flux-towers up to a $0.5^0X0.5^0$ grid, aided by gridded meteorological and remote sensing co-variables covering the period from 2007 to 2010 was used. We also use the multiyear monthly mean of GPP at a spatial resolution of $0.5^0X0.5^0$ data described by Beer et al. (2010) (accessed from: `https://www.bgc-jena.mpg.de/geodb/projects/Data.php`). This product will henceforth be referred to as MPI-BGC GPP.

2.2.8 Satellite-based vegetation indices from MODIS

MODerate Resolution Imaging Spectroradiometer (MODIS) is an imaging spectrometer on NASA's Terra and Aqua satellites. The Terra satellite was launched in 2000 and has an equator crossing local time of 10:30 hrs the second satellite called Aqua was launched two years later from Terra in 2002 with equator crossing of 12:00 hrs, both are in sun-synchronous orbits with 16 orbits per day. Enhanced Vegetation Index (EVI) and the Normalized Difference Vegetation Index (NDVI) are the two most widely used vegetation indices for monitoring vegetation conditions and have significant relationships with GPP (Xiao et al., 2005). Monthly EVI and NDVI from MODIS collection of MOD13C2 at a spatial resolution of $0.05^\circ \times 0.05^\circ$ in the years 2007-2016 was used in the study. Compared with NDVI, EVI is less sensitive to soil background variations and remains sensitive over dense vegetation (Huete et al., 2002). For that reason, we focus on comparison with the EVI than with NDVI.

The NIRv represents the fraction of reflected Near-Infrared Reflectance (NIR) of light that originates from vegetation. NIRv was first described as a proxy for photosynthesis by Badgley, Field, and Berry (2017). More accurate retrievals of the contribution of vegetation to observed NIR reflectance under a wide array of field conditions, including over sparse canopies and regardless of soil brightness, recent studies use NIRv for vegetation productivity and computing a NIRv-based meddled SIF at 760 nm (Badgley, Field, and Berry, 2017; Zeng et al., 2019). In this study we used NIRv at a spatial resolution of $0.5^\circ \times 0.5^\circ$ and a monthly temporal resolution for the years 2007-2016. We also used NIRv at a higher resolution ($0.05^\circ \times 0.05^\circ$, daily) in a comparison with flux tower GPP. MODIS data over a 16-day period from Terra and Aqua can be combined to build a high resolution (500 m) composite called MCD43A4. NIRv data used here were calculated using surface reflectance data from MODIS collection MCD43C4 v006 (Schaaf and Wang, 2015) covering the period from 2007 to 2016 as:

$$NIRv = \rho_{nir} \times \left(\frac{\rho_{nir} - \rho_{red}}{\rho_{nir} + \rho_{red}} - 0.08 \right) \tag{2.2}$$

where ρ_{nir}, ρ_{red} are reflectances acquired in the near-infrared (841 - 876 nm) and red (620 - 670 nm) portions of the electromagnetic spectrum respectively (Huete et al., 2002). A constant 0.08 is subtracted to reduce the effects of the bare soil (Baldocchi et al., 2001; Huang, Xiao, and Ma, 2019). Uncertainties in NIRv are largely due to inaccuracy in measurements of canopy architecture, including the clamping index and leaf projection function and the clumping index, both strongly vary in time and space (Zeng et al., 2019).

2.2.9 Other datasets

Global Precipitation Climatology Centre (GPCC) provides global rainfall data which can be freely accessed from `http://gpcc.dwd.de` data portal. GPCC provides gridded high-resolution and high-quality land surface precipitation analyses as mandated by the World Meteorological organization's (WMO's), World Climate Research Program and the Global Climate Observing System (GCOS). GPCC provides gauge-based gridded monthly precipitation datasets for the global land surface, in different spatial resolutions. For this study, we chose a $1^0 X 1^0$ spatial resolution over tropical Africa covering the period from January 2000 to December 2016. Data products are publicly available in OGC compliant netCDF format to the community (`ftp://ftp-anon.dwd.de/pub/data/gpcc/html`). Monthly precipitation data from GPCC at 0.5^0 spatial resolution was employed. This analysis product is based on stations data.

Monthly mean of daily means of 2m air temperature at a spatial resolution of 0.75^0 on a regular longitude/latitude grid, corresponding to about 83 km at the equator were extracted over the study region. Temperature data was obtained from ECMWF atmospheric reanalysis ERA-Interim (Dee et al., 2011)

Monthly mean data sets of root Zone Soil moisture and downward shortwave radiation from the Global Land Data Assimilation System Version 2.1 (GLDAS2.1) of National Aeronautics and Space Administration (NASA) Goddard Space Flight Center (GSFC) a spatial resolution of $0.25° \times 0.25°$ covering the period from years February 2000 to December 2016 was used (Peters-Lidard et al., 2007).

Based on the SST anomalies averaged over a certain region in the tropical Pacific Ocean, there are five common Niño indices namely NINO 1, 2, 3, 3.4 and 4. Niño 3.4 composite effect of Niño 3 and Niño 4 became preferable for defining El Niño and La Niña events. Niño 3.4 is defined by SST anomalies over the region that covers $5^0 N - 5^0 S$, $170^0 W - 120^0 W$ and is considered as representing the average equatorial SSTs across the Pacific from about the dateline to the South American coast. The Niño 3.4 index typically uses a 5-month running mean, and El Niño or La Niño events are defined when the Niño 3.4 SSTs exceed +/- $0.4^0 C$ for a period of six months or more. The latest Niño 3.4 index accessed from the new HADISST dataset, from the Hadley Centre was used in this study.

2.3 Basic statistics

Correlation coefficients (R), bias and root mean square deviation (RMSD) are used to assess the level of agreement between the two data sets. The mean bias determines the average deviations in XCO_2 between Carbon Tracker simulation and satellite observations. In this work the bias at the j^{th} grid point is computed as:

$$Bias_j = \frac{1}{n}\sum_{i=1}^{n}(S_i - O_i) \tag{2.3}$$

where S_i and O_i are CT and GOSAT XCO_2 values over the j^{th} pixel at the i^{th} time respectively. To quantify the extent to which XCO_2 of CT and GOSAT agree, the pattern correlations at the j^{th} grid point are computed as:

$$R_j = \frac{\frac{1}{n}\sum_{i=1}^{n}(S_i - \bar{S})(O_i - \bar{O})}{\sqrt{\frac{1}{n}\sum_{i=1}^{n}(S_i - \bar{S})^2}\sqrt{\frac{1}{n}\sum_{i=1}^{n}(O_i - \bar{O})^2}} \tag{2.4}$$

where $\bar{S}$ and $\bar{O}$ are the mean values of S_i and O_i over the j^{th} pixel. The root mean square deviation (RMSD) which shows the standard error of the model with respect the observation at the j^{th} grid point is computed as :

$$RMSD_j = \sqrt{\frac{1}{n}\sum_{i=1}^{n}((S_i - \bar{S}) - (O_i - \bar{O}))^2} \tag{2.5}$$

this is the centered pattern root mean squared (RMS) difference which is obtained from the RMS error after the difference in the mean has removed (Taylor, 2001).

Chapter 3

On the performance of satellite-based observations of CO_2 in capturing the NOAA Carbon Tracker model and ground-based flask observations over Africa land mass

3.1 Background

Models with appropriate physical and mathematical formulations and sufficiently constrained by observations can be used to understand the spatio-temporal nature of atmospheric CO_2. The NOAA Carbon Tracker (CT) is an integrated modelling system that assimilates CO_2 from other observations to complement satellite observations in understanding CO_2 surface sources and sinks as well as its spatiotemporal variability. However, both satellite and model data should be validated against other independent satellite observations and/or in-situ observations before using them to answer scientific questions. As a result, a lot of validation and intercomparison has been conducted in previous studies. For example, Kulawik et al. (2016) found a root mean square deviation of 1.7 and 0.9 ppm in GOSAT and CT2013b XCO_2 relative to 17 TCCON sites across the globe respectively. Other authors have undertaken validation exercises and found the bias of $-8.85 \pm 4.75\ ppm$ in retrieving XCO_2 from the GOSAT observed spectrum by Japans National Institute for Environmental Studies (NIES) level 2 V02.xx XCO_2 (Yoshida et al., 2013) with respect to TCCON (Morino et al., 2010). In addition, Chevallier (2015) shows the retrieved XCO_2 from GOSAT observed spectrum by NASA Atmospheric CO_2 Observations from Space (ACOS) (O'Dell et al., 2012) suffers a systematic error over African Savanna. Lei et al. (2014) also showed a regional difference of XCO_2 between the ACOS and NIES datasets. For example, a larger regional difference from 0.6 to 5.6 ppm was obtained over China land region, while it is from 1.6 to 3.7 ppm over the global land region and from 1.4 to 2.7 ppm over US land region. These findings suggest that it is important to assess the consistency of $\mathrm{XCO_2}$ from satellite observations with respect to state-of-the-art models (e.g., NOAA Carbon Tracker) and ground-based observations over other regions as well.

Therefore, this chapter aims to assess the performance of the observed XCO_2 from GOSAT and OCO-2 satellites in capturing simulated XCO_2 from NOAA Carbon Tracker model over Africa. These satellite observations and Carbon Tracker mixing ratios near the surface are also compared to available in situ $\mathrm{CO_2}$ flask data from Assekrem, Algeria; Mt. Kenya; Gobabeb, Namibia; and Cape Town; as well as to data off the coast of Seychelles, Ascension Island, and at Izana, Tenerife. Moreover, the consistency between the model and satellite observations in capturing the amplitudes and phases of observed seasonal cycles over different parts of the continent are evaluated. The agreement of modelled spatiotemporal variability with the known seasonal climatology of the regions that determines carbon source and sink levels, is also assessed.

3.2 Analysis methods

The GOSAT and CT model XCO_2 time series used in this investigation span five years, ranging from May 2009 to April 2014. Atmospheric $\mathrm{CO_2}$ concentrations of NOAA Carbon-Tracker have global coverage with a $3^0 \times 2^0$ Longitude/Latitude resolution, which covers 426 grid boxes in our study area. Satellite observations, however, are different from model assimilation and have gaps because of various reasons (e.g., clouds and the observational mode of the satellite). As a result, there is no one to one spatiotemporal match between the two data sets. For example, CO_2 products from the two datasets are not directly comparable since CT is a 3 hourly smooth and regular grid dataset, whereas GOSAT XCO_2 is irregularly distributed in space and time. Thus, the CT CO_2 is extracted on the time and location of GOSAT-XCO_2 data. Using the grid point of CT as a reference bin, the corresponding GOSAT XCO_2 found within a rectangle of $1.5^0 \times 1.5^0$ with center at the reference bin and with a temporal mismatch of a maximum of 3 hrs is extracted. Moreover, CT has higher vertical resolutions than GOSAT. As a result, the two cannot be directly compared. It is customary to smooth the high-resolution data (in this case CT) with averaging kernels and a priori profiles of the low-resolution satellite measurements (in this case GOSAT). In addition, due to the difference between CT and GOSAT on the number of vertical levels, CT CO_2 is interpolated to the vertical levels of GOSAT. The CT XCO_2 (XCO_2^{model}) used in the comparison is computed from the interpolated CT CO_2 (CO_2^{interp}), pressure weighting function (w), XCO_2 a priori (XCO_{2a}), column averaging kernel of the satellite retrievals (A) and a priori profile (CO_{2a}) of the retrievals as per procedure discussed by Rodgers and Connor (2003), Connor et al. (2008), O'Dell et al. (2012), Chevallier (2015), and Jing et al. (2018) and given as:

$$XCO_2^{model} = XCO_{2a} + \sum_i w_i^T A_i * (CO_2^{interp} - CO_{2a})_i \tag{3.1}$$

where i is the index of the satellite retrievals vertical level and T is the matrix transpose. To compare the CT simulations and the satellite observation with the flask observations, the vertical profiles of the satellite and CT were extracted at the corresponding pressure level and location within a box of 1.5^0.

Comparisons with in-situ flask observations are achieved in a way that the Carbon Tracker and satellite observations are taken at a corresponding pressure level of the in-situ flask observation (as mentioned in Table 2.2) to correspond to the flux tower surface observation. Furthermore, the datasets are resampled to fit the flask observations in a 3^0X3^0 window centring the flux towers and the available months were averaged.

3.3 Validation of CT XCO_2

3.3.1 Comparison of XCO_2 mean climatology from NOAA CT2016 and GOSAT

The XCO_2 obtained from the NOAA Carbon Tracker model and GOSAT observation was compared. The results are based on 426 grid boxes uniformly distributed to cover the whole of Africa's land region. The analysis was based on five years of daily data starting from May 2009 to April 2014.

Fig. 3.1 shows temporal average of CT2016 (Fig. 3.1a) and GOSAT (Fig. 3.1b) XCO_2 distribution. The major common spatial feature in the mean map of XCO_2 from GOSAT and CT2016 reanalysis shows a dipole structure characterized by high XCO_2 northward of the equator and low XCO_2 southward of equator with the exception of some part of Equatorial Guinea and Republic of

Congo for CT (Fig. 3.1a) and part of Democratic Republic of Congo for GOSAT (Fig. 3.1b); these are characterized by spatially anomalous high XCO_2. The Southern Africa region is characterized by weak anthropogenic CO_2 emission and high CO_2 uptake by the vegetation than Northern Africa (Ciais et al., 2011). This contributed to the observed dipole distribution. Another important pattern is an anomalous peak over the annual average location of the Inter-tropical convergence zone (ITCZ) (Fig. 3.1b), which appears to fade over Eastern Africa. This is in agreement with the fact that carbon stocks and net primary production per unit land area is high over Equatorial Africa and decreases towards northward and southward of the equator over arid environments (Williams et al., 2007). However, Fig. 3.1b shows that GOSAT observations have some limitations in simulating this spatial pattern in comparison to CT.

Fig. 3.1c shows the mean difference (CT2016-GOSAT) XCO_2 which ranges from -4 to 2 ppm. The highest difference between the CT2016 and GOSAT XCO_2 (as high as -4 ppm) is observed over Northern part of Equatorial Africa (e.g., southern Guinea, southern Ghana, southern Nigeria, southeast of Central Africa, western Ethiopia and South Sudan.) which are also known for near-year-round rainfall and relatively dense vegetation. The regions are known for their rain forest (Malhi et al., 2013). The likely explanation could be XCO_2 mean (over five years) may be slightly positively biased due to fewer GOSAT observations as shown in Fig.3.1d. The satellite retrievals have a noise which can be smoothed out when a large number of datasets are averaged. The strategy and methods for cloud screening in GOSAT retrievals could lead to a smaller number of observations in the equatorial region (Crisp et al., 2012; O'Dell et al., 2012; Yoshida et al., 2013; Chevallier, 2015; Deng et al., 2016b). The number of datasets used for comparison ranged from 14 to 4288 from gridbox to gridbox with a spatial mean of 1109 data over the continent. Fig. 3.1c also shows that CT2016 simulations are overall lower than the values of GOSAT observations over most regions with an exception in Gabon, Congo, southern Kenya, and southern Tanzania where CT2016 simulations are higher than GOSAT observations by more than 1 ppm. The spatial distribution of global atmospheric CO_2 is not uniform because of the irregularly distributed sources of CO_2 emissions, such as large power plants and forest fire, and biospheric assimilation as clearly noted above.

Fig. 3.2a shows the differences between CT2016 and GOSAT XCO_2, which ranges from -4 to 3 ppm. Out of 100% occurrence, more than 90% of the observed differences are within ± 2 ppm. The mean difference between CT2016 and GOSAT means is about -0.27 ppm with the standard deviation of 0.98 ppm

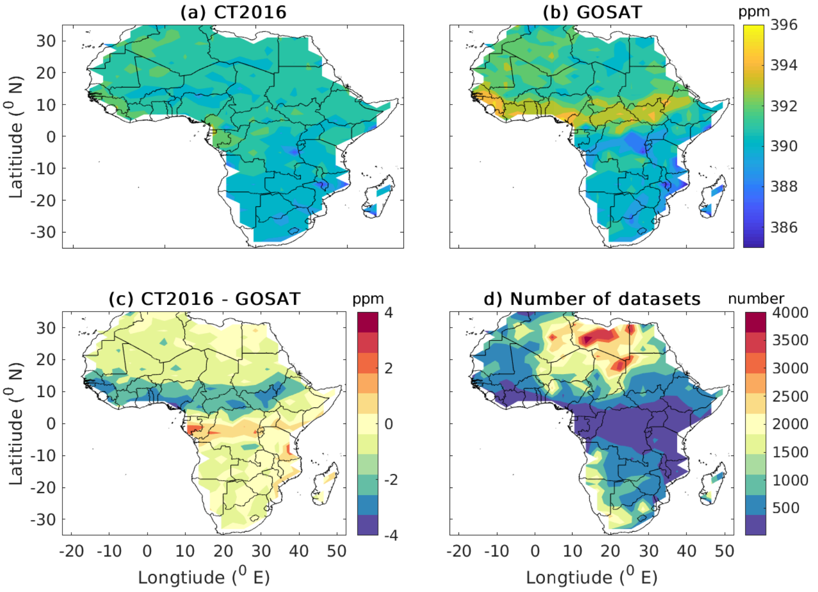

FIGURE 3.1: Distribution of five-years averages of CT2016 **(a)** and GOSAT **(b)** XCO_2 and their difference **(c)** gridded in $3^0 \times 2^0$ bins over Africa's Land mass; and the total number of datasets at each grid from the GOSAT observations(d).

indicating better regional consistency and low potential outliers. Moreover, a negative mean of the difference implies that XCO_2 simulated from CT2016 is lower than that of GOSAT retrievals over Africa landmass.

Because of the selection criteria which permits a difference of 3 degrees long and wide, the two datasets are not exactly at the same point. The impact of the relative distance between them should be assessed before performing any statistical comparison. Fig. 3.2b depicts colour-coded scatter plot of CT2016 model simulation verses GOSAT to determine if the discrepancy between the datasets arose from the spatial mismatch. The colour code indicates the relative distance between the model and observation datasets. For these datasets, the 50^{th} percentile has a relative distance of 1.19^0, which means 50% of the data has a relative distance of shorter than 1.19^0. The maximum relative distance between them is 2.12^0. However, there is no indication that this has been the case since the scatter is not a function of the relative distance between the datasets. For example, data points with blue colour with the lowest location difference are scattered everywhere instead of along the 1:1 line. Furthermore, we found the bias of -0.26 ppm, a correlation coefficient of 0.86 and RMSD of 2.19 ppm for datasets which has a relative distance shorter than 1.19^0. On the other hand, the bias, correlation coefficient, and RMSD are -0.33 ppm, 0.86 and 2.22 ppm for those which are above 1.19^0. These statistics confirm that there is no strong discrepancy due to our selection criteria.

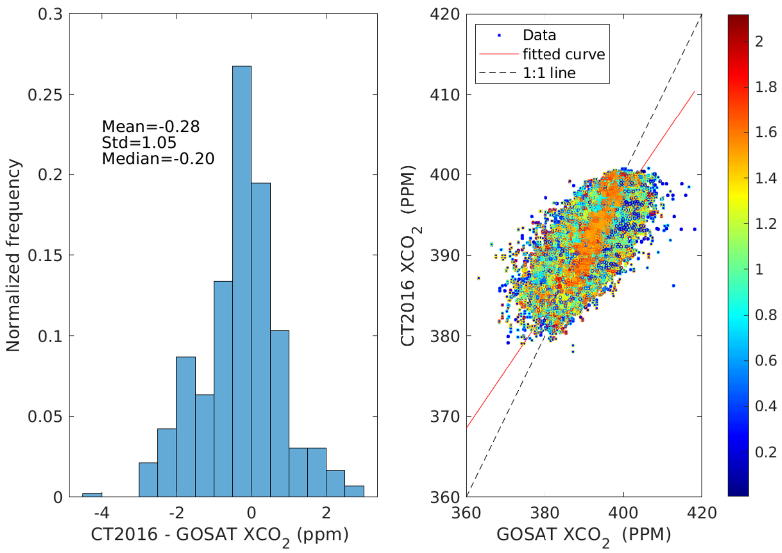

FIGURE 3.2: Histogram of the difference of CT2016 relative to GOSAT (left panel) and color code scatter diagram of XCO_2 concentration as derived from CT2016 and GOSAT (right panel). Color indicates the relative distance in unit of degrees as shown in colorbar between datasets.

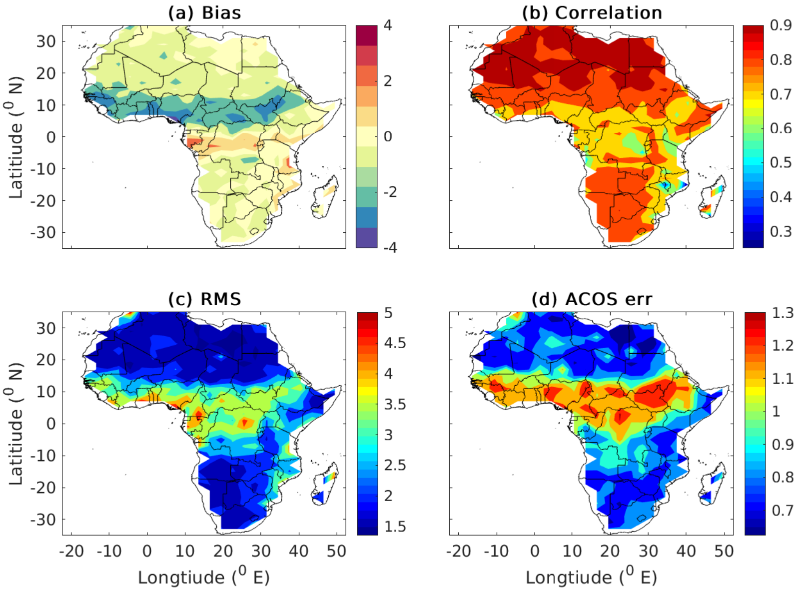

FIGURE 3.3: Spatial patterns of bias (a), correlation (b), RMSD (c) of the two data sets, and mean posteriori estimate of XCO_2 uncertainty from GOSAT (d).

Fig. 3.3 shows a statistical comparison of XCO_2 from CT2016 and GOSAT over Africa. The number of data used in this comparison is shown in Fig. 3.1d.

TABLE 3.1: Summary of statistical relation between CT2016 and GOSAT observation. The statistical tools shown are the mean correlation coefficient (R), the spatial average of bias (Bias), the spatial average root mean square deviation (RMSD), the standard deviation in bias (std of Bias), GOSAT posteriori estimate of XCO_2 error (GOSAT err), the standard deviation in CT2016 XCO_2 (CT2016 std) and the standard deviation in GOSAT XCO_2 (GOSAT std).

Statistical tool	R	Bias (ppm)	RMSD (ppm)	std of Bias (ppm)	GOSAT err (ppm)	CT2016 std (ppm)	GOSAT std(ppm)
Values	0.83	-0.28	2.30	1.05	0.91	0.90	1.55

As it is depicted in Fig. 3.3a, the bias ranges from -4 to 2 ppm with a mean bias of -0.28 ± 1.05 ppm (see Table 3.1). A larger negative bias of about -2 ppm was found along with the annual mean position of ITCZ, the main climatic mechanism controlling rainfall in Africa. Systematic errors due to ITCZ and the East African Monsoon need to be addressed well in satellite retrievals and modelling works. The correlation varies from 0.4 over some isolated pockets in Congo, Tanzania, Mozambique, Uganda, and western Ethiopia to 0.9 over the northern part of Africa above 13^0N, Eastern Ethiopia and the Kalahari Desert. Fig. 3.3b depicts the correlation coefficient between GOSAT and Carbon Tracker XCO_2. The region with poor correlation also exhibits high RMSD as shown in Fig. 3.3c. To understand whether this discrepancy originates from model weakness alone or terrible satellite visibility when the ITCZ is present and clouds are extremely thick and widely present, we have looked at the GOSAT posterior estimate of XCO_2 error (Fig. 3.3d), which are high over regions where the bias and RMSD between GOSAT and Carbon Tracker XCO_2 is high. GOSAT's posterior estimate of XCO_2 error is a combination of instrument noise, smoothing error and interference errors (Connor et al., 2008; O'Dell et al., 2012). This posterior estimate of XCO_2 error does not include forward model error which may lead to underestimation of the true error of satellite XCO_2 by a factor of two (O'Dell et al., 2012). Therefore, part of the discrepancy is linked to satellite retrievals uncertainty, which might have been amplified due to the small number of data points used to calculate the mean error of GOSAT XCO_2 measurements (see Fig. 3.1d). In general, the two data sets are characterized by a high spatial mean correlation of 0.83 ± 0.20, a global offset of -0.28 ± 1.05 ppm, which is the average bias, a regional precision of 2.30 ± 1.46 ppm, which is average RMSD and relative accuracy of 1.05 ppm which is the standard deviation in the bias as depicted in Table 3.1. The number of data used in the statistics is 472,792 over 425 pixels covering the study period, distribution at each grid point is shown in Fig. 3.1d. Negative bias indicates that CT2016 XCO_2 is lower than GOSAT XCO_2 values.

3.3.2 Comparison of monthly average time series of NOAA CT2016 and GOSAT XCO_2

Figs. 3.4 - 3.6 show monthly mean XCO_2 from CT2016 and GOSAT averaged over North Africa, Equatorial Africa, and Southern Africa respectively. Figs. 3.4a - 3.6a depict the existence of an overall very good agreement for the monthly averages with respect to the amplitude and phase of XCO_2. However, XCO_2 from the two datasets slightly disagree in capturing the seasonal cycles over Southern Africa.

TABLE 3.2: Summary of statistical relations between CT2016 and GOSAT observations. The statistical analysis were made using a monthly averaged time series of 60 months (i.e., months from May 2009 to April 2014).

Statistics	R	Bias (ppm)	RMSD (ppm)	number of data
Africa	0.997	-0.254	0.265	698505
North Africa	0.996	-0.361	0.345	424070
Equatorial Africa	0.977	-0.172	0.708	101660
Southern Africa	0.964	0.006	0.841	172775

Fig. 3.4a shows that XCO_2 concentration reaches a maximum in April and a minimum in September over North Africa. Consistent with this evidence, other authors (e.g., Zhou et al., 2008) have indicated the presence of strong absorption of CO_2 by vegetation during August in the northern hemisphere. This is the most likely cause for the minimum concentrations observed during September over North Africa. Both datasets show the concentration of XCO_2 increases from October to April, and decreases from May to September (see also Table 3.3). Moreover, the two dataset shows a monthly mean regional mean bias of -0.36 ppm with a correlation of 1.0 and a small root mean square deviation of 0.36 ppm (see Table 3.2).

Fig. 3.5a shows XCO_2 concentration reaches a maximum (392.99 ppm) for CT2016 in March and (393.53 ppm) for GOSAT in January while a minimum (389.56 ppm for CT2016 and 389.32 ppm for GOSAT) in October over Equatorial Africa. The largest monthly mean difference of -1.34 ppm and the smallest of -0.05 ppm between the two datasets observed in December and in April respectively (Table 3.3). Moreover, both datasets show that the concentration of CO_2 increases from October to March while it decreases from June to October. This similarity in the seasonal variability of the two datasets shows that they are in good agreement in terms of amplitude and phase. In addition, the two

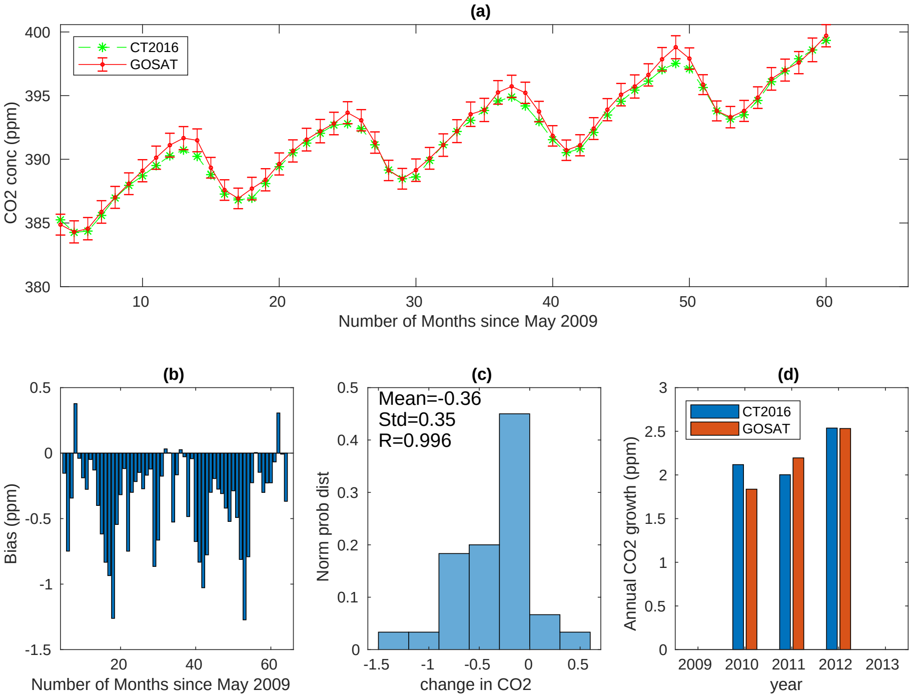

FIGURE 3.4: The monthly mean time series of CT2016 and GOSAT from May 2009 to April 2014 averaged over North Africa (a), bias associated with the monthly means (b), the histogram of difference in XCO_2 computed as CT2016-GOSAT XCO_2 in units of ppm (change in CO_2) (c) and the annual growth rate obtained by subtracting the mean from the mean of the next year (d). The error bars in (a) show the GOSAT a posteriori XCO_2 uncertainty.

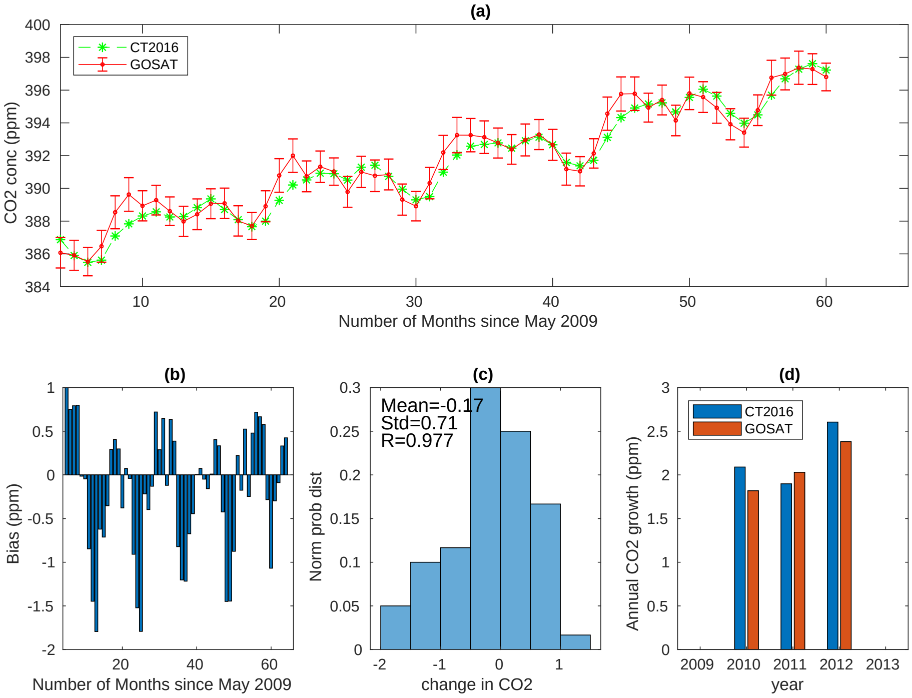

FIGURE 3.5: The same as Fig. 3.4 but over Equatorial Africa.

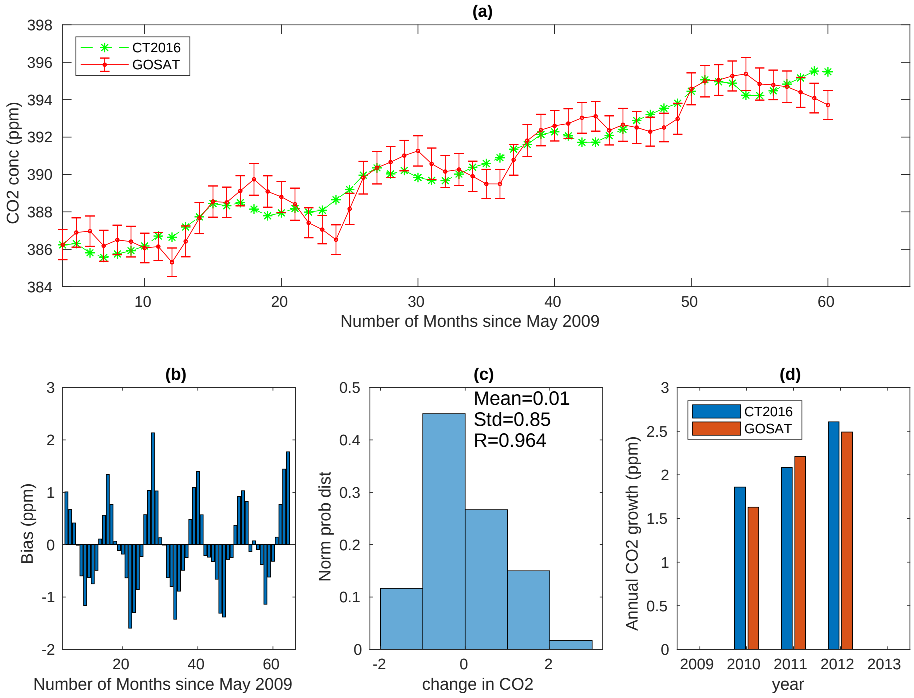

FIGURE 3.6: The same as Fig. 3.4 but over Southern Africa.

datasets show a monthly average regional average bias of -0.17 ppm, a correlation of 0.98 and a small root mean square deviation of 0.71 ppm over Equatorial Africa (see Table 3.2). Fig. 3.6a shows maximum XCO_2 concentration in April (391.04 ppm) for CT2016 and in October (391.28 ppm) for GOSAT, while minimum in May (389.30 ppm) for CT2016 and (388.46 ppm) for GOSAT over Southern Africa. The largest monthly mean difference of 1.53 ppm and 0.03 ppm between the two datasets is observed in April and in July (Table 3.3) respectively. Both datasets show the concentration of CO_2 increases from May to July while it decreases from October and November. However, the XCO_2 from CT2016 shows a gradually increasing trend from January to April. Conversely, GOSAT XCO_2 shows decreasing values. This is most likely the result of the fact that CT2016 simulation is more sensitive to the growing size of sinks following the rainy season. Moreover, the two datasets show a monthly mean regional mean bias of 0.07 ppm, a correlation of 0.97 and RMSD of 0.87 ppm over southern Africa (see Table 3.2).

Figs. 3.4b - 3.6b show the regional averaged bias in the monthly mean XCO_2 from CT2016 and GOSAT. Fig. 3.4b shows the presence of a seasonally varying negative bias over North Africa. A high (<-0.5 ppm) negative bias in the dry season (April to June) and low (>=-0.1 ppm) negative bias in the wet season (August to September) are observed. Moreover, the strength of bias increases from February to June. Conversely, the bias decreases from June to September.

TABLE 3.3: Five years monthly averaged XCO_2 concentration in ppm obtained from CT2016 (CT) and GOSAT (GO) and their difference $CT - GO$ (D) in ppm over Africa (A), North Africa (NA), Equatorial Africa(EA) and Southern Africa (SA).

Month	A CT	A GO	A D	NA CT	NA GO	NA D	EA CT	EA GO	EA D	SA CT	SA GO	SA D
January	391.81	392.17	-0.36	392.43	392.61	-0.18	392.22	393.53	-1.31	390.28	390.49	-0.21
February	392.48	392.58	-0.1	393.27	393.5	-0.23	392.72	393.21	-0.49	390.52	390.06	0.46
March	393.25	393.28	-0.03	394.02	394.29	-0.27	392.99	393.19	-0.2	390.82	389.81	1.01
April	393.81	393.91	-0.1	394.79	395.35	-0.56	392.87	392.92	-0.05	391.04	389.51	1.53
May	391.65	391.85	-0.21	392.92	393.73	-0.81	390.47	389.93	0.54	389.3	388.46	0.84
June	391.49	391.94	-0.45	392.43	393.33	-0.9	391.12	390.89	0.23	389.95	389.85	0.11
July	390.92	391.1	-0.18	391.09	391.5	-0.41	391.44	391.03	0.41	390.43	390.4	0.03
August	389.89	389.96	-0.07	389.4	389.44	-0.04	390.92	390.72	0.21	390.37	390.61	-0.25
September	389.26	389.4	-0.14	388.65	388.75	-0.1	390.02	389.67	0.35	390.39	391.01	-0.61
October	389.19	389.71	-0.51	388.85	389.26	-0.41	389.56	389.32	0.24	389.95	391.28	-1.32
November	389.97	390.43	-0.46	390.06	390.32	-0.26	389.86	390.52	-0.66	389.8	390.76	-0.96
December	391.09	391.53	-0.45	391.42	391.6	-0.18	391.23	392.57	-1.34	389.98	390.52	-0.54

Similarly, Figs. 3.5b and 3.6b show a seasonally fluctuating bias. For example, Fig. 3.6b shows a positive bias from February to July and a negative bias from August to December over Southern Africa.

Figs. 3.4c - 3.6c show the histogram of difference. The mean difference between CT2016 simulation and GOSAT observations of XCO_2 is -0.36 ppm with a standard deviation of 0.35 ppm over North Africa (see Fig. 3.4c); Fig. 3.5c presents a mean difference of -0.17 ppm with a standard deviation of 0.71 ppm over Equatorial Africa and Fig. 3.6c reveals a mean difference of 0.01 ppm and a standard deviation of 0.85 ppm which indicates that XCO_2 from CT2016 was slightly higher than that of GOSAT over Southern Africa on average. In addition, the low standard deviation of monthly mean difference over North Africa typically indicates good regional consistency between CT2016 and GOSAT. This is mainly because Northern Africa is dominated by the Sahara desert, which is a vegetation-free area, and the systematic bias due to the local atmosphere biosphere interaction is minimum. However, the spatial mean of monthly mean bias is slightly higher (-0.36 ppm) over North Africa than over Equatorial Africa (-0.17 ppm) and Southern Africa (0.01 ppm). This is possibly due to the presence of strong local emissions from Egypt, Algeria and Libya as well as due to long-range transport from the Northern Hemisphere as reported in other studies (Williams et al., 2007; Carré et al., 2010).

Figs. 3.4d - 3.6d display an annual growth rate of XCO_2 which ranges from 1.5 to 2.7 $ppm\ yr^{-1}$. Moreover, the two datasets are consistent in determining the annual growth rate. The results are found in good agreement with the observed variability in the global annual growth rate from surface measurements (http://www.esrl.noaa.gov/ gmd/ccgg/trends/global.html) which is 1.67, 2.39, 1.70, 2.40, 2.51 ppm yr^{-1} global during 2009 - 2013 respectively, and 1.89, 2.42, 1.86,2.63, 2.06 ppm yr^{-1} for Mauna Loa during 2009 - 2013 respectively, with error bars of 0.05 - 0.09 ppm yr^{-1} for global and 0.11 ppm yr^{-1} for Mauna Loa data sets(Kulawik et al., 2016). The growth rate may not be conclusive due to the short length of the datasets used. However, it reflects how the CT and GOSAT observations perform with respect to each other.

3.3.3 Comparison of seasonal climatology

The seasonal cycle has important implications for flux estimate (Keppel-Aleks et al., 2012). It is important to analyze whether there are seasonally dependent biases that are affecting the seasonal cycle and whether the data sets are capturing the same seasonal cycle. The four seasons considered here are December/January/February (DJF), March/April/May (MAM), June/July/August (JJA), and September/October/November (SON). DJF corresponds to northern winter/southern summer, MAM to northern spring/southern autumn, JJA to northern summer/southern winter, and SON to northern autumn/southern spring, respectively. Fig. 3.7 shows the seasonal distributions of CT2016 (left panels) and GOSAT (middle panels) XCO_2 and their difference (CT2016 - GOSAT, right panels). The distribution clearly shows that XCO_2 concentration is maximum during MAM and minimum during SON over North Africa. On the other hand, maxima are found during SON and minima during DJF over Southern Africa. These features are in good agreement with the rainfall climatology of the northern and southern hemispheres. Moreover, Table 3.4 shows seasonally varying biases. Seasonal biases affect the seasonal cycle and amplitudes, which are important for biospheric flux attribution (Lindqvist et al., 2015).

The right panels in Fig. 3.7 show that the seasonal mean difference (CT2016 - GOSAT) ranges from -4 to 6 ppm. Negative bias means CT2016 is lower than GOSAT. These statistics are on the basis of the spatial average of seasonal averages of bias, correlation, RMSD and standard deviations. A maximum difference of 6 ppm over the Gulf of Guinea and Congo during JJA. However, such maximum difference was also observed over Southern Africa during DJF. A minimum of -4 ppm over the annual mean ITCZ region was observed during DJF and MAM. Moreover, the difference is above 1 ppm over Southern Africa region during DJF and MAM (wet season of the region). This implies high spatial variability of the seasonal mean difference during different seasons (see also Table 3.4). It also suggests that the discrepancy between the CT2016 and GOSAT becomes significant when vegetation cover is weak during DJF and MAM (dry season) over North Africa.

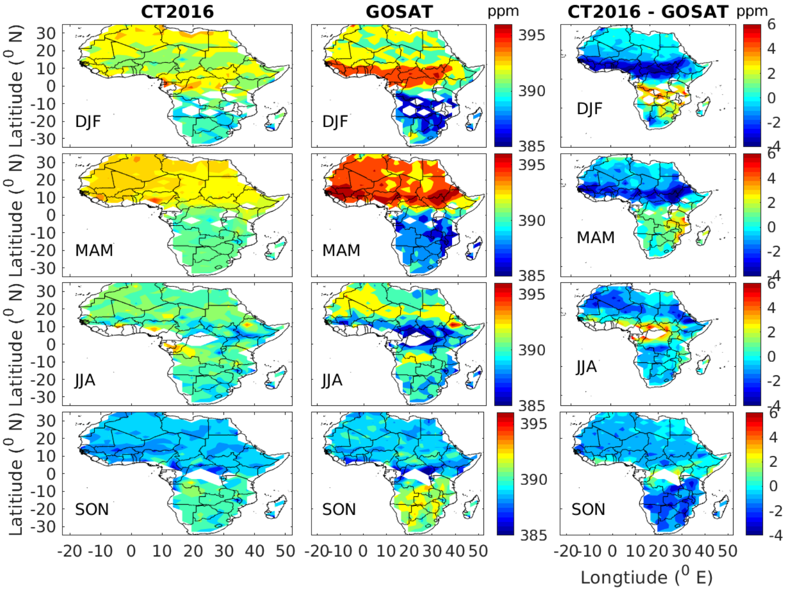

FIGURE 3.7: Seasonal climatology of XCO_2 for NOAA CT2016 (left panels) and GOSAT (midel panels) and their difference (right panels).

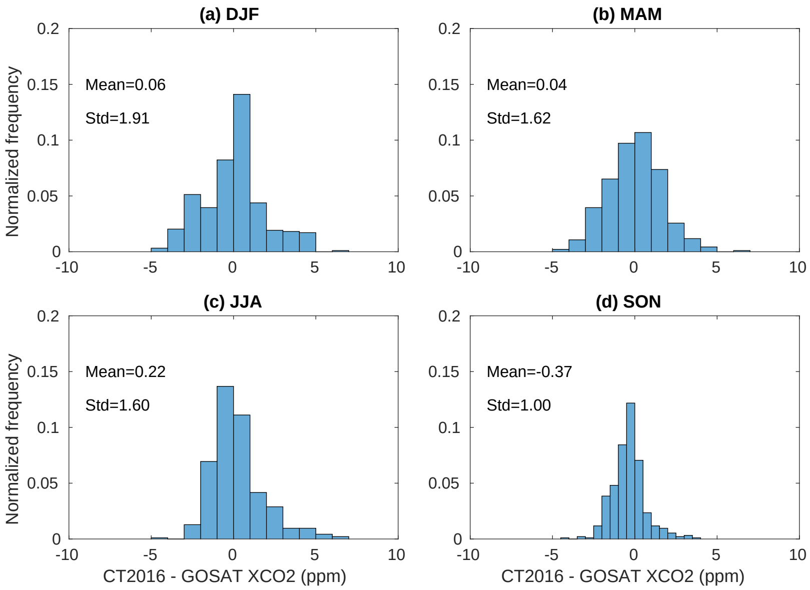

FIGURE 3.8: Histogram of difference for the seasonal XCO_2 climatology for DJF (a), MAM(b), JJA (c) and SON (d) seasons.

During SON, the seasonal difference in most Africa's landmasses ranged from -2 to 1 ppm. The result implies that CT2016 simulates nearly similar values of XCO_2 with that of GOSAT observation, indicating that there is a better spatial consistency during this season between these datasets. Furthermore, during these seasons, both Northern and Southern Africa have a moderate vegetation cover following their respective summer seasons. The two datasets show

TABLE 3.4: Summary of statistical relations between CT2016 and GOSAT XCO_2: Bias, correlation (R), Root mean square deviation (RMSD), standard deviation of XCO_2 from CT2016 simulation (CT2016 std), standard deviation of XCO_2 from GOSAT observation (GOSAT std), aggregate number of coincident observations (number of data) and number of grids over the region (grid).

Region	**Statistics**	**Bias (ppm)**	**R**	**RMSD (ppm)**	**CT2016 std (ppm)**	**std in GOSAT (ppm)**	**number of data**	**grid**
Africa	DJF	0.06	0.73	1.91	1.15	2.57	135865	409
	MAM	0.04	0.92	1.62	1.98	3.25	95942	410
	JJA	0.22	0.65	1.59	1.12	2.08	116360	400
	SON	-0.37	0.76	1	0.94	1.52	124233	408
N. Africa	DJF	-0.25	0.36	1.08	0.67	1.12	103913	204
	MAM	-0.72	0.44	1.11	0.62	1.24	65115	204
	JJA	-0.42	0.73	1.17	0.9	1.66	60854	204
	SON	-0.35	0.66	0.53	0.52	0.71	91778	204
Eq. Africa	DJF	-0.52	0.68	2.47	1.06	3.07	22639	121
	MAM	0.18	0.9	1.88	1.94	3.46	8300	115
	JJA	1.51	0.59	2.02	1.46	2.52	12714	104
	SON	0.25	0.7	1.3	1.16	1.83	10213	113
S. Africa	DJF	1.61	0.42	1.72	0.88	1.9	9313	84
	MAM	1.56	0.67	0.97	0.82	1.31	22527	91
	JJA	0.18	0.81	0.78	0.93	1.31	42792	92
	SON	-1.16	0.77	0.81	0.84	1.26	22242	91

lower regional variation (i.e., only from -2 to 2 ppm) over most of Africa landmass. However, Equatorial Africa exhibits a mean difference lower than -2 ppm during DJF and MAM. This indicates the model tends to simulate lower than GOSAT XCO_2 over the region. Fig. 3.7(right panels) reveals XCO_2 from CT2016 is lower than GOSAT XCO_2 over Northern Africa. The underestimation of observed XCO_2 by NOAA CT2016 model is likely related to the skill of driving ERA-Interim data as noted from previous studies. For example, Mengistu Tsidu (2012) has shown that the ERA-Interim data has a wet bias over Ethiopian highlands. Mengistu Tsidu, Blumenstock, and Hase (2015) have also shown that ERA-Interim precipitable water is higher than measurements from radio-sonde, FTIR and GPS observations. Therefore, such wet (precipitation occurrence) bias in the driving ERA-Interim GCM might have forced NOAA CT2016 to generate dense vegetation which serves as CO_2 sink.

Fig. 3.8 shows the mean difference between CT2016 and GOSAT XCO_2 seasonal means, which ranges from -0.37 to 0.04 ppm with a standard deviation within a range of 1.00 to 1.91 ppm over the continent. The highest mean difference of XCO_2 (-0.37 ppm) occurs during SON and the lowest (0.04 ppm) occurs during MAM. Table 3.4 presents the summary of statistical values for the spatial mean of each season means. The comparison between the two data sets also shows that there is a strong correlation (>0.5) during each season over the continent. However, there are moderate correlations (0.3 to 0.5) during DJF and MAM over North Africa and during DJF over Southern Africa. The low correlation over Northern Africa may be linked to a weak absorption by vegetation and a strong emission from human activities during winter as reported elsewhere (Liu et al., 2009; Kong et al., 2010). Moreover, Table 3.4 shows that the seasonal biases are negative over North Africa while they are mostly positive over Equatorial and Southern Africa. Negative biases are observed during DJF and SON over Equatorial and Southern Africa respectively implying that XCO_2 from CT2016 are lower than GOSAT during the dry seasons.

3.3.4 Comparison of GOSAT and CT2016 with flask observations

Comparisons of GOSAT and CT2016 with flask observations are carried out over six available ground-based flask observations. For comparison, the volume mixing ratios of CO_2 from GOSAT and CT2016 at the pressure level that corresponds to surface flask observations (see Table 2.3) were considered. We compare the near-surface values CO_2 from the Carbon Tracker CO_2 profile to the available in-situ CO_2 data from flask observations and XCO_2 of GOSAT/OCO-2 were transformed to CO_2 profiles using the prior CO_2 vertical profile and then the near-surface values are sampled.

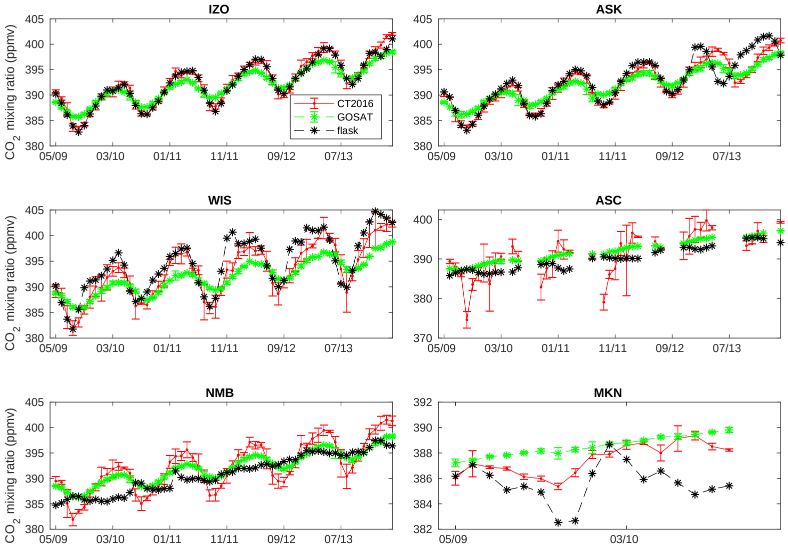

FIGURE 3.9: CO_2 time series for the coincident period for CT2016 (red), GOSAT (green) and flask (black). The standard deviation in computing the monthly mean is indicated by the vertical error bar.

Monthly mean CO_2 from flask observations at IZO and ASK in northern Africa shows an excellent agreement with both CT2016 and GOSAT CO_2. Moreover, CT2016 has better sensitivity in capturing the amplitudes than GOSAT, where observations from GOSAT mostly underestimate higher values of flask

CO_2 (Fig. 3.9). However, this agreement has deteriorated over sites in Equatorial Africa (ASC and MKN) and Southern Africa (MNB). Over MKN, CT2016 shows better correlation (0.43) than GOSAT observation (0.08). In addition, the monthly amplitudes from CT2016 are closer to the flask observations, suggesting that satellite retrievals need much attention over the region. On the other hand, GOSAT observations were found to be in better agreement with flask observations over ASC. Zhang, Jiang, and Zhang (2015) also showed that GOSAT data was correlated well with ground observations and found to be more centralized, having high system stability, especially over the ocean.

TABLE 3.5: Summary of statistical relations of CT2016 and GOSAT observations with respect to flask observations. The statistical analysis was made using the monthly averaged covering the period from May 2009 to April 2014).

code	CT R	GOSAT R	CT Bias (ppm)	GOSAT Bias (ppm)	CT RMSD (ppm)	GOSAT RMSD (ppm)	number of data
ASC	0.58	0.93	1.05	1.84	4.46	1.07	39
ASK	0.90	0.90	-0.63	-0.76	1.97	2.23	60
NMB	0.75	0.91	1.40	1.13	3.12	1.56	60
IZO	0.99	0.97	0.24	-0.36	0.70	1.40	60
MKN	0.40	0.04	1.83	2.88	1.48	1.64	17
WIS	0.93	0.83	-1.57	-2.61	1.95	3.31	60

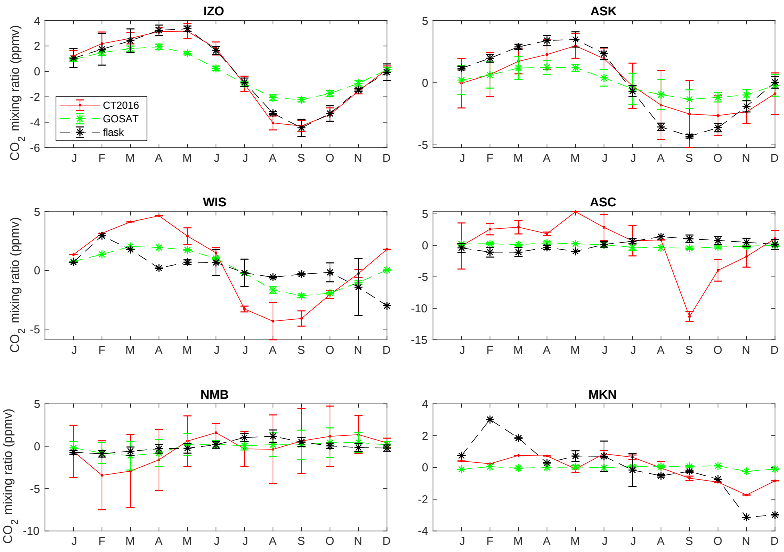

FIGURE 3.10: De-trended seasonal cycles of near surface CO_2 mixing ratio during 2009-2014 from CT2016 (red), GOSAT (green), and flask (black) observations. The standard deviation of the monthly variables is indicated by error bars.

CT2016 had show a better agreement over IZO and ASK. Moreover, CT2016 compared well with flask observations than GOSAT over these sites; almost all flask observations are within the standard deviations of the monthly mean of CT2016. However, GOSAT observations were found in better agreement with flask observations than CT2016 was over WIS and ASC. On the other hand, both CT2016 and GOSAT showed low agreement to flask observation over MKN (see Fig. 3.10). Similar to our previous discussion over sites in the Northern Africa (IZO, ASK and WIS), CT2016 underestimates near-surface CO_2 mixing ratio during August, September, and October (wet season) compared to GOSAT observation and overestimates during January to June. However, the CT2016 and the flask observations exhibit better agreement indicating a bias in GOSAT observation during the wet season.

3.3.5 Comparison of mean XCO_2 from NOAA CT16NRT17 and OCO-2

The strong El Niño event occurred during 2015-2016 provides an opportunity to compare the performance of CT16NRT17 during strong El Niño events. Because of the decline in terrestrial productivity and enhancement of soil respiration, the concentration of CO_2 increases during El Niño events (Jones et al., 2001). In this section, we compare mean XCO_2 of NOAA CT16NRT17 and NASA's OCO-2 covering the period from January 2015 to December 2016.

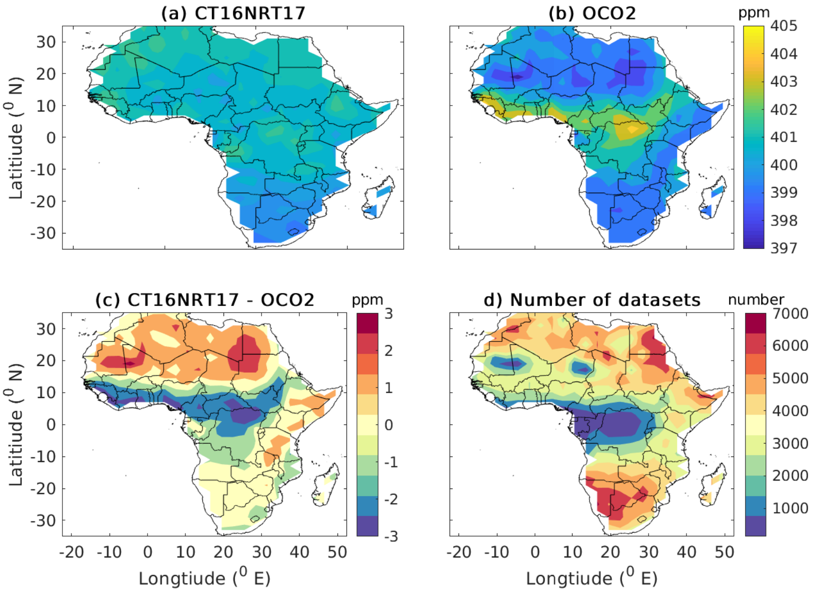

FIGURE 3.11: Distribution of two years average XCO_2 of CT16NRT17 **(a)** and OCO-2 **(b)** XCO_2 and their difference **(c)** gridded in $3^0 \times 2^0$ bins; and **(d)** the total number of datasets at each grid

The comparison was done based on the selection criteria discussed in Section 3.2. Fig. 3.11 shows mean distribution of XCO_2 from CT16NRT17 (Fig.

3.11a) and OCO-2 (Fig. 3.11b) over Africa's landmass. CT16NRT17 shows high ($>$ 400 ppm) XCO_2 values over North Africa, while these high XCO_2 values are observed over Equatorial Africa in the case of OCO-2 observation. The two datasets show a discrepancy over Equatorial Africa, where CT16NRT17 simulates low XCO_2 values (< 401 ppm) while OCO-2 observes high values of XCO_2 (> 401 ppm). Both datasets show moderate XCO_2 values which range from 397 to 400 ppm over Southern Africa. The XCO_2 distribution from OCO-2 is consistent with the maximum CO_2 concentration reported in a past study by Williams et al. (2007) implying that the CT16NRT17 likely underestimates XCO_2 values over Equatorial Africa. It is also possible that the discrepancy is a compounded effect of OCO-2 XCO_2 positive bias over the region (O'Dell et al., 2012; Chevallier, 2015). Fig. 3.11c shows the mean difference between two years mean of XCO_2 from CT16NRT17 and OCO-2, which is in the range from -2 to 2 ppm. Positive Bias indicates that CT16NRT17 is higher than OCO-2. However, high (<-2 ppm) negative mean difference between the two data sets over rain forest regions (the Gulf of Guinea and Congo basin) and ITCZ over Eastern Africa (South Sudan and southeastern Sudan) is observed implying that CT16NRT17 simulates lower XCO_2 values than that of OCO-2 observation over regions where vegetation uptake is strong. Conversely, high (>1) positive mean difference over the Sahara desert, Somalia and Tanzania implies CT16NRT17 simulates higher XCO_2 values than OCO-2 observation where the vegetation uptake is weak. Moreover, a positive (>2) mean difference over Egypt, Libya, Sudan, Chad, Niger, Mali and Mauritania is likely due to overestimates of XCO_2 emission from local sources by CT16NRT17. Overall, the two datasets show a fairly reasonable agreement with a correlation of 0.60 and an offset of 0.34 ppm, a regional precision of 2.57 ppm and a regional accuracy of 1.21 ppm (Table 3.6). The number of data used in the statistics is 1,659,411 over 426 pixels covering the study period, the distribution at each grid point is shown in Fig 3.11d.

TABLE 3.6: Summary of statistical relation between CT16NRT17 and OCO-2 observation.

Statistical tool	R	Bias (ppm)	RMSD (ppm)	std of Bias (ppm)	OCO-2 err (ppm)	CT16NRT17 std (ppm)	OCO-2 std (ppm)
Values	0.6	0.34	2.57	1.21	0.55	0.55	1.28

Fig. 3.12a shows the histogram of two years mean difference, which is characterized by a positive mean of 0.34 ppm and a standard deviation of 1.21 ppm. This suggests that CT16NRT17 simulates high XCO_2 as compared to observations from OCO-2 over Africa's landmass.

Because of the presence of spatial and temporal mismatch of some level between CT16NRT17 and OCO-2 datasets, it is important to assess the effect of

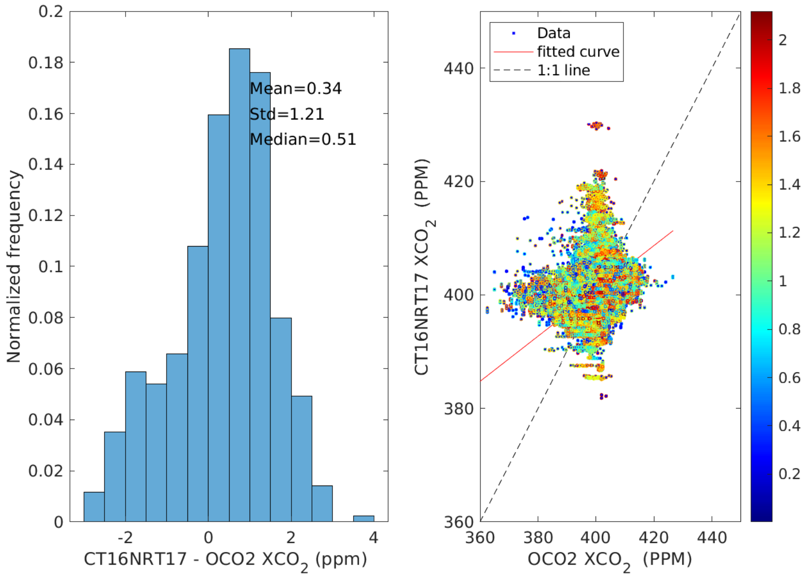

FIGURE 3.12: Histogram of the difference of CT16NRT17 relative to OCO-2 (left panel) and color code scatter diagram of XCO_2 concentration as derived from CT16NRT17 and OCO-2 (right panel). Color indicates the relative distance in unit of degrees as shown in colorbar between datasets.

the relative distance between the datasets. Fig. 3.12b shows a colour-coded distribution of the two datasets. In the figure, colour codes indicate the relative distance. The random scatter of blue dots implies that the statistical discrepancies do not arise from the relative distance between the two datasets. More specifically, a statistical comparison of datasets lower and higher than the 50^{th} percentile (1.2^0) shows the bias of 0.58 and 0.57 ppm, correlation of 0.57 and 0.57 and RMSD of 2.65 and 2.67 ppm respectively.

Fig. 3.13 shows the comparison of mean XCO_2 from CT16NRT17 and OCO-2 covering the period from January 2015 to December 2016. The number of data used is displayed in Fig. 3.11d. Fig. 3.13a depicts the bias which ranges from -2 to 2 ppm with a mean bias of 0.34 ppm. However, higher biases (<-2 ppm) are observed over Equatorial Africa along with the annual average location of ITCZ. Fig. 3.13b shows the correlation map with values from 0.2 to 0.8 over Africa's landmass. A good correlation of above 0.6 is seen over many regions of the continent, while a weak correlation of less than 0.2 and higher root mean square error (> 3 ppm) are observed over small pockets of Equatorial and Eastern Africa regions (see Fig. 3.13c). These regions also show a higher (> 0.65 ppm) error in satellite retrievals (see Fig. 3.13d). In addition, Fig. 3.11d shows that the number of observations is small (< 1000) over these regions.

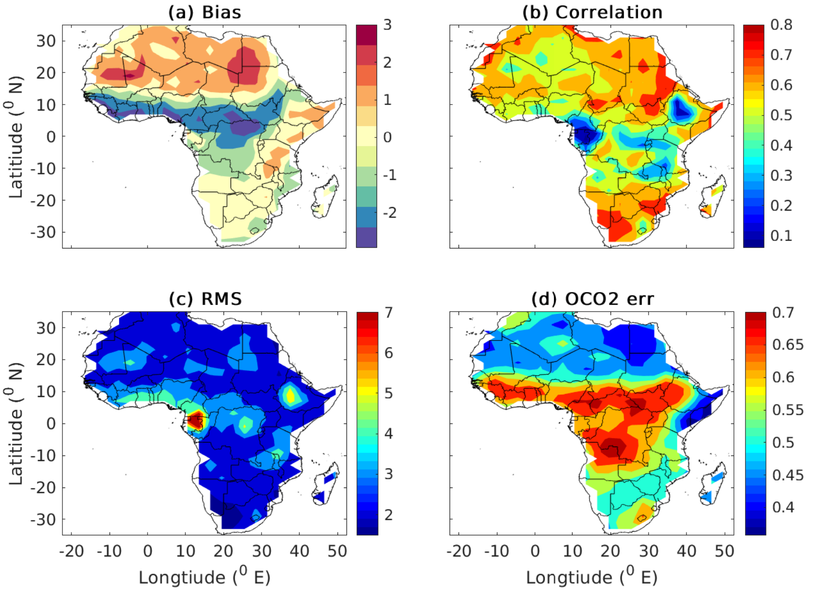

FIGURE 3.13: The bias (a), correlation (b), RMSD (c) of model and OCO-2 XCO_2 and mean posteriori estimate of XCO_2 error from OCO-2 (d).

This may contribute to the observed discrepancy over these regions. However, weak correlations are also observed over a wider area in North Africa such as Mauritania, Mali, Algeria and some regions of Niger where satellite errors are low and sufficient data are obtained. Poor correlation and higher RMSD values are observed over Southwest Ethiopia.

3.3.6 Comparison of monthly average time series of NOAA CT16NRT17 and OCO-2 XCO_2

Figs. 3.14 - 3.16 show a two-year monthly average time series comparison of XCO_2 from CT16NRT17 and OCO-2 over North Africa, Equatorial Africa and Southern Africa respectively. Fig. 3.14a shows the existence of a good agreement between the two datasets in describing pattern over North Africa. Moreover, both datasets show a decreasing trend of XCO_2 from May to September while an increasing trend from October to April. On the other hand, consistent with the climate condition and associated CO_2 exchange, the monthly mean XCO_2 shows a maximum value of 403.37 ppm for CT16NRT17 and 402.06 ppm for OCO-2 during May. Conversely, a minimum concentration of 398.77 ppm from CT16NRT17 simulation and 398.27 ppm from OCO-2 observation is found in September. In addition, both CT16NRT17 and OCO-2 show maximum XCO_2 values (402.15 ppm for CT16NRT17 and 402.03 ppm for OCO-2) in December.

These peak values in December are not surprising, because the 2015-2016 El Niño started in March 2015 and reached a peak in December 2015, which added extra CO_2 into the atmosphere (Chatterjee et al., 2017). Fig. 3.14a also shows that XCO_2 from CT16NRT17 simulation are higher than OCO-2 observations over North Africa.

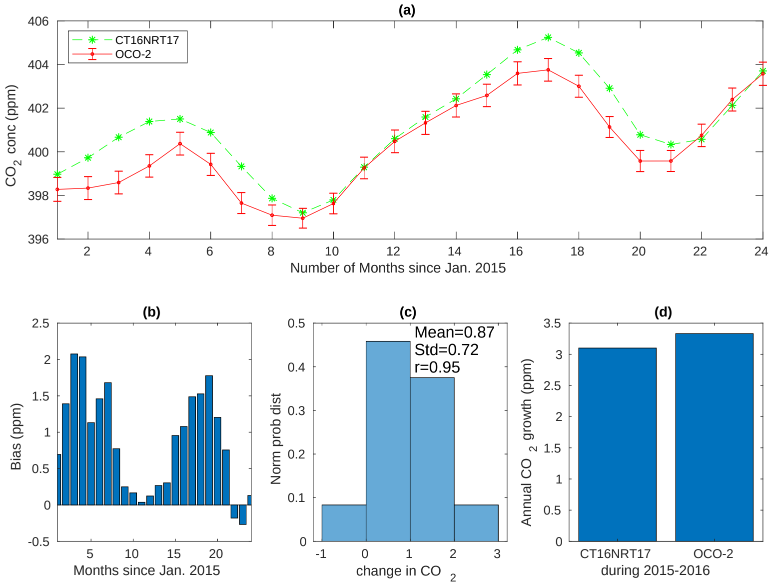

FIGURE 3.14: The monthly mean time series of CT16NRT17 and OCO-2 from January 2015 to December 2016 averaged over North Africa (a), bias associated with the monthly means (b), the histogram of difference (c) and the annual growth rate obtained by subtracting the mean from the mean of the next year (d). The error bars in (a) shows the OCO-2 a posteriori XCO_2 uncertainty.

Fig. 3.14b shows the monthly mean difference between CT16NRT17 and OCO-2 which ranges from -0.5 to 2 ppm. OCO-2 XCO_2 observations are lower than CT16NRT17 by 2 ppm during March and April 2015. Starting from August 2015, the difference between the two datasets is minimum; On the other hand, a maximum difference of exceeding 1.5 ppm was observed during MAM which can be mentioned as a burning season of Northern Africa, as the area north of the equator was burned mostly from March to June (Hao and Liu, 1994). The observed lower XCO_2 values from OCO-2 observations than that of CT16NRT17 simulation will be a consequence of much respiration which exceeded photosynthesis when vegetation uptake is weak following the strong El Niño and dry season over North Africa. Furthermore, intense burning of the forest during this season which will further be intensified by the strong El Niño may cause unpredictable aerosol loading, and thereby this inaccurate estimation of aerosol loading could be suggested as the most likely source for the observed discrepancy. Moreover, Fig. 3.14c displays a monthly mean regional mean bias of 0.87 ppm, correlation of 0.95 and a root mean square deviation of 0.72 ppm between CT16NRT17 and OCO-2 XCO_2. This implies that CT16NRT17 is in a good agreement with OCO-2. However, a small discrepancy arose most likely due to a strong anthropogenic emission from Nigeria, Egypt and Algeria.

Figs. 3.15a - 3.16a show monthly mean time series of XCO_2 from the model and OCO-2 instrument over Equatorial Africa and Southern Africa which is also in good agreement in terms of pattern. However, the figures show that CT16NRT17 simulations are lower than those of OCO-2 during October, November and December whereas it is opposite during April, May and June over Equatorial Africa and Southern Africa. Figs. 3.15b and 3.16b depict a seasonal bias in the monthly time series over Equatorial Africa and Southern Africa respectively. Positive biases are observed during dry seasons while negative biases are during wet seasons. Moreover, the datasets have monthly averaged regional mean biases of 0.13 and 0.11 ppm, correlation of 0.90 and 0.94, RMSD of 0.84 and 0.73 ppm over Equatorial Africa and Southern Africa respectively. This shows that the existence of a better agreement between CT16NRT17 and OCO-2 over these regions in terms of monthly average regional mean values. Figs. 3.14d-3.16d show both CT16NRT17 and OCO-2 are in good agreement in estimating the annual growth rate. Patra et al. (2017) found a global mean of more than 3 gigatons of CO_2 added to the atmosphere due to the strong El Niño event that occurred during 2015-2016. In agreement with this, both CT16NRT17 and OCO-2 shows an annual growth rate that ranges from 3.10 to 3.42 ppm year^{-1} of XCO_2 over Africa's landmass (see also Table 3.7). However, overall regions of Africa's landmass CT16NRT17 shows lower XCO_2 annual growth rate than those of OCO-2.

TABLE 3.7: Annual growth rate (AGR) of XCO_2 over Africa land mass from CT16NRT17 and OCO-2. The results are obtained as the mean annual difference of 2015 and 2016 values

Region	AGR of CT (ppm year^{-1})	AGR Of OCO-2 (ppm year^{-1})
North Africa	3.10	3.33
Equatorial Africa	3.14	3.42
Southern Africa	3.20	3.16

3.3.7 Comparison of seasonal means of NOAA CT16NRT17 and OCO-2 XCO_2

Fig. 3.17 depicts seasonal means of XCO_2 over Africa's landmass from CT16NRT17 (left panels), OCO-2 (middle panels) and their difference (right panels) covering

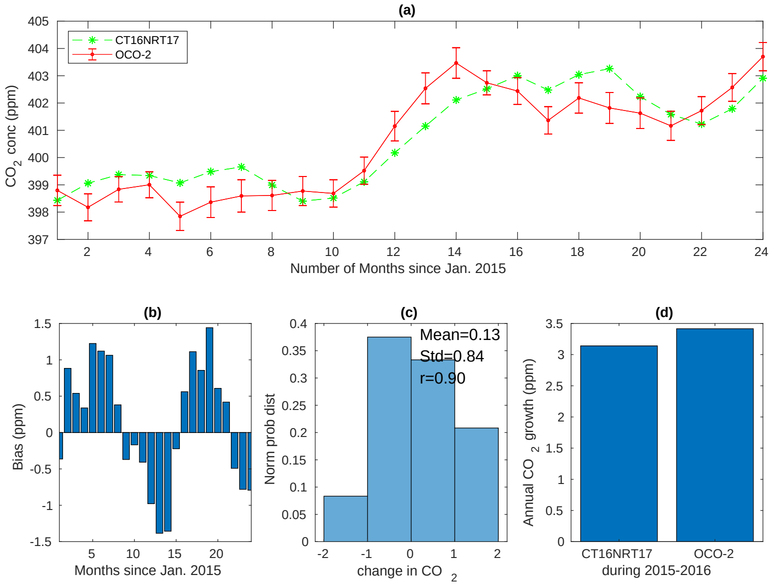

FIGURE 3.15: The same as in Fig. 3.14 but over Equatorial Africa.

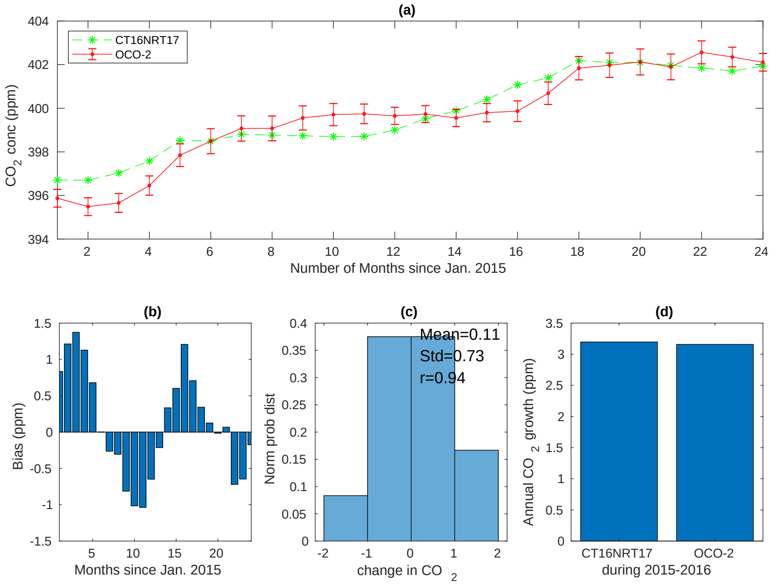

FIGURE 3.16: The same as in Fig. 3.14 but over Southern Africa.

a period of January 2015 to December 2016. The white space has seen over some regions (e.g., Mali during JJA) is due to insufficient coincident satellite data according to the selection criteria during these seasons. XCO_2 increases from winter to spring and then decreases from spring peak to summer minimum over the whole continent. The decrease from spring maximum to summer continued into autumn over the northern half of Africa in contrast to the southern half of Africa which exhibits an increase in XCO_2. The decrease from spring to autumn (northward of equator) and until summer (southward of equator) is likely to be a consequence of the land vegetation awakening from dormancy of winter and partly spring. Conversely, the decomposition of died and decayed vegetation which began in autumn and continued throughout winter adds extra CO_2 leading to a maximum concentration during spring (Idso, Idso, and Balling Jr, 1999). In agreement with this, both CT16NRT17 and OCO-2 show maximum XCO_2 during MAM over North Africa and during SON over Southern Africa. Conversely, minimum concentrations are observed during SON over North Africa and during DJF over South Africa.

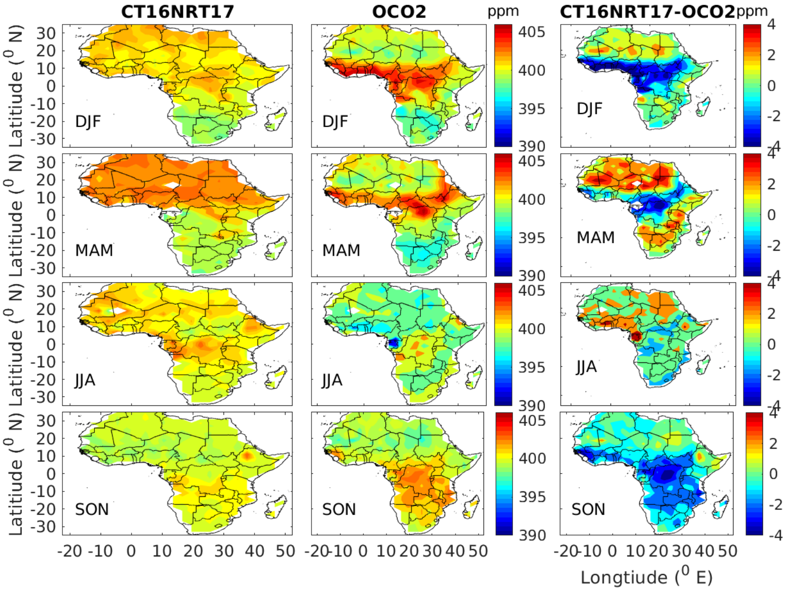

FIGURE 3.17: Seasonal mean of CO_2 for NOAA CT16NRT17 (left panels) and OCO-2 (middle panels) and their difference (right panels).

Fig. 3.17 (right panels) shows the seasonal mean difference of CT16NRT17 and OCO-2. A higher mean difference greater than 1 ppm is observed over North Africa during DJF and MAM when the vegetation cover over the region decreases and in the presence of an intensive burning of the northern savanna during this season (Hao and Liu, 1994). This indicates that XCO_2 values from CT16NRT17 are higher than that of OCO-2 when vegetation uptake is weak and there is more fire. On the other hand, a higher negative mean difference of less than -2 ppm are observed over Equatorial Africa during DJF and SON over Southern Africa. This difference between CT and OCO-2 arises likely due to grass fires from the dry savanna. Consistent with a report by Liang et al. (2017), low seasonal variability is observed between CT16NRT17 and OCO-2 in the range from -4 to 4 ppm with greater amplitude over North and Equatorial Africa than over Southern Africa (see Fig. 3.17 (right panels)). During the dry seasons OCO-2, overestimates values over Northern Africa, but it underestimates for Southern Africa.

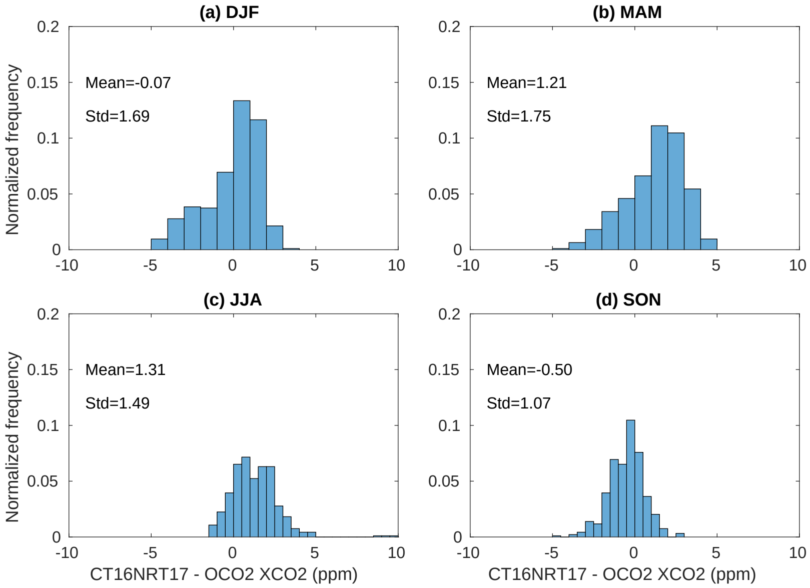

FIGURE 3.18: Histogram of difference for the seasonal CO_2 climatology for DJF (a), MAM(b), JJA (c) and SON (d) seasons.

Fig. 3.18 shows the histogram of seasonal mean difference of CT16NRT17 and OCO-2. The smaller standard deviations of 1.49 and 1.07 were observed during JJA and SON. On the other hand, a higher standard deviation of 1.69 and 1.75 ppm are observed during DJF and MAM respectively. These results indicate that CT16NRT17 and OCO-2 show a better consistency during the wet season and this consistency decreases as the vegetation cover decreases over most regions of Africa landmass during the dry season.

3.3.8 Comparison of OCO-2 and CT16NRT17 with flask observations

TABLE 3.8: Summary of statistical relation between CT16NRT17 and OCO-2 observations with respect to flask observations. The statistical analysis were made using the monthly averaged covering the period from May 2009 to April 2014).

code	CT R	OCO2 R	CT Bias (ppm)	OCO2 Bias (ppm)	CT RMSD (ppm)	OCO2 RMSD (ppm)	number of data
ASC	-0.14	0.97	3.93	-0.48	7.63	1.10	22
ASK	0.97	0.93	-0.47	-2.60	0.80	1.88	24
CPT	0.91	0.98	0.62	0.90	0.80	0.53	24
NMB	0.28	0.42	2.14	0.09	3.27	2.02	24
IZO	0.93	0.97	0.46	-2.16	1.10	1.33	24
LMP	0.02	-0.09	-4.20	-4.08	3.82	3.61	18
SEY	0.68	0.71	-0.98	-0.98	2.23	1.47	22
WIS	0.73	0.68	-1.64	-4.84	2.90	3.25	24

Monthly CT16NRT17 near-surface CO_2 values have a better sensitivity over IZO and ASK both in terms of a temporal pattern (phase) and amplitude than

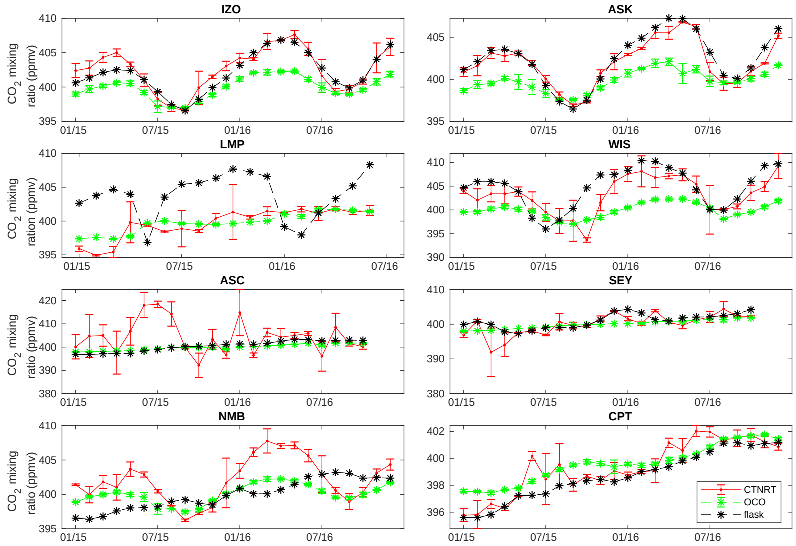

FIGURE 3.19: CO_2 from CT16NRT17, OCO-2 and flask observations.

OCO-2 (see Fig. 3.19) where observations from OCO-2 mostly underestimate CO_2 mixing ratio at these two flask sites. Over LMP and WIS, both CT16NRT17 and OCO-2 have moderate sensitivity in capturing the seasonal cycle. On the other hand, OCO-2 has a better sensitivity over ASC and SEY. In addition, near-surface CO_2 from both CT16NRT17 and OCO-2 was found to have poor correlations with flask observations over NMB and CPT. However, OCO-2 has closer sensitivity in capturing amplitudes than CT16NRT, where CT16NRT17 overestimates CO_2 at these flask sites. In general, CT has a better performance over sites located at high altitude (IZO, ASK) where satellite observations underestimate CO_2 mixing ratio. Conversely, satellite observations have better performance over low altitude island sites (ASC and SEY) as revealed by better agreement with flask measurements.

3.4 Summary

In this chapter, the consistency of the Carbon Tracker model in capturing the atmospheric XCO_2 was tested by comparing XCO_2 simulated by the Carbon Tracker model against other two independent CO_2 dedicated satellite observations: GOSAT and OCO-2. Carbon Tracker shows good skill in capturing the spatiotemporal distribution of XCO_2 and shows a bias of -0.28 and 0.34 ppm, correlations of 0.83 and 0.60 and root mean square deviation of 2.30 and 2.57 ppm for GOSAT and OCO-2 respectively. Carbon Tracker can capture more than 93% of the retrieved XCO_2 from GOSAT and OCO-2 observations. The sampled near-surface CO_2 profiles from these satellites and Carbon Tracker were found in good agreement with available in-situ CO_2 flask data from Assekrem, Algeria; Mt. Kenya; Gobabeb, Namibia; and Cape Town; as well as with data from the coast of Seychelles, Ascension Island, and Canary Island. CT agrees well with measurements in terms of pattern and amplitude, also in capturing the observed seasonal cycles over different parts of the continent. However, this agreement deteriorates over Equatorial and Southern Africa in terms of amplitude. The Carbon Tracker model shows a seasonal bias related to the vegetation thriving and end-thriving seasons. The model has also shown some weakness in XCO_2 estimation over some regions of tropical and Northern Africa. For example, GOSAT observation shows better agreement and small bias with the flask measurements during the wet season than CT2016, thereby incorporating satellite observations in the model assimilation will further enhance the quality and resolution of Carbon Tracker datasets. The possibility of free access of spatiotemporally smoothed datasets along with its good agreement with the known seasonal climatology of the regions that determines carbon source and sink levels, indicates that CT model products are the preferred dataset for carbon cycle study of the region.

Chapter 4

Sun-induced Fluorescence and Near-Infrared Reflectance of vegetation track the seasonal dynamics of gross primary production over Africa

4.1 Background

The seasonal dynamics of GPP over tropical ecosystems have been discussed widely due to contrasting observations from remote-sensing and eddy covariance platforms over the South American Amazon basin (see Restrepo-Coupe et al. (2013) and references therein). In addition to photosynthetic active radiation (PAR) and vapour pressure deficit (VPD), there is a clear contribution of soil moisture stress for short vegetation, and for changing the photosynthetic capacity of leaves as a function of age in broadleaf vegetation (Xiao et al., 2006; Huete et al., 2006), in shaping the GPP seasonal cycle. In seasonally wet forests, GPP typically peaks in the wet season when VPD is low and soil moisture high, and declines in the early dry season only to increase again well before the rainfall minimum, as freshly grown leaves take advantage of the maximum in PAR (Lopes et al., 2016). Areas with low vegetation (shrubs, grasses, and sparse trees) instead show a decline of GPP throughout the dry season, as soil moisture and high VPD limit the productivity of the vegetation. These patterns were confirmed in three separate studies using remote-sensing observations of sun-induced fluorescence from GOSAT (Lee et al., 2013), GOME-2A (Koren et al., 2018), and TROPOMI (Doughty et al., 2019) over the Amazon.

Similar to SIF, the near-infrared of vegetation (NIRv), which is the product of the normalized vegetation index (NDVI) and the total scene near-infrared reflectance (NIRT), was found to provide a good proxy for GPP (Badgley, Field, and Berry, 2017; Turner et al., 2019). Therefore, we use the Sun-Induced Fluorescence of Terrestrial Ecosystems Retrieval (SIFTER, Schaik et al., 2020) data from the GOME-2A instrument and NIRv from MODIS to assess the usefulness of these signals to capture the seasonality and magnitudes of GPP derived from six eddy covariance flux towers from Africa in the overlap years between the years 2007-2014. We also test the robustness of SIF and NIRv to track the seasonality of GPP for the major biomes in comparison to the widely used machine-learning approach of MPI-BGC GPP, as well as to other vegetation remote-sensing indices like NDVI (Kong et al., 2016) and EVI (Arvor et al., 2011). Furthermore, we assess the relationship between the satellite observations and (model-generated) soil moisture (SM) and incoming shortwave (SWR) radiation in the region. Finally, we derived a plant-functional specific linear relation between eddy-covariance GPP and SIF/NIRv, to quantify the integrated GPP from remotely-sensed signals.

4.2 Analysis methods

To compare the gridded data sets (SIF, NIRv, MPI-GPP) with the GPP measurements from flux towers, we extracted data from a $4^\circ \times 4^\circ$ window surrounding each flux tower (see Table 2.3). The flux towers have a footprint of about 1 km^2 and it is hard to compare them to areas that are 200 km^2 off the tower, which includes many vegetation types. However, we use the vegetation mask to exclude grid cells with different vegetation from the tower's vegetation; this will account for the land heterogeneity of the regions (see Fig. 2.1e). The variations in climate conditions were addressed by splitting up the shrubs and C4 grasses over the Northern and Southern Hemispheres. The empirical relationship between GPP and SIF is complicated due to the fact that we only observe a very small fraction of the emitted SIF signals, which also depends on the direction of observation (Porcar-Castell et al., 2014). Even if the mechanistic link between remotely sensed vegetation reflectance and GPP is complex (Porcar-Castell et al., 2014), Guanter et al. (2014) and Sun et al. (2017) showed that a simple linear relationship between SIF and tower-based GPP as a reasonably convenient framework for presenting and evaluating arguments and counterarguments for the SIF-GPP relationship. Here, we predict GPP from these remotely sensed vegetation reflectances using a linear regression between GPP and these signals as:

$$y = ax + b \tag{4.1}$$

where y is the GPP obtained from SIF or NIRv signals, x is SIF or NIRv signal. a and b are the slope and y-intercept of the fitting line. The conversion of SIF and NIRv to GPP is achieved by applying fitting to all monthly SIF and NIRv values for each vegetation type separately.

The linear relationship between SIF and GPP in Eq. 4.1 may be rationalized with the formulation based on the concept of light use efficiency (LUE) (Monteith, 1972) in a simple parametric LUE-model GPP as follows:

$$GPP = APAR \times LUE_p \tag{4.2}$$

where APAR is the absorbed photosynthetically active radiation expressed in radiance units and LUE$_p$ is the light use efficiency of photosynthesis, which represents the efficiency of energy conversion for gross CO_2 assimilation. Similarly, SIF can be expressed as:

$$SIF = APAR \times LUE_f \tag{4.3}$$

where LUE$_f$ is the effective light use efficiency of canopy fluorescence, which accounts for both the fluorescence yield and the fraction of emitted photons escaping the canopy (Damm et al., 2015). These equations can be combined making the dependence on light implicit,

$$GPP \approx SIF \times \frac{LUE_p}{LUE_f} \tag{4.4}$$

SIF has negative values due to noise in its retrieval and a zero value of SIF may not result in a zero value, whereby we do not force the regression to pass through the origin and as there will be intercepts 'b' as in Eq. 4.4. Furthermore, the linear relationship between NIRv and SIF can be rationalized by the fact that both SIF and NIRv are jointly dependent on the flux of the fractional interceptance of vegetation, incoming solar radiation, and the fraction of photons that escape from the canopy, these two are strongly related measurable fluxes (Zeng et al., 2019).

4.3 Seasonal dynamics of gross primary productivity

4.3.1 GPP proxies and eddy-covariance derived GPP estimates

Spatial patterns in climatological NIRv, SIF, and MPI-BGC GPP are very similar across large scales, with maximum annual mean productivity in tropical broadleaf forests. Fig. 2.1a-c shows that productivity changes strongly at the borders of the plant-functional types, which is interesting because only the MPI-BGC product was actually informed by a PFT-map in its machine-learning, while the satellite observations provide independent spatial views on productivity. SIF and NIRv products suggest additional variations within PFTs not represented in the MPI-BGC map, as would be expected based on the higher volume of observed data in the remote-sensing products (see Fig. 2.1a-c).

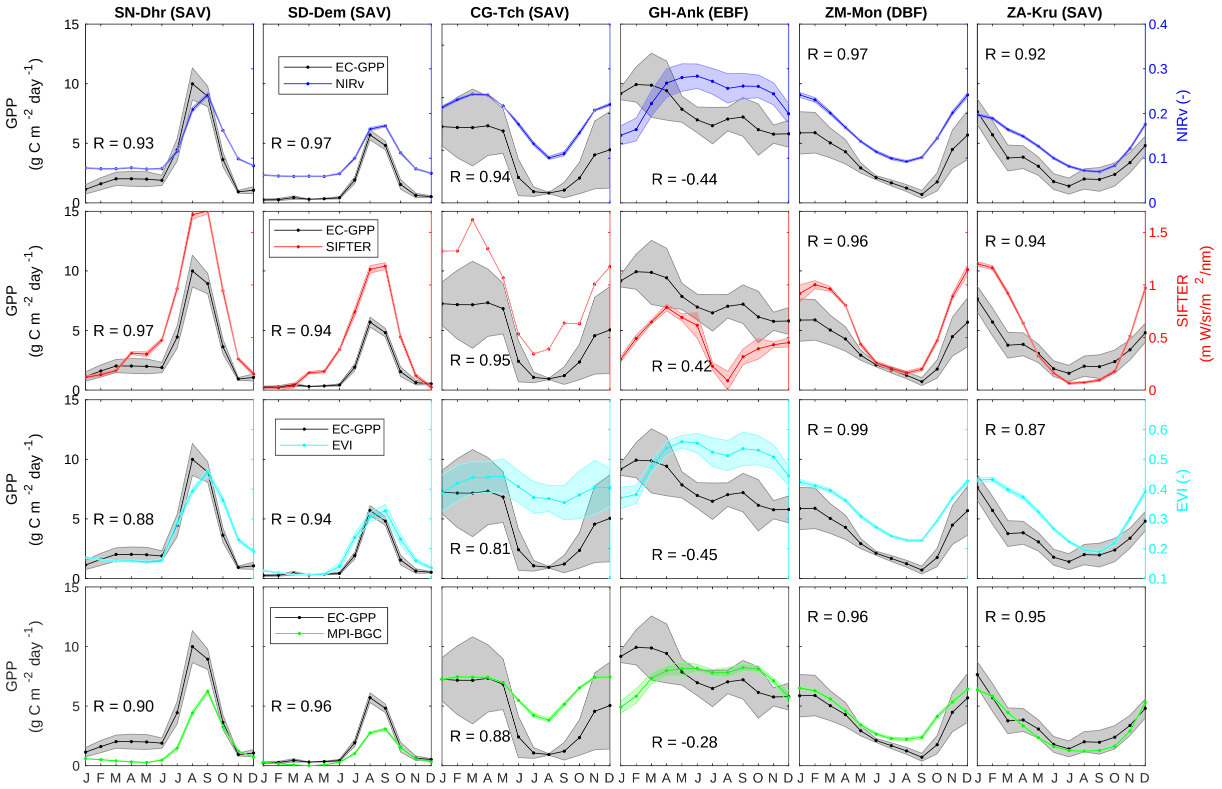

FIGURE 4.1: The skill of NIRv, SIF, EVI and MPI-BGC GPP in capturing the seasonal cycle of GPP from flux towers. The shaded area indicates the standard deviation around the monthly means. Note that NIRv, SIF and EVI do not have the same unit as GPP and their values are provided on the secondary y-axis.

NIRv, SIF, EVI and MPI-BGC GPP generally capture the seasonal patterns of tower GPP well, except at the Ghana GH-Ank flux tower where all products only SIF yields the expected positive correlation with eddy-covariance derived GPP observations. Fig. 4.1 shows the observation-derived and simulated seasonal cycles of GPP, and the generally high (R>0.8) seasonal correlations. SIF shows more rapid changes in signal during the transition from wet-to-dry periods than other proxies. The May-June-July period at the Savannah site CG-Thc is an example and indicates that SIF more rapidly responds to the decline of photosynthesis in wilting grasses, which are still green and reflective enough to affect NDVI, EVI, and NIRv. Such a more immediate response of SIF to water stress was also observed by others (Chen et al., 2019; Tian et al., 2020).

Results from all sites depict the correlation between FLEXNET2015 GPP and Satellite fluorescence (NIRv and SIF) are better than the VIs (NDVI and EVI) and MPI-BGC GPP (Fig. 4.2). Even over evergreen forests where GPP is high throughout the season (see Fig. 2.1a-c) suggesting that these two are good proxies for GPP. Compared with NDVI, EVI showed a much better relation to tower GPP. On the other hand, SIF had a strong correlation with tower GPP over most towers than all other proxies. Leading that SIF is a better proxy in estimating GPP at the ecosystem level. Luus et al. (2017) also found SIF as a superior GPP proxy than vegetation-derived proxies.

SIF and NIRv have a higher monthly correlation with the EC-GPP at most of the towers than EVI and MPI-BGC GPP (Fig. 4.2). Luus et al. (2017) also found this for other flux towers, and suggested this is because the chlorophyll content seen through NDVI and EVI adapts slowly to stress and it can take weeks for leaves to lose their green colour (Hew, Krotkov, and Canvin, 1969). EVI and NDVI not only have generally much weaker correlations but also show saturation when GPP is high (Fig. 4.2). We found the relationship between SIF/NIRv and GPP for croplands to be the strongest, with r > 0.90 for C4 vegetation at both the Sudan (SD-Dem) and Senegal (SN-Dhr) sites (Fig. 4.2). A much weaker relation was obtained for broadleaf evergreen vegetation such as in Ghana (GH-Ank). This agrees with Li et al. (2018), who also showed a weak relationship between SIF and GPP over rain forest sites. Previous authors suggested this may result from the inefficiency of satellite measurements to detect the canopy activities of tropical forest (Tang and Dubayah, 2017), due to limitations in their retrieval due to atmospheric cloud contamination (Frankenberg et al., 2014; Doughty et al., 2019), or from the EC measurement technique itself (Hayek et al., 2018).

Eddy covariance measurements over tropical rainforests regions are more complicated than over flat vegetation due to the presence of uneven tall canopies (Mercado et al., 2006). This comes on top of the uncertainty incurred on the

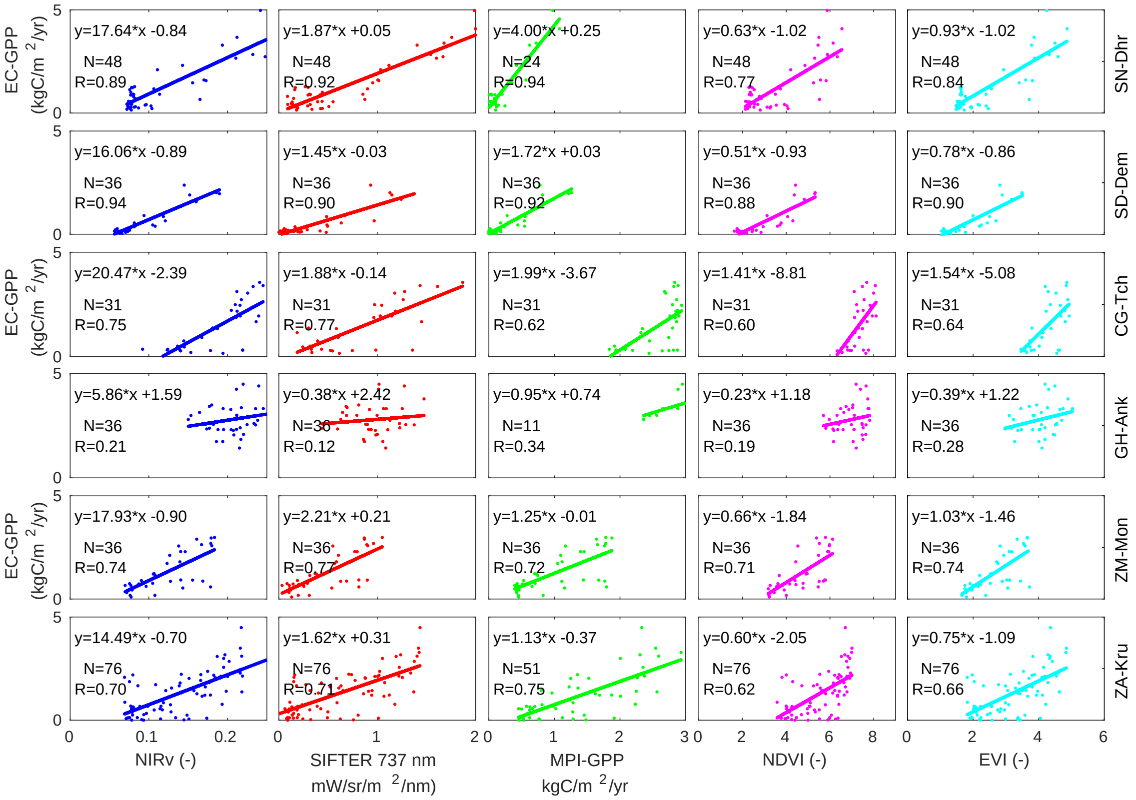

FIGURE 4.2: Comparison of eddy covariance GPP with NIRv, SIF, MPI-BGC GPP, NDVI and EVI for major biomes around the flux-tower. To obtain sufficient data the comparison is made by averaging monthly values within a 4° × 4° window enclosing the tower. Furthermore, to account for vegetation heterogeneity of the land, grid cells with a different vegetation type than for the tower location were masked.

derived GPP, which requires a partitioning of the measured net ecosystem exchange during turbulent conditions (Reichstein et al., 2005). The methodology used assumes a temperature-dependency of ecosystem respiration to remove its influence during the daytime, such that GPP can be determined from the residual of measured NEE and measurement-derived TER. For tropical sites, this T-dependency is often assumed negligible (Restrepo-Coupe et al., 2013). The partitioning approach is furthermore not well-tested for tropical ecosystems because of a lack of long data records, the larger uncertainty in determining nighttime TER (Kruijt et al., 2004), and the often seen nighttime storage that results in peak NEE fluxes in the early morning (Araújo et al., 2002). Finally, tropical TER is likely to experience larger control of precipitation and moisture on TER (Chambers et al., 2004).

The tower GPP from the GH-Ank site shows the limited seasonality in GPP over Evergreen Tropical Forest vegetation, which is poorly captured by all products (Fig. 4.1). Where NIRv, EVI, and MPI-BGC all show a phase-lag of nearly

4-months, SIF manifests a double peak structure and much too low annual mean SIF relative to the other EC-sites. These results are illustrative for tropical ecosystems, where GPP variations are irregular and strongly coupled to leaf phenology of vegetation (Restrepo-Coupe et al., 2013; Restrepo-Coupe et al., 2017). We suggest this may be due to the large resolution of the satellite pixels for GOME-2, resulting in possible inclusion of low SIF-values from the neighbouring ocean. In general, SIF and NIRv were better proxies in capturing the tower GPP over most sites. The relationships can be improved by using a higher result in products instead of these coarse resolutions. Here we used SIF from the GOME-2 instrument which has a larger footprint (40 × 80 km^2) and global gridding with a spatial resolution of 0.5° × 0.5° at monthly temporal. TROPOMI SIF is a promising alternative for future studies of the African carbon cycle. TROPOMI SIF has a higher spatial resolution than GOME-2 SIF and a more frequent coverage. Global TROPOMI SIF data was first shown by Köhler et al. (2018). Their study also included a detailed view of the North-African Nile Delta. In addition, Doughty et al. (2019) used TROPOMI to study the seasonality of the Amazon, showing the capability of this instrument to capture the seasonal dynamics of tropical ecosystems. Moreover, high resolution (0.05° × 0.05°) SIF can be modeled using explanatory variables which are available at both fine and coarse resolution (Guanter et al., 2014; Zeng et al., 2019).

For a more detailed look, we also compare EC-GPP to daily NIRv signals, derived from high-resolution (0.05° × 0.05°) MODIS radiances instead of coarse averaged MODIS NIRv (0.5° × 0.5°). At this daily timescale, we again find a very strong correlation over Northern Africa, while this correlation decreases for the equatorial sites Fig. 4.3. And again, we see a weak correlation at GH-Ank, Ghana (Fig. 4.3 Gh-Ank). The high-resolution NIRv mostly improves the comparison for sites with more heterogeneous vegetation cover (GH-Ank and ZM-Mon, ZA-kru), whereas no significant improvement for less heterogeneous sites (SN-Dhr and SD-Dem). In contrast to the low daily correlation for tropical evergreen broadleaf forest (GH-Ank, $R = 0.02$), the correlation in the interannual variation of NIRv and GPP is higher ($R = 0.28$). These results are illustrative for tropical ecosystems, where GPP variations are irregular and strongly coupled to photosynthetic capacity changes of vegetation (Restrepo-Coupe et al., 2013; Restrepo-Coupe et al., 2017).

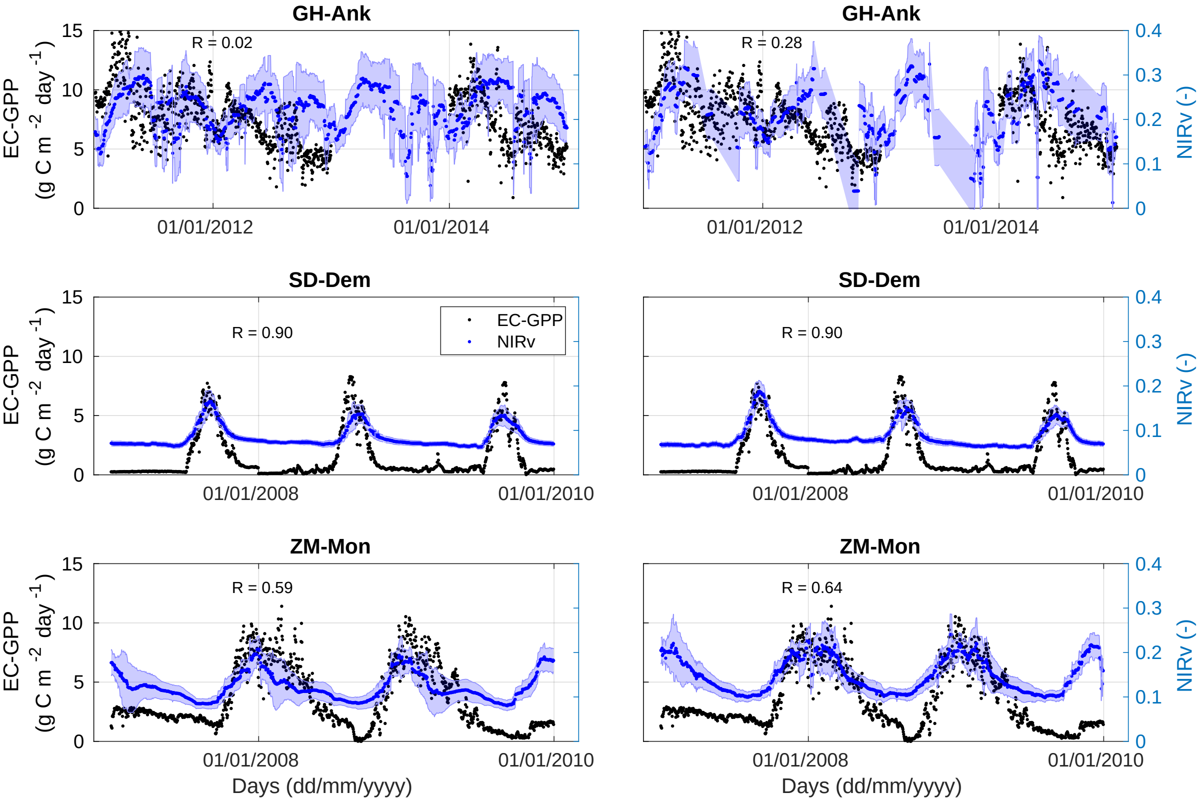

FIGURE 4.3: Comparison of coarse NIRv at 0.5° × 0.5° (left panels) and high resolution NIRv at 0.05° × 0.05° (right panels) with flux tower measured GPP (EC-GPP) for a selection of three African flux towers (GH-Ank, SD-Dem and ZM-Mon). The temporal correlation between NIRv and EC-GPP is given in each panel.

4.3.2 GPP proxies across the major biomes of Africa

We next extend this view from the level of individual towers to the scale of six major biomes in Africa (Fig. 2.1e) by spatially averaging our productivity products. Also then, wet months show higher SIF and NIRv values than dry months for all biomes of the region. Both SIF and NIRv show a strong linear relation with that of the MPI-BGC GPP estimates. Signals from both SIF and NIRv were correlated well with MPI-BGC GPP over these biomasses with a correlation of ($R^2 > 0.85$ for NIRv and $R^2 > 0.77$ for SIF). However, the correlation was moderate for broadleaf evergreen forests with a correlation of 0.38 for NIRv and 0.16 for SIF (see Table 4.1). This seasonality shown in Fig. 4.4 agrees closely with that seen for similar biomes in the Amazon (Girardin et al., 2016; Koren et al., 2018) and confirms the known strong water-control over GPP in tropical vegetation (Abdi et al., 2017; Bonal et al., 2016). Correlations with shortwave radiation are thus strongly negative, especially over short vegetation like shrubs and grasses. Over evergreen forests, SIF and NIRv show a double-peaked seasonality and a decrease of productivity during the dry seasons despite high SWR and high leaf area index (see Fig. 4.4 Broadleaf evergreen), suggesting an influence of photosynthetic capacity on GPP that has been noted before to be not yet represented by most biosphere models and light use efficiency models (Bhattacharya, 2018). Clouds can strongly reduce direct solar radiation during the wet season, which increases the ratio of diffuse versus direct solar radiation, possibly increasing the productivity (Hollinger et al., 1999).

Mostly, EVI and MPI-GPP closely agree on the satellite-observed seasonality at these larger scales, but EVI appears late in simulating the wet-dry season (Sep-Dec) decline in signal for C3 grasses and shrubs (see SIF-vs-EVI hysteresis plots in Fig. 4.5). This delayed response resembles that described by Luus et al. (2017) for high-latitude short vegetation, which greened up in EVI 9 days before spring photosynthesis started. Our response is opposite in the sense that we see photosynthesis decline already before the seasonal brown down of the savannah. To further investigate this, we, therefore, turn to the main drivers, water and light, of the African seasonal cycle in GPP.

Remote sensing data-driven models are widely used for estimating plant photosynthesis and they are linearly dependent on the amount of solar illumination, amount of water content in the soil and plant canopy (Ceccato et al., 2001). Most of these models assume information in Fraction of Absorbed Photosynthetically Active Radiation (fAPAR) and Vapor Pressure Deficit (VPD) are sufficient to accurately estimate the responses of GPP to drought. However, deficits in soil moisture and their effects on GPP are not necessarily captured by fAPAR or VPD (Stocker et al., 2019) and results in large uncertainties in these GPP estimations.

The biome-integrated productivity in Africa has strong seasonally which strongly controlled by soil moisture, with a weak influence of light availability superimposed. In Fig 4.6 this is recognized by the positive correlation between SIF/NIRv (which independently display the exact same patterns) and soil moisture in both hemispheres. Peak productivity coincides with peak soil moisture that occurs in September on the NH, and in March on the SH. Interestingly, the lead up to peak productivity occurs more slowly than its subsequent decline even at the same soil moisture levels, evident when comparing the pairs of months (August, October) and (July, November) for the NH, or pairs (January, April) and (December, May) for the SH. Translating these points to the SWR diagrams in panels (a) and (c), a notable difference between the hemispheres appears: in the SH peak productivity occurs while light-availability continues to decline, creating the elliptical shape of the hysterics diagram. In the NH however, peak productivity happens at minimum light-availability becoming larger

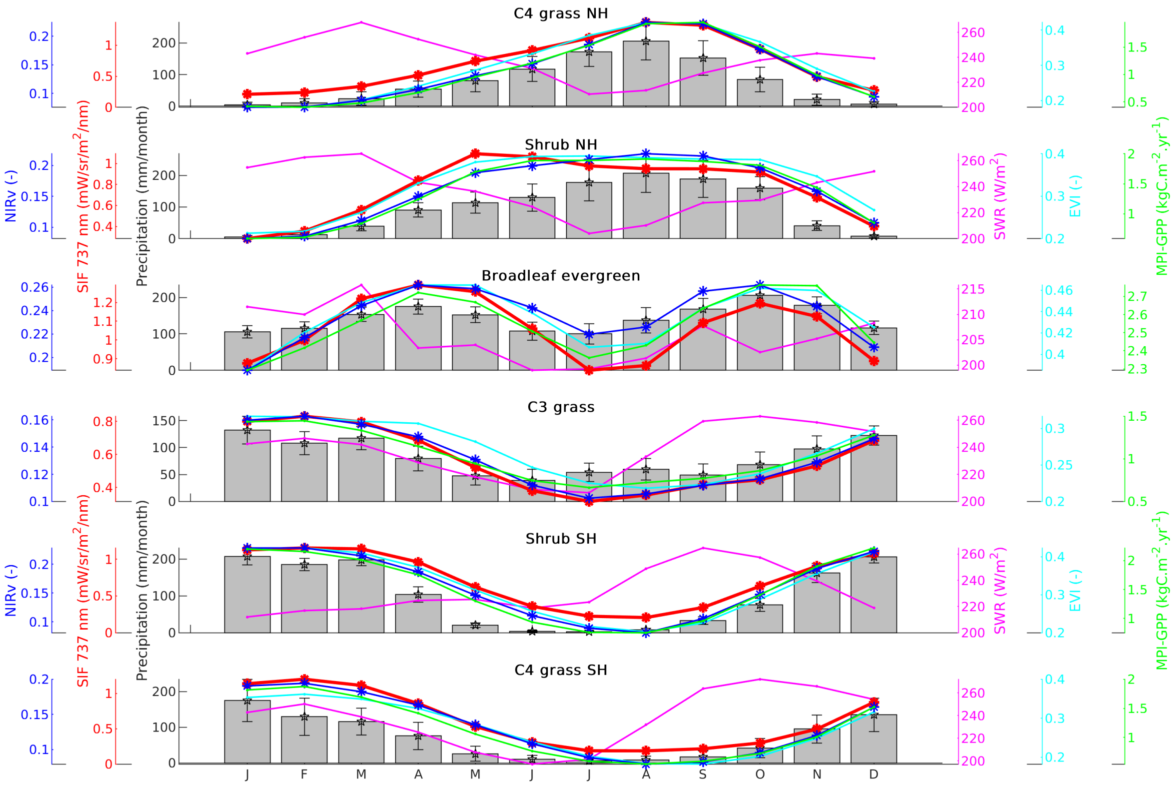

FIGURE 4.4: Seasonal cycles of NIRv, SIF, precipitation, short wave radiation (SWR), EVI and MPI-GPP at 0.5° × 0.5° resolution over major biomes of Africa covering the period from 2007 to 2011. The error bars provided for precipitation denote the standard deviation around the mean.

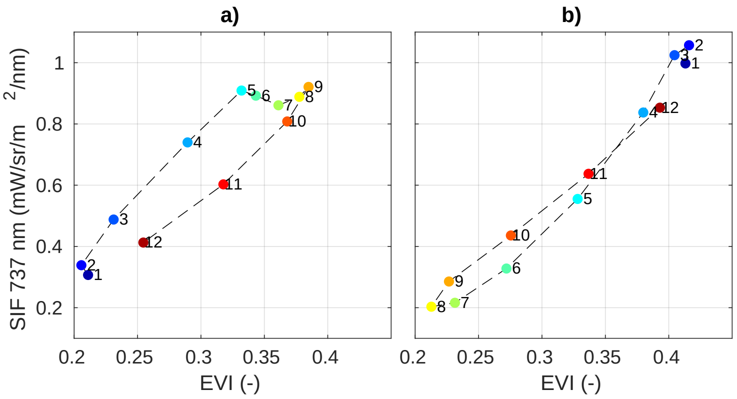

FIGURE 4.5: Seasonal values SIF verses EVI as a response of C3 grass and shrub vegetation types of Africa a) Northern of the equator and b) South of the equator.

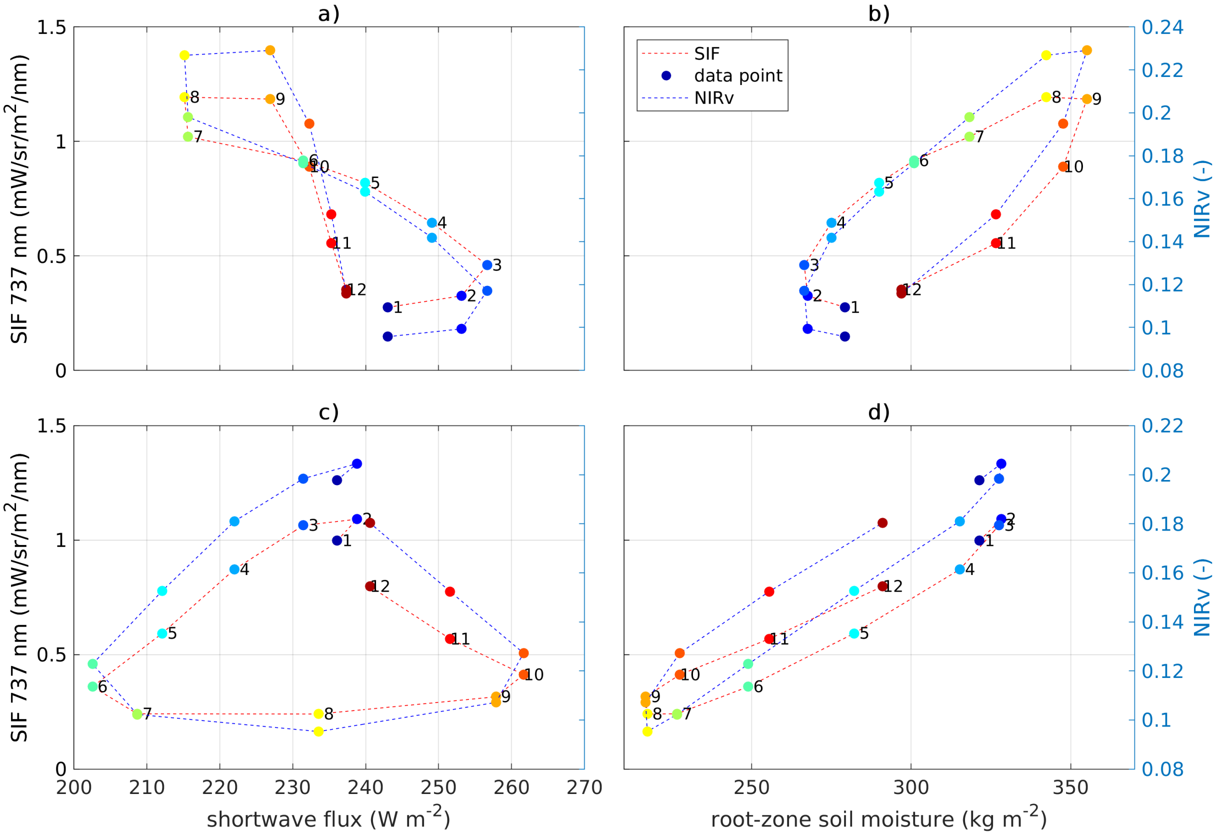

FIGURE 4.6: Relation between SIF/NIRv with incoming downward shortwave radiation (left panels), root zone soil moisture (right panels) for major African biomes. Upper panels show results over the vegetated regions of Northern Africa (north of the equator) while the bottom shows the results for Southern Africa (south of the equator). The numbers in the plot, and the colour of the markers, refer to the month of the year.

at the same soil moisture levels past the peak productivity.

Our analysis showed the availability of soil moisture strongly controls plant productivity. SIF and NIRv have a more strong correlation coefficient of R ≈ 0.97 with soil moisture over Southern Africa than Northern Africa (R ≈ 0.76).

4.3.3 SIF-GPP/NIRv-GPP Estimation for the Major Biomes

A SIF or NIRv based GPP estimate across each biome compares independently quite well to MPI-BGC estimated GPP. Figure 4.7 shows the GPP estimated by applying the SIF/NIRV-vs-GPP relation derived at EC-sites to biome-wide

TABLE 4.1: Linear regression results for NIRv and SIF with MPI-BGC GPP from Beer et al. (2010) over major biomes of Africa. y is the GPP inferred from NIRv/SIF and x is the NIRv/SIF signal. R is the spatial correlation coefficient between these signals and MPI-BGC GPP. n refers to the number of data points used in the regression analysis.

Biome	MPI-BGC GPP ($\frac{Kg\ C}{m^2 yr}$) & NIRv fitting equation	R^2	MPI-BGC GPP & SIF ($\frac{n\ W}{srm^2\ nm}$) fitting equation	R^2	n
Broad leaf evergreen Forest	y = 9.06*x + 0.51	0.38	y = 1.07*x +1.58	0.16	574
C3 grass	y = 10.33*x - 0.24	0.86	y = 1.92*x + 0.10	0.77	480
Shrub Northern Africa	y = 10.97*x - 0.41	0.98	y = 1.91*x - 0.03	0.92	265
Shrub Southern Africa	y = 13.55*x - 0.62	0.96	y = 2.51*x - 0.10	0.83	325
C4 grass Northern Africa	y = 12.54*x - 0.73	0.88	y = 2.23*x - 0.54	0.86	1382
C4 grass Southern Africa	y = 13.79*x - 0.75	0.85	y = 2.55*x - 0.38	0.83	1108

satellite observations. We chose the relation between the remotely sensed reflectances and the EC-GPP from Senegal SN-Dhr, Congo CG-Tch, Sudan SD-Dem and ZA-Kru towers to estimate GPP of the Northern Shrub, the Southern shrub, C4-grass and C3-grass respectively to represent different biomes over the northern and southern Africa (Fig. 4.2 for the fitting equations applied). Due to the weak relationship between SIF/NIRv with Ghana GH-Ank GPP, a flux tower in the tropical rain forest of Africa with broadleaf evergreen vegetation, we used a linear relation between SIF/NIRv with EC GPP data from Brazil BR-Sa1 flux tower which is also in tropical rain forest region with broadleaf evergreen vegetation and shows a better relationship with these signals than the GH-Ank (Fig. 4.8). The good correspondence to MPI-BGC GPP partly results from the EC-sites being part of the training algorithm for that product (Jiang and Ryu, 2016), but we note that the spatiotemporal drivers in our product (SIF/NIRv) is much different from that in MPI-BGC (PAR, T, PFT, precip, ...). Mostly, it shows that a reasonable first estimate of spatiotemporal GPP patterns can be based on SIF and NIRv without the need for the more complex and data-intensive machine-learning approach. At least, it captures the large differences between the major biomes of Africa, allowing further study of their seasonal dynamics, drought response, and contribution to tropical GPP.

GPP estimation from SIF needs a more complicated modelling approach

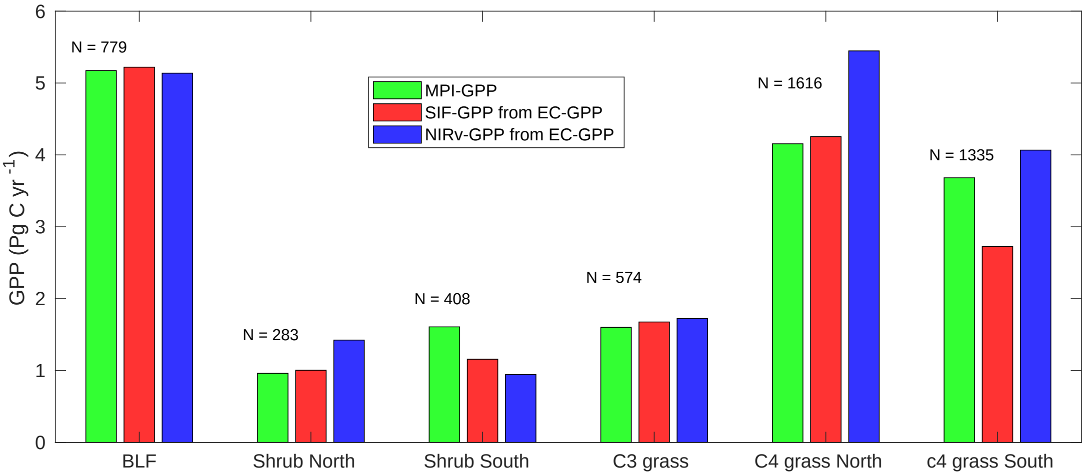

FIGURE 4.7: Comparison of aggregated MPI-BGC GPP, SIF-GPP and NIRv-GPP for major biomes in Africa. N is the number of grid box of size 0.5° × 0.5° used in the aggregation.

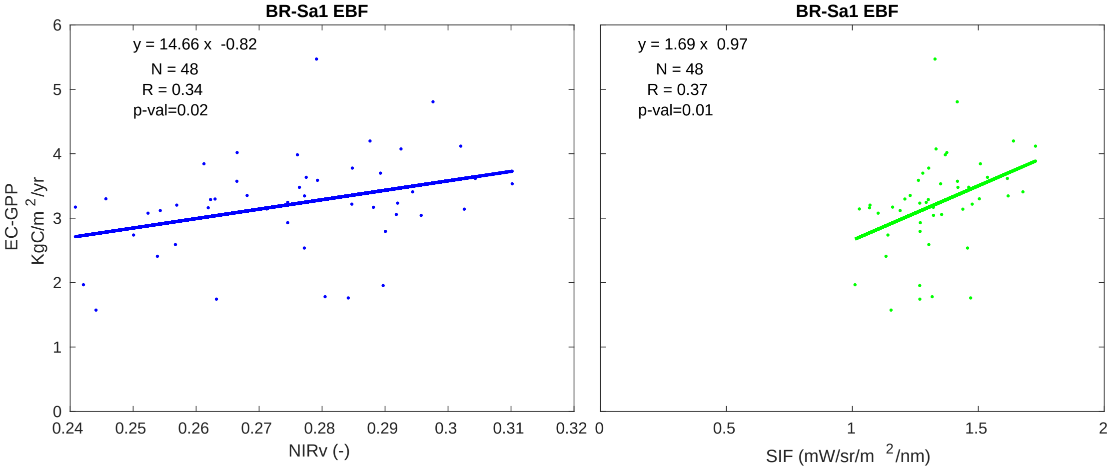

FIGURE 4.8: Comparison of eddy covariance GPP with NIRv and SIF around the Brazil BR-Sa1 flux tower. To obtain sufficient data the comparison is made by averaging monthly values within a 4° × 4° window enclosing the tower. Furthermore, to account for vegetation heterogeneity of the land, grid cells with a different vegetation type than for the tower location (evergreen broad-leaf forest) were masked. The regression slope and intercepts are used to infer GPP from NIRv and SIF over African broad-leaf evergreen forest.

(Norton et al., 2018; Anav et al., 2015) as it needs assimilation of SIF into a terrestrial biosphere model to estimate the gross uptake of carbon through photosynthesis. However, we applied a simple linear relation between SIF/NIRv and EC GPP and showed reasonably well estimates of GPP over different biomes (Fig.4.7) (see also Table 4.2 for biome specific estimation of GPP per unit area as a response of the major biomes of Africa). The GPP obtained using this simple upscaling method was integrated for each biome and found in good consistency with MPI-BGC GPP. SIF-GPP was found more consistent with MPI-BGC GPP than the NIRv-GPP. The NIRv-GPP upscaled was 31% higher than MPI-BGC GPP for C4 grass over Northern Africa. In contrast, it is lower by 42% for the shrub over Southern Africa. Guanter et al. (2014) investigated the global agricultural productivity and found that the MPI-BGC crop GPP estimations are 50-70% lower than the SIF-based GPP obtained by fitting to flux towers based GPP in the US and Europe crop and grasslands however in African grasslands. In contrast to this, we found that SIF-GPP is relatively lower than MIP-BGC GPP for the major biomes of Africa.

TABLE 4.2: comparison of biome specific estimates of five years mean GPP covering the period from 2007 to 2011 for major biomes of Africa as derived from: leaner regression of SIF/NIRv-vs-EC-GPP and Max-Planck Ensemble GPP (MPI-GPP).

Leave type	BLEF	Shrub NH	Shrub SH	C3 grass	C4 grass NH	C4 grass SH
SIF-GPP ($Kg\ Cm^{-2}yr^{-1}$)	2.52	1.34	0.90	1.15	1.04	0.82
NIRv-GPP ($Kg\ Cm^{-2}yr^{-1}$)	2.53	1.81	0.3	1.18	1.33	1.26
MPI-GPP ($Kg\ Cm^{-2}yr^{-1}$)	2.44	1.24	1.19	1.10	1.01	1.15

Fig. 4.9 shows the amplitude of the seasonal cycle of GPP derived from SIF and NIRv signals using the linear relation between SIF/NIRv-versus-MPI-BGC GPP over each biome. The predicted GPP from SIF and NIRv effectively tracked the magnitude and seasonal dynamics of the tower GPP. Seasonality of GPP well captures the beginning period, thriving period and the end period of the growing season. Weak correlation between the predicted and tower GPP was observed over the site in Ghana (see Fig. 4.9 GH-Ank BLF) with broadleaf evergreen vegetation type. This discrepancy is largely due to the vegetation mask we use has poor resolution near the cost and also retrieval of satellite products will be influenced by ocean pixel value during the process of aggregation. This suggests that satellite retrievals near the coast need much improvement. SIF-GPP shows a better sensitivity in capturing FLUXNET2015 GPP over Sudan and Senegal during wet months when GPP is maximum. In contrast, NIRv-GPP shows better sensitivity during dry months when GPP is minimum. SIF-GPP remains near zero throughout the non-growing season and starts to increases in response to enhanced photosynthesis during the growing season. In agreement with our hypothesis that, the Max-plank institute GPP estimation also suffers from large uncertainties in Africa as there are a very sparse flux tower measurements to be included.

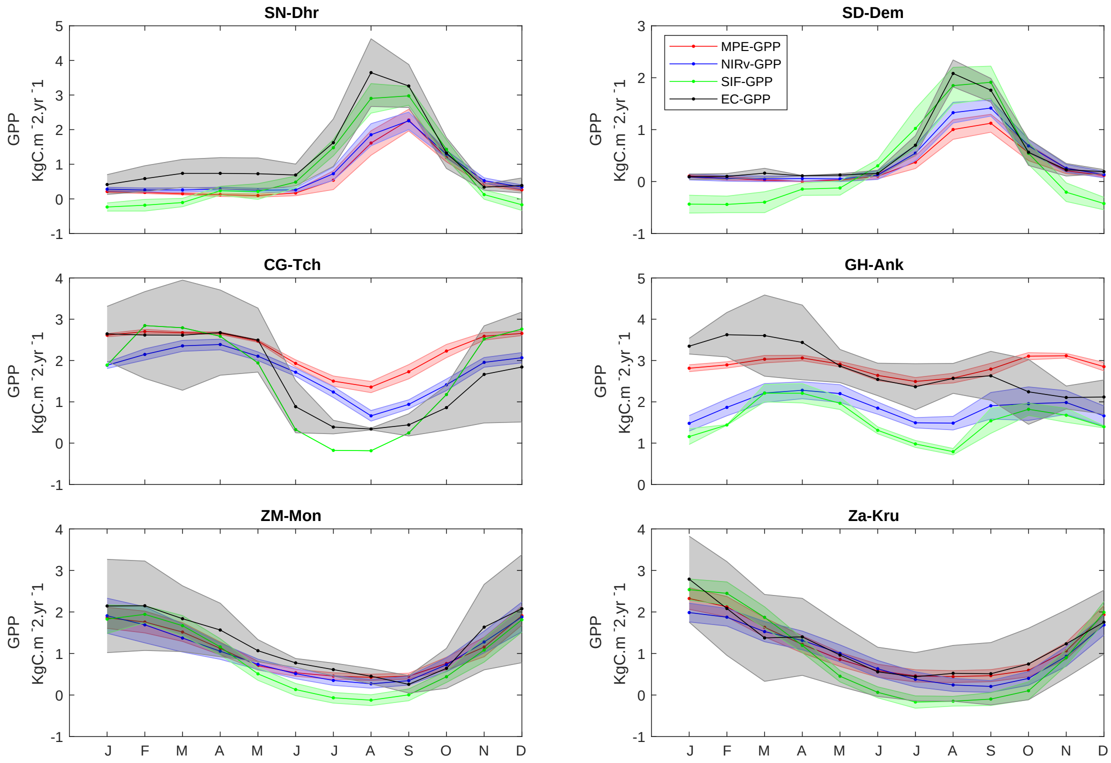

FIGURE 4.9: Seasonal cycles of GPP derived from FLUXNET2015 GPP (black), SIF-GPP (green), NIRv-GPP (blue) and MPI-BGC GPP (red) averaged for the available months of the flux site. Flux tower site IDs are indicated as a title over each box. Shaded areas are the standard deviations of the monthly means.

4.4 Summary

We investigated that Sun-Induced Fluorescence and Near-Infrared reflectance of vegetation can effectively track the seasonal dynamics of gross primary production for major biomes. The large uncertainties in the carbon cycle are from a poor estimation of the land-use change associated with the growing and end-growing periods of vegetation. SIF and NIRv can also effectively track the seasonality of GPP derived from six eddy covariance flux towers in Africa. Resulting in correlation coefficients of > 0.9 over savannas in the northern and southern hemispheres. These coefficients are slightly higher than the widely used MPI-BGC GPP products and Enhanced Vegetation Index (EVI). Unlike the GPP estimation from vegetation index, GPP derived from these two remotely sensed vegetation reflectances does not show saturation at maximum productivity. SIF and NIRv are strongly controlled by the amount of soil moisture during a thriving and end-growing seasons of vegetation, while during the extremely dry and wet seasons the amount of shortwave radiation strongly controls vegetation productivity.

Chapter 5

Trends, periodicity and associated drivers of natural carbon dioxide flux over tropical Africa land mass

5.1 Background

Correlations between ENSO events and atmospheric CO_2 concentrations have been studied since the 1970s (Chatterjee et al., 2017). The long-term CO_2 record from the Mauna Loa Observatory, Hawaii, shows a noticeable seasonal cycle and interannual fluctuation (Keeling et al., 1976; Keeling et al., 1995). The atmospheric annual growth rate of CO_2 significantly increases during El Niño, and decreases during La Niña event (Bousquet et al., 2000; Keeling and Revelle, 1985). Wang, Zeng, and Wang (2016) depicted that Mauna Loa atmospheric CO_2 annual growth rate leads temperature by 1 month with a correlation of (0.77); lags precipitation by 4 months with a good correlation of -0.63 and with no lags and a correlation of 0.65 with soil moisture. Previous studies from in situ observations and terrestrial carbon cycle models suggest that temperature has major influences on plant respiration and photosynthesis. Thus, El Niño induced temperature rise can be considered as the dominant factor responsible for atmospheric carbon annual fluctuation (Wang et al., 2014; Wang et al., 2013; Clark et al., 2003; Cox et al., 2013a; Piao et al., 2013). In addition, the microbial decomposition, which increases exponentially with warming temperature, accounts for the significant positive correlation between the tropical temperature and atmospheric CO_2 annual growth rate (Wang et al., 2013; Wang et al., 2014). Wang et al. (2014) also noted a two-fold increase in the sensitivity of annual CO_2 growth rate in response to the tropical temperature change in the past 5 decades. In addition, Enhanced Vegetation Index (EVI), which provides an indirect estimate of the vegetation photosynthetic activity (Tucker, 1979), is closely related to rainfall and soil moisture availability (Camberlin, 1995; Martiny et al., 2006, and references therein). As a result, it is an indicator of the global and regional carbon budget. Therefore, an understanding of the spatiotemporal ecosystem dynamics together with its relation to meteorological variables during ENSO events is paramount to quantify the sensitivity of the carbon cycle to climate variability.

In particular, this chapter aims to identify and discuss the response of terrestrial-atmospheric exchange of CO_2 flux at various localities over tropical Africa in relation to ENSO events. It also tries to identify the main drivers responsible for the observed fluctuation. Concurrent and lag correlations of temperature, precipitation, soil moisture, EVI and Niño 3.4 indices with CO_2 flux over Equatorial Africa landmass covering the period from 2000 to 2016 at the pixel scale are analyzed. The study also investigates the carbon dioxide stock of different subregions of equatorial Africa during the strongest El Niño event together with the most probable driver.

5.2 Analysis methods

Ensemble empirical mode decomposition (EEMD) is a statistical tool that decomposes the time series into different signal components without leaving the time domain. The method is useful for analyzing natural signals which are non-linear and non-stationary. EEMD filters out a function (Intrinsic Mode Functions, IMFs) from a completely and nearly orthogonal basis for the original signal. These IMFs are sufficient to describe the signal, even though they are not necessarily orthogonal (Wu and Huang, 2009; Huang and Wu, 2008). IMFs obtained from the EEMD decomposition of real-world time series signals is quite important because natural processes often have multiple causes, and each of these causes may happen at specific time intervals. Such causes can be captured in EEMD analysis, but it is hardly possible in other methods such as Fourier decomposition or in wavelet analysis. In this chapter, an EEMD method was applied to decompose CO_2, temperature, precipitation and root zone soil moisture time series signals over tropical Africa covering the period from January 2000 to December 2016. The EEMD was applied on the monthly time series of each variable to obtain fluctuations at seasonal, interannual and decadal time scales at each grid point. The grid points were selected based on the resolution of CT2017-flux products, which is in 1^0X1^0 resolution. In the EEMD method, a time series x(t) is decomposed into adaptively obtained, amplitude-frequency modulated oscillatory components or Impirical Mode Fluctuation (IMF) and a residual lowest frequency IMF component (RES) which represents the overall general trend of the original signal. For a given signal x(t), local maxima/minima of x(t) were identified and then, all local maxima/minima are connected by a cubic spline to form the upper/lower envelope (Huang et al., 1998). The mean value of the upper and the lower envelopes, $m_1(t)$, is subtracted from the original time series, x(t), and denoted as $h_1(t)$, i.e.,

$$h_1(t) = x(t) - m_1(t) \tag{5.1}$$

where, $h_1(t)$ could be the first IMF, if the number of extremes is equal to the number of zero-crossings or at most differ by one and the mean value of the two envelopes determined by the local maxima and minima equal to zero (Huang et al., 1998). However, if $h_1(t)$ does not satisfy these conditions, the the sifting process will be repeated using $h_1(t)$ as the new data, such that

$$h_{11}(t) = h_1(t) - m_{11}(t) \tag{5.2}$$

where $m_{11}(t)$ is the mean of the envelopes with $h_1(t)$ replacing the data x(t) in the first iteration. This process is repeated up to k=1000 times:

$$h_{1k}(t) = h_{1(k-1)}(t) - m_{1k}(t) \tag{5.3}$$

IMF becomes a constant-amplitude frequency-modulated function as the sifting process is repeated sufficiently too many times, which possibly guaranteed that, the IMF retains enough physical sense of both amplitude and frequency modulations (Huang et al., 1998; Huang et al., 2003). This can be accomplished by limiting the size of the standard deviation, SD, computed from the two consecutive sifting results as (Huang et al., 1998)

$$SD = \sum_{t=0}^{T}[\frac{|(h_{1(k-1)(t)-h_{1k}(t)})|^2}{h^2_{1(k-1)}(t)}] \tag{5.4}$$

The first IMF is obtained when SD is smaller than the defined threshold:

$$c_1(t) = h_{1k}(t) \tag{5.5}$$

$c_1(t)$ contains the finest scale component of the signal. The residue $r_1(t)$ is calculated as

$$r_1(t) = x(t) - c_1(t) \tag{5.6}$$

then, residue $r_1(t)$ treated as the signal to be decomposed and the above steps are repeated to obtain $c_2(t)$, $c_3(t)$, . . . , $c_n(t)$. The procedure stops when the residue $r_n(t)$ becomes a monotonic function from which no more IMF can be extracted (Huang et al., 1998). After the sifting process is completed, the original signal can be reconstructed from the sum of the IMFs and the final residue as

$$x(t) = \sum_{i=1}^{n} c_i(t) + r_n(t) \tag{5.7}$$

c_i(i = 1, 2,. . . , n) is the ith IMF component and a residual r_n which is a curve that is either monotonic or contains only one extreme from which no additional oscillatory components can be extracted.

To see whether an IMF for EEMD contains a true signal or just a random noise component, the Monte-Carlo method was used to perform a significance test (Wu and Huang, 2005; Wu and Huang, 2004). The statistical significance test for IMF components derived from white noise was established by Wu and Huang 2005; 2004. The true signals were determined by examining the more detailed distribution of the energy with respect to the period in the form of spectral function. The energy density of the i^{th} IMF component (E_i) defined as follows (Wu and Huang, 2009)

$$E_i = \frac{1}{N} \sum_{t=1}^{N} |c_i(t)|^2 \tag{5.8}$$

where N is the length of the IMF component and $c_i(t)$ denotes the i^{th} IMF component. There exists a simple equation that relates the energy density and the mean oscillation period (T_i) (Wu and Huang, 2009):

$$\ln E_i + \ln T_i = 0 \tag{5.9}$$

If the IMF energy of the climate signal with a certain mean period exceeds the upper limit of a certain confidence interval, we assume that the corresponding IMF contains statistically significant information at that selected confidence level (e.g., 95%, 90%, 50%).

Variance contribution rate (VCR) explains the aggregate impact of frequency and amplitude at different time scales on the overall characteristics of the original signal. The VCR of the i$_t h$ IMF component (VCR_i) is calculated as:

$$VCR_i = \frac{var(c_i(t))}{\sum_{i=1}^{i=n} var(c_i(t)) + var(r_n(t))} \times 100\% \tag{5.10}$$

where $var(c_i(t))$ and $var(r_n(t))$ represents the variance of the ith IMF component and the final residue respectively.

The decomposed signals of CO_2, temperature, precipitation, root zone soil moisture and EVI were correlated to Niño 3.4 index at seasonal and inter-annual scale. Based on the climatology and vegetation types we investigate six regions as shown in the map depicted in Fig. 2.1c.

5.3 Spatiotemporal variability of CO_2

5.3.1 CO_2 Periodicity over tropical Africa

EEMD was applied on CT2017-flux time-series signal. The result implies that CO_2 flux has six periodicities over tropical Africa. Fig. 5.1 shows the time series of CO_2 (Original data, upper row), the six IMF components (IMF1-6, middle rows) and the overall adaptive trend component (Trend, last row) averaged over tropical Africa covering the period from January 2000 to December 2016. The fluctuation characteristics from high frequency to low frequency at different time scales are reflected in each IMF component. The first IMF (IMF1) contains the highest frequency and this frequency decreases as the index i of IMFi increases. The trend represents the lowest frequency of the original signal. Moreover, each IMF has its physical meaning, which is associated with the driver that causes the fluctuation (Huang et al., 1998).

TABLE 5.1: Mean periodicity of each IMF in the natural CO_2 flux and the associated contribution rate for the variation in the total natural CO_2 flux during 2000 - 2016 in tropical Africa.

IMF components	IMF1	IMF2	IMF3	IMF4	IMF5	IMF6	Trend
Period (month)	3.26	6.48	12.36	24.00	58.29	102.00	-
variance (%)	50.60	22.94	17.91	5.05	1.88	0.28	1.35
Pearson correlation	0.77	0.51	0.20	0.13	0.03	0.05	0.09

IMF components contain the periodic changes of climatic systems under external forces, as well as nonlinear feedback. CO_2 flux from 2000 to 2016 in tropical Africa has quasi-3 months (IMF1) and quasi-6 months (IMF2) and quasi-1 year (IMF3) variability. In addition, it has also quasi-2 years (IMF4) and quasi-4 years (IMF5) at the inter-annual scale and quasi-8.5 years (IMF6) at the decadal scale (see Table 5.1). The variance contribution illustrates the effect of the signal fluctuation frequency and amplitude at each scale on the general characteristics of the available raw data. The variance contribution of each component to CO_2 flux is depicted in Table 5.1. IMF1 explains 50.6% of the total CO_2 variance and as a result, strongly correlates (0.77) with CO_2 flux. In addition, IMF2 and IMF3 explain 22.94% and 17.91% of the total natural CO_2 flux variance respectively.

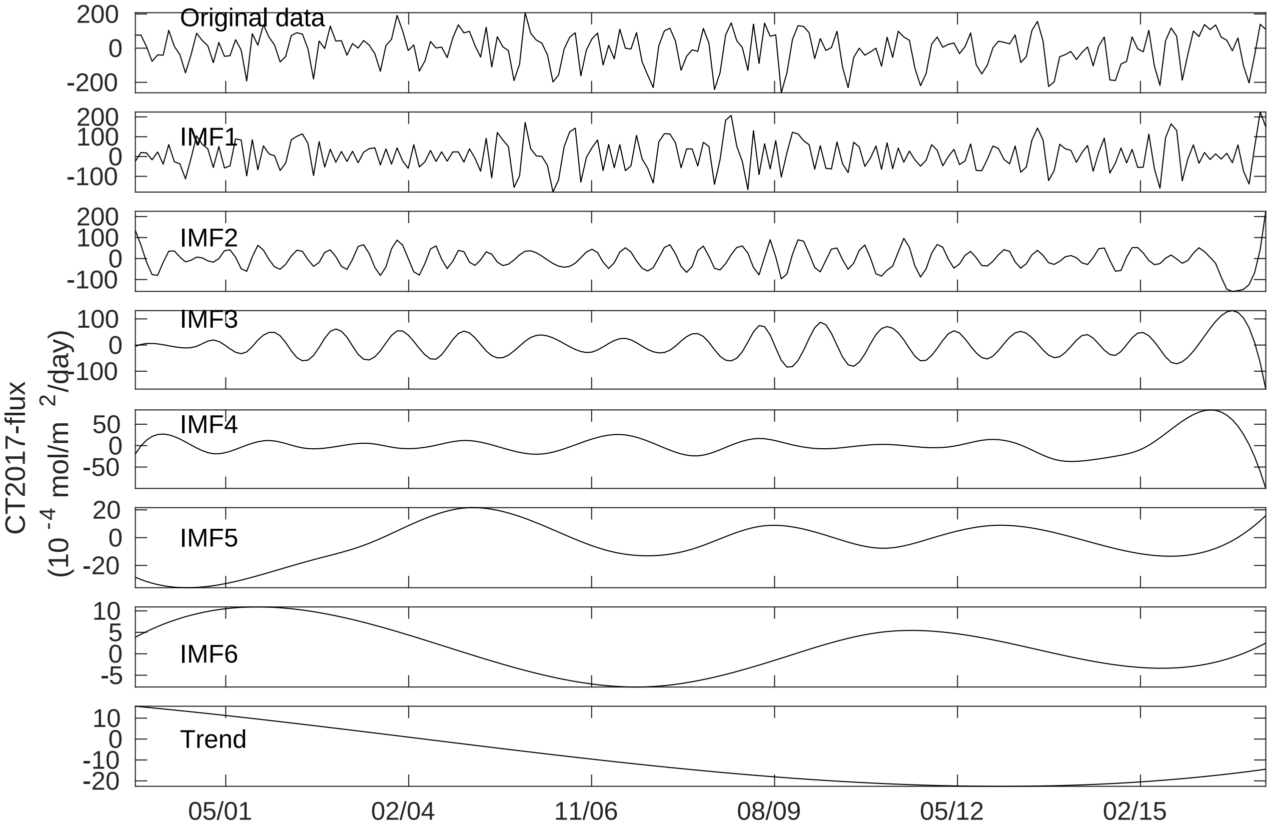

FIGURE 5.1: Ensemble empirical mode decomposition of CT2017-flux at seasonal (IMF1-IMF3), inter-annual (IMF4 and IMF5), and inter-decadal (IMF6 and Trend) scale covering the period from 2000 to 2016 in tropical Africa. A negative value implies that the biosphere is a sink of CO_2.

Therefore, CO_2 fluctuation at a seasonal scale contributes 91.41% of the total variance of natural CO_2 flux. On the other hand, more than 8.56% of the natural CO_2 flux fluctuation is associated with interannual and long-term drivers. Specifically, the quasi-2 years (IMF4) and quasi-5 years (IMF5) explain 5.05% and 1.88% of the total variance of the observed natural CO_2 flux respectively. The CO_2 variability at these time scales is associated with the ENSO cycle. In addition, IMF6 contributes 0.28% of the CO_2 variance at quasi-8 years, which has an association with Pacific Decadal Oscillation (PDO).

Fig. 5.2 shows the spatial distribution of periodicities of each IMFs in the natural CO_2 flux averaged from 200-2016 and the variance contribution rate of each IMFs to the original flux. The variance contribution of each IMF to the total natural CO_2 flux shows a significant variation from region-to-region. For example, quasi-3, quasi-6 quasi-12 months fluctuation has a strong contribution over the tropical rainforest, tropical Southern Savanna, tropical Northern Savanna.

Fig. 5.3 shows the statistical significance of each CO_2 flux IMFs averaged over the region. IMFs corresponding to seasonal variability (IMF1, IMF2 and

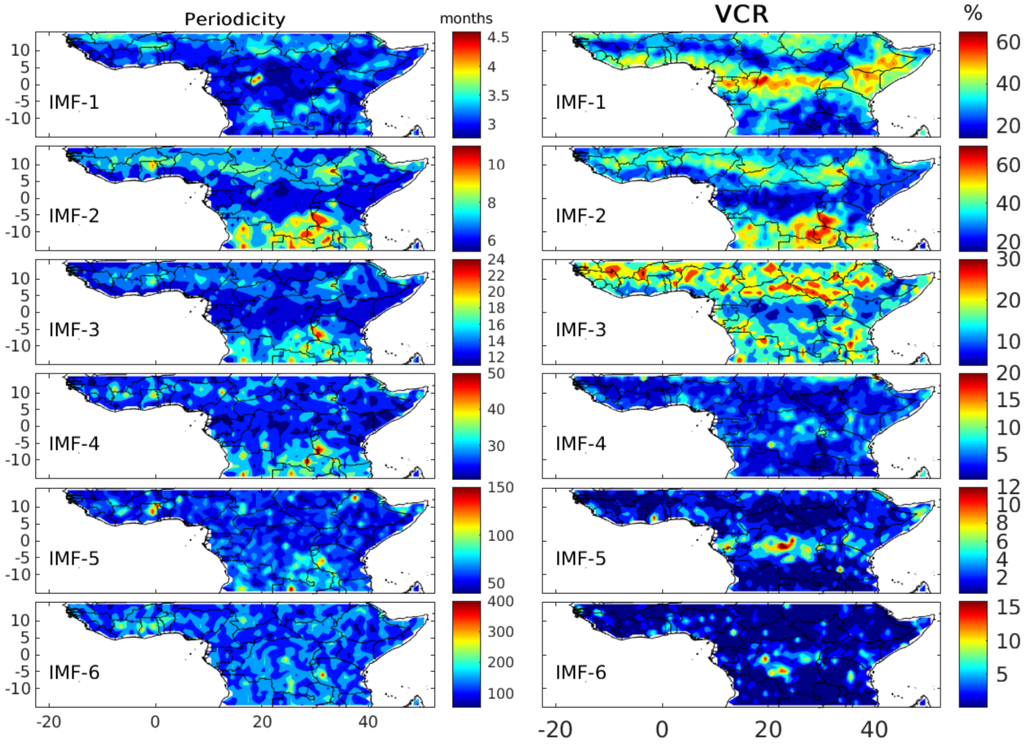

FIGURE 5.2: Spatial distribution of periodicity for each IMF in the natural CO_2 flux (Periodicity) and the associated variance contribution rate (VCR) covering the period from 2000 to 2016 at a resolution of $1^0 X 1^0$.

IMF3) are significant at the 95% confidence level, implying that these components are highly significant and have strong physical driver/s responsible for the fluctuation (Wu and Huang, 2005). In contrast, IMFs with periodicity in the range of interannual fluctuations were found to be significant at about 50% confidence interval, suggesting that they contained less information with the actual physical meaning. At the subregional scale, Fig. 5.4 shows that IMFs of CO_2 flux corresponding to interannual fluctuations are significant at the 95% confidence interval over Western tropical Africa (Fig. 5.4a) and Tropical East Africa (Fig. 5.4f), indicating the presence of strong drivers of CO_2 flux over these regions both at quasi-2 and quasi-5 years. In contrast, these IMFs are significance at the 50% level in tropical North Africa (Fig. 5.4b). IMF2, IMF3, IMF4 and IMF6 over rainforest (Fig. 5.4d) are significant at a confidence level of 50%. In contrast, IMF1 and IMF5 are significant at the 95% level, implying that strong seasonal and interannual CO_2 variability associated with quasi-3 month and quasi-5 year periodicity respectively in tropical rainforest Africa. Ethiopian highlands and

Tropical South Africa (Figs. 5.4c and 5.4e) are found to have a strong atmospheric, surface and oceanic drivers at seasonal and quasi-5 year time scales.

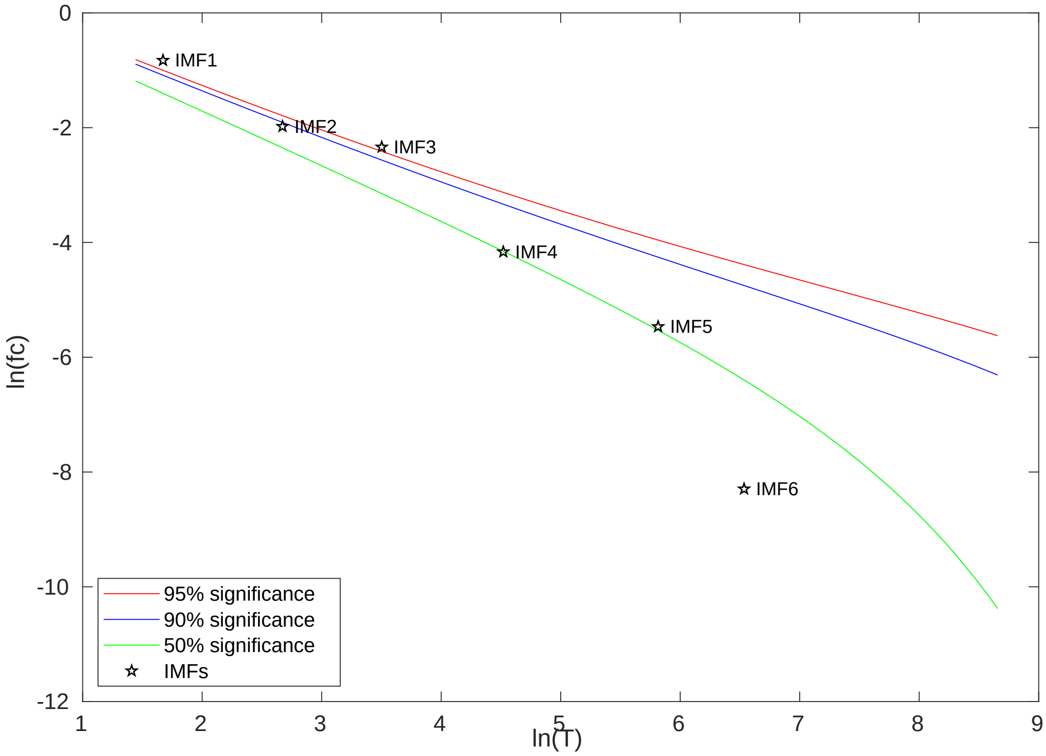

FIGURE 5.3: Statistical significance of each IMFs averaged over tropical Africa. The results were computed as the natural logarithm of CO_2 flux (fc) versus the natural logarithm of the mean period in months (T) for each IMFs.

5.3.2 Trends and variability of CO_2 flux

Fig. 5.5 depicts the time series of seasonal (which is the sum of IMF1, IMF2, IMF3, and the trend component) fluctuation, interannual (which is the sum of IMF4, IMF5, IMF6, and the trend component) fluctuation, and the overall adaptive trend in comparison to the original CO_2 flux. The reconstructed seasonal variation of CO_2 flux was almost consistent with the fluctuations of the original CO_2 flux during the study period. The interannual variability shows anomalously high variability with peaks above the trend line during El Niño years (e.g., during the 2004, 2006, 2009, 2012 and 2015-2016 El Niño years). The strongest interannual CO_2 fluctuation was found in conjunction with the 2015-2016 El Niño event, which is the strongest El Niño event since 2000 (Pumphrey et al., 2018). Reduced biosphere uptake during dry and warm seasons results in an increase of atmospheric CO_2. On the other hand, anomalously low interannual variability was observed during La Niña years (e.g., during the 2001,

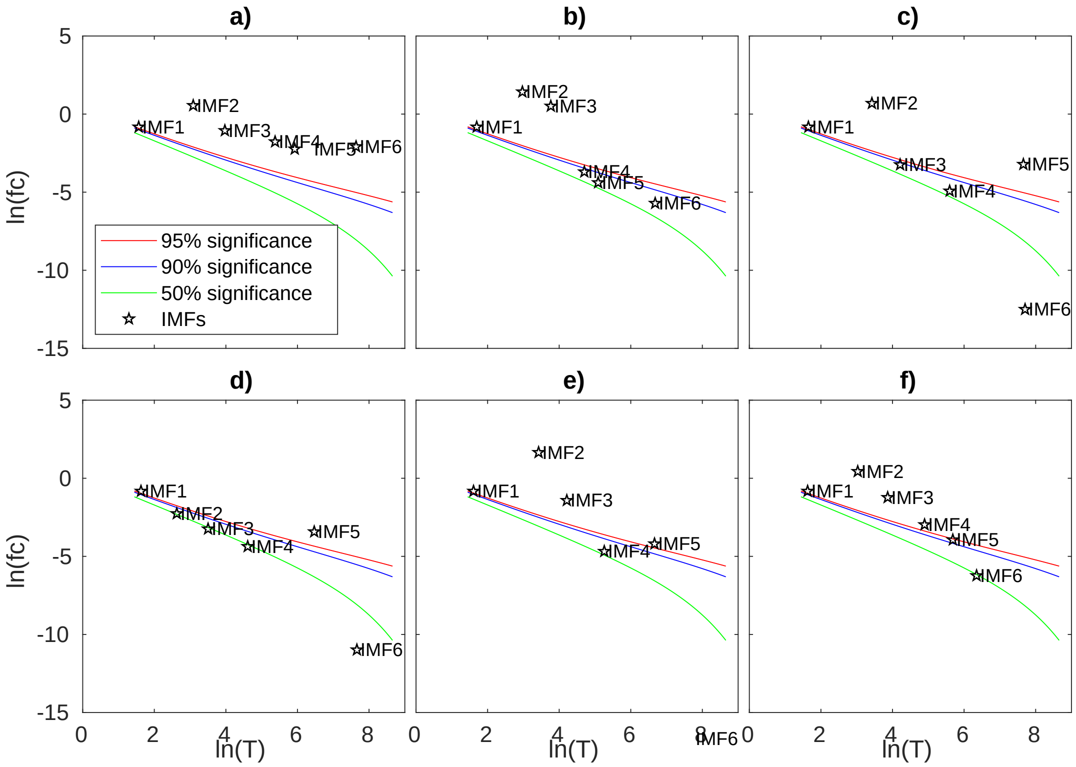

FIGURE 5.4: Statistical significance of each IMFs averaged over subregions tropical Africa. a) tropical Western Africa, b) Tropical North Africa, c) Ethiopian Highlands , d) tropical rainforest, e) tropical Southern Africa and f) Tropical East Africa F).

2008 and 2014 La Niña years). The results suggest that the terrestrial CO_2 sink is weak during El Niño years. In addition to interannual and multi-decadal variability, there was an overall nonlinear downward trend in natural CO_2 flux over tropical Africa, covering the period from 2000 to 2016. Previous studies have shown that CO_2 levels in other regions have also experienced complex and nonlinear processes (Good et al., 2015; Jia et al., 2017), indicating that the nonlinear process of CO_2 is a global issue. Fig. 5.5 shows a decreasing trend up until 2013 and starts to increase afterwards, suggesting that, in recent years the carbon uptake has decreased and/or emissions from fires have increased over the region.

At a subregional scale, natural CO_2 flux shows an increasing trend over Western tropical Africa (see Fig. 5.6a) and Ethiopian highlands (see Fig. 5.6c), indicating a reduced CO_2 sink and/or increased CO_2 emission from a forest fire. The growing population and industrialization together with the variability of climate and land-use change contribute to the rising of atmospheric CO_2 emissions and reduced CO_2 uptake by the terrestrial vegetation (Mengistu and Mengistu Tsidu, 2018; Ciais et al., 2011; Williams et al., 2007, and references therein). On the other hand, Fig. 5.6b shows a decreasing trend in the natural

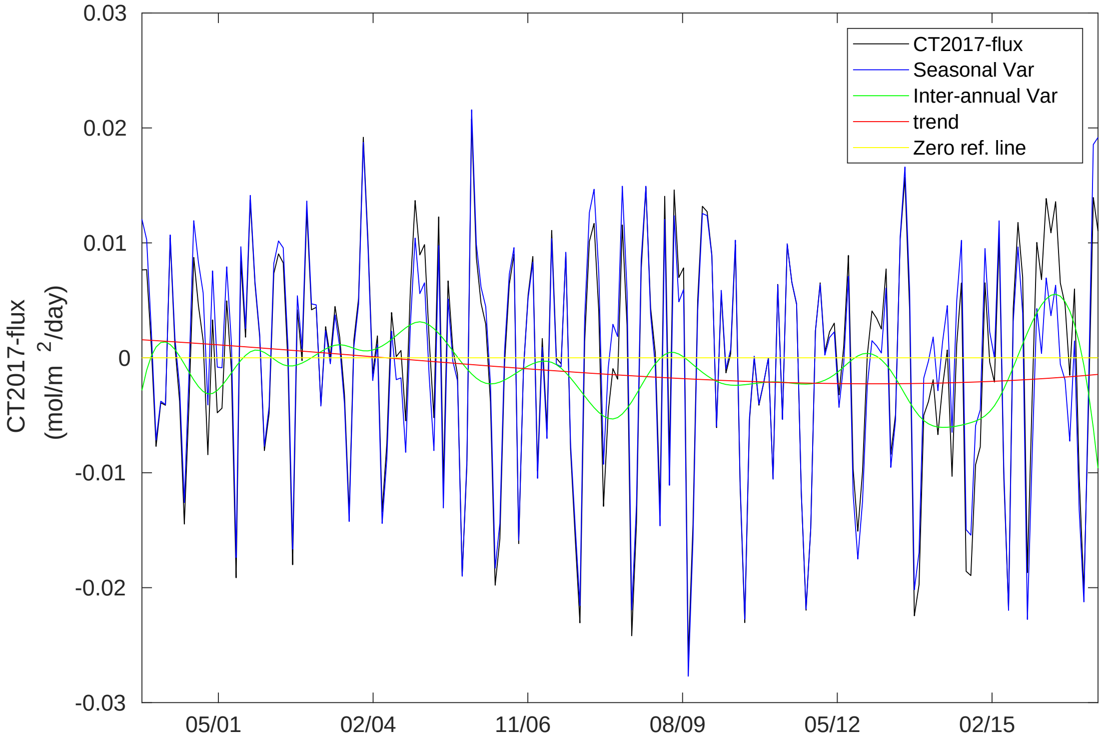

FIGURE 5.5: Time series of total natural CT2017-flux (black line), seasonal variability (blue line), interannual variability (green line) and the trend component (red line) during 2000-2016 over tropical Africa.

CO_2 flux over tropical Northern Africa, implying a growing terrestrial CO_2 sink over the region. Canadell, Raupach, and Houghton (2009) also found a recent plantation, which exceeds deforestation, resulting in a net flux of carbon sink over North Africa.

5.3.3 Seasonal variability of natural CO_2 flux with temperature, precipitation, soil moisture and EVI

Fig. 5.7 depicts a negative correlation between natural CO_2 flux and precipitation, root zone soil moisture and EVI whereas it shows a positive correlation with temperature over most regions in tropical Africa. This is a consequence of the terrestrial carbon sink increase with increasing precipitation and decreasing temperature (Wang et al., 2018). Hence, spring and summer are the growing seasons for plants, including trees, grass, flowers, etc. which leads to an enhanced photosynthesis activity whereby the plant extracts carbon dioxide from the atmosphere. In contrast, during winter, reduced photosynthesis activity, enhanced forest fire, and soil decomposition result in the emission of CO_2 to the atmosphere. In addition, plants like grasses die and decomposed during the

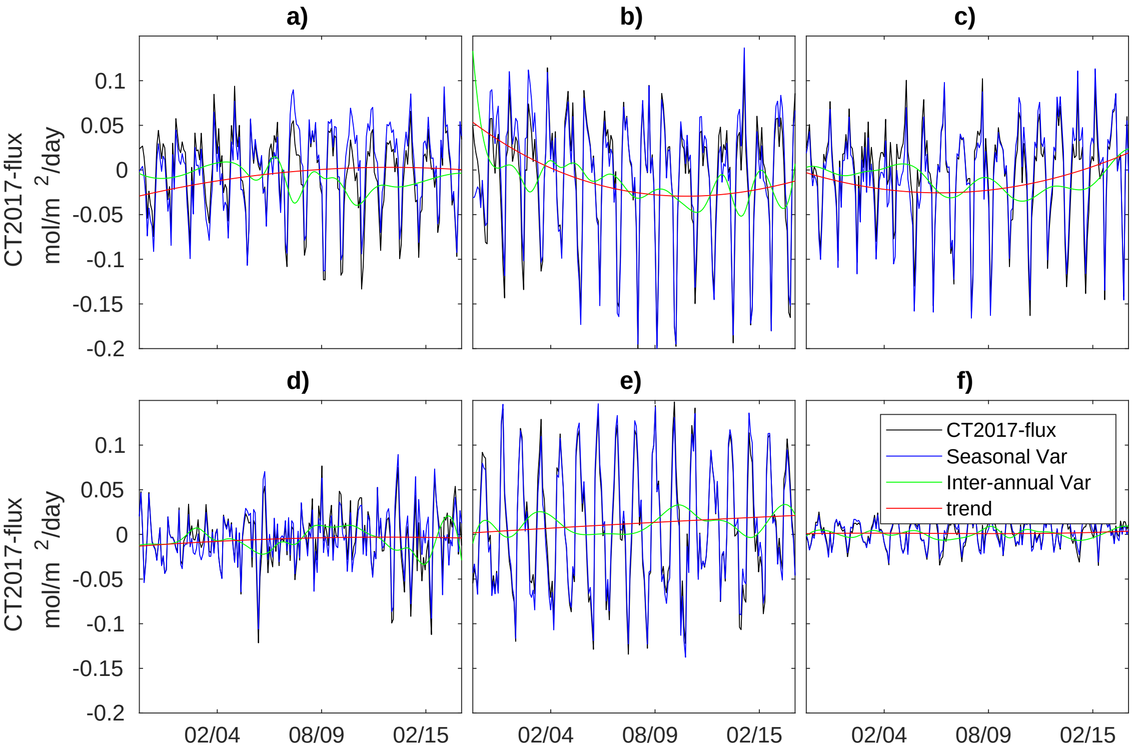

FIGURE 5.6: The same as Fig. 5.5 but over a) tropical Western Africa, b) Tropical North Africa, c) Ethiopian Highlands , d) tropical rainforest, e) tropical Southern Africa and f) Tropical East Africa.

colder months, resulting in more CO_2 release to the atmosphere (Tsutsumi et al., 2006).

Fig. 5.7 also shows a stronger correlation over grassland regions than over tropical rainforest regions. On the other hand, there is a positive correlation between the natural CO_2 flux and precipitation over East Africa (e.g., Eastern Ethiopia, Somalia and Kenya), indicating that the terrestrial carbon sink decreased with increasing precipitation. Moreover, in tropical East Africa regions, temperature shows a negative correlation with natural CO_2 flux. This is most likely anticipated to warm and wet conditions in the region that enhances terrestrial respiration which exceeds photosynthesis. Nydahl, Panigrahi, and Wikner (2013) also noted that warmer and wetter climatic conditions enhance microbial activity. Indicating enhanced precipitation and a decrease in temperature will cause an increased CO_2 flux over Tropical Eastern Africa at a seasonal scale. However, the correlation with temperature is insignificant over most of Tropical East Africa regions, implying that precipitation plays the dominant role in CO_2 variability of the region at a seasonal scale. A positive/negative correlation of CO_2 flux with temperature/precipitation was observed over most tropical northern and southern Africa regions. This indicates that the rising

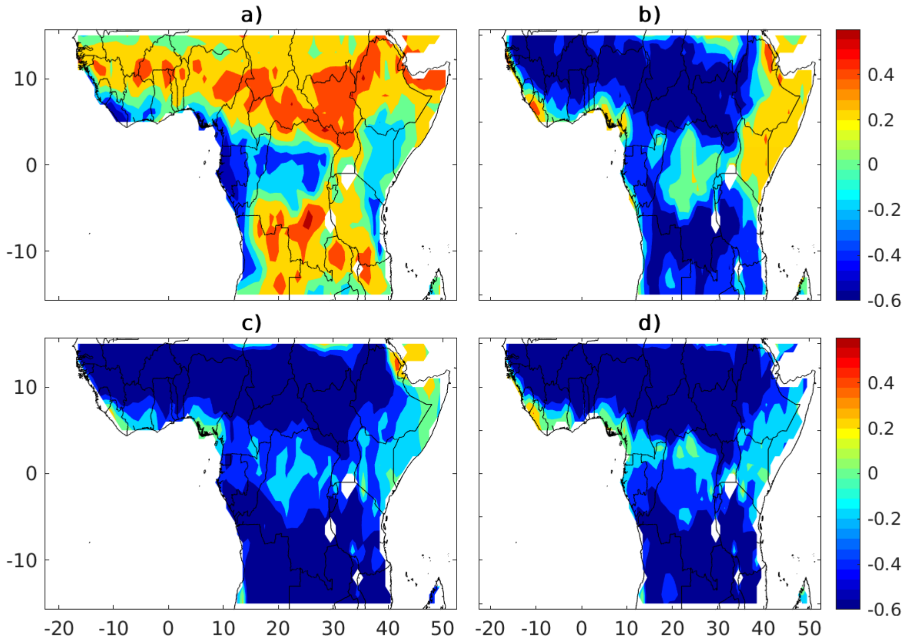

FIGURE 5.7: Correlation of seasonal fluctuation in the natural CO_2 flux with seasonal fluctuation of: a) Temperature, b) Precipitation, c) Root zone soil moisture and d) EVI.

in temperature and lowering in precipitation primarily results in an increased natural CO_2 flux over the region, i.e., the concentration of atmospheric CO_2 was higher during drier and warmer seasons. In contrast, both temperature and precipitation are found to have a negative correlation with natural CO_2 flux over the rainforest regions of tropical Africa, which suggests the rise in precipitation will favour vegetation growth and rising temperature will not enhance soil oxidation, as the soil is moist enough for reduced microbial activity. Therefore, precipitation will represent the dominant cause for the rising natural CO_2 flux over the tropical rainforest region at the seasonal scale.

5.3.4 Relation between Interannual natural CO_2 flux variability and ENSO events

Fig. 5.8 shows a correlation of interannual natural CO_2 flux with Niño 3.4 index (Fig. 5.8a) and the corresponding lag time in units of months (Fig. 5.8b). A positive correlation implies El Niño events are the most likely cause for the rising in atmospheric CO_2 flux over the region at the interannual scale. Whereas, a negative correlation indicates El Niña events are responsible for the lowering of atmospheric CO_2 flux due to increased terrestrial uptake and/or reduced emissions. Fig. 5.8a depicts a positive correlation between the natural CO_2 flux and Niño 3.4 index over most of the study area with a lag time ranging from 0 to 12 months (Fig. 5.8b). A strong correlation of up to 0.6 was found over regions like Benin, Nigeria, Chad, and Kenya and Tanzania. These regions are known to be the most vulnerable to El Niño induced drought. Ahlström et al. (2015) suggests that semi-arid ecosystems of low latitudes highly contribute to interannual CO_2 fluctuations. Moreover, the sensitivity of tropical North Africa to global SST anomalies was confirmed by earlier observations and modelling work (Giannini, Saravanan, and Chang, 2005). On the other hand, Fig. 5.8 also shows near-zero and negative correlation in regions like Central Africa, Ethiopian highlands, west and east coast of tropical Africa.

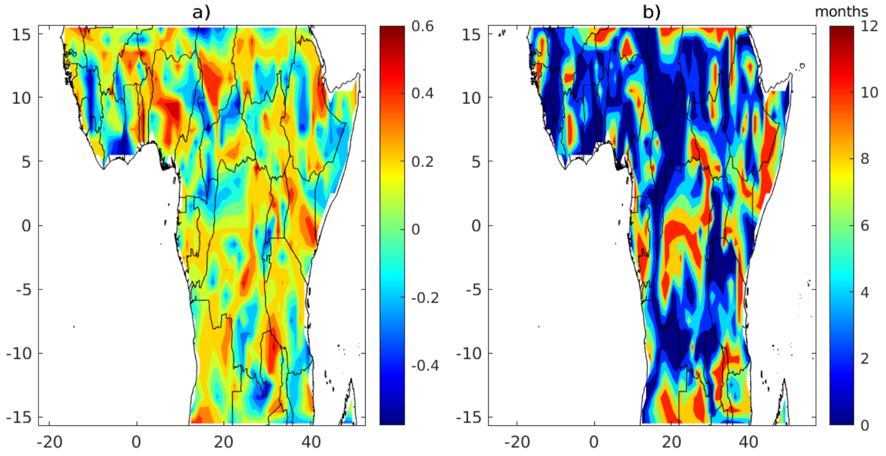

FIGURE 5.8: a) Correlation of interannual fluctuation in the natural CO_2 flux with Niño 3.4 index and b) the corresponding lag time in units of months over tropical Africa covering the period from January 2000 to December 2016.

TABLE 5.2: CO_2-flux balance of tropical Africa in units of $gCm^{-2}y^{-1}$. Carbon balance covering the period from 2000 to 2016 (17 years mean), during the strong El Niño event of 2015/16 (2015/16). Contribution from seasonal variability (CSV) and Contribution from interannual fluctuation (CIV).

Regions	**17 years mean**	**2015/16**	**CSV 17 years Mean**	**CSV 2015/16**	**CIV 17 years mean**	**CIV 2015/16**
Tropical West Africa	-64.76	4.60	-75.39	-80.60	3.84	94.17
Tropical Northern Africa	-156.90	-117.91	-150.05	-148.64	-8.09	26.87
Ethiopian Highlands	-64.89	113.98	-47.39	47.16	-2.69	54.41
Tropical Rain Forest	-64.23	-1.28	-61.62	-48.02	-15.76	76.24
Tropical South Africa	146.18	246.57	149.64	218.62	6.10	56.58
Tropical East Africa	28.91	80.21	28.38	47.95	-0.99	42.06
Horn of Africa	20.69	51.83	23.46	49.30	0.76	4.79
Tropical Africa	-7.01	29.12	-5.24	5.85	-2.46	29.81

The relation between interannual CO_2 flux variability and Niño 3.4 index associated with ENSO teleconnection like temperature, precipitation, root zone

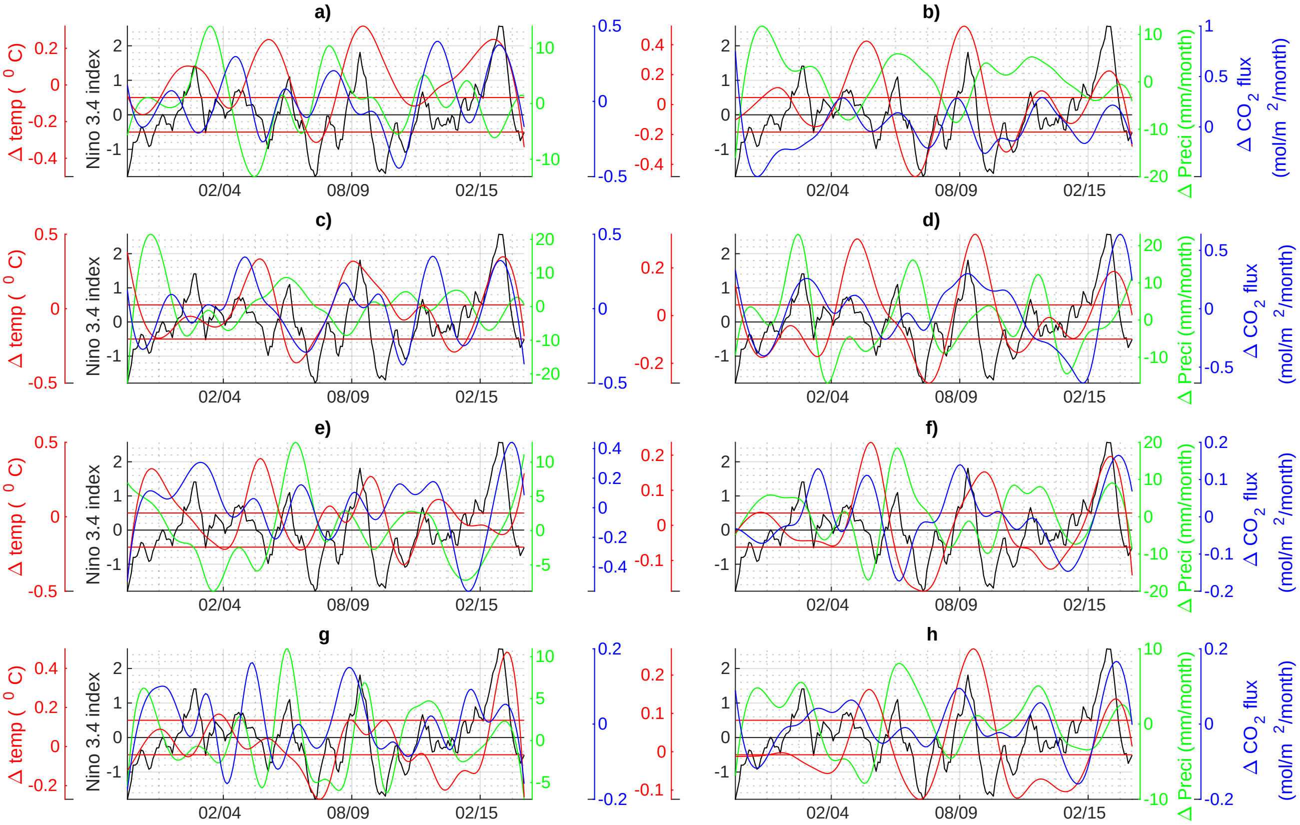

FIGURE 5.9: Time series of interannual variability of temperature (red line), Niño 3.4 index (black line), precipitation (green line), natural CO_2 flux (blue line) during 2000-2016 over a) tropical Western Africa, b) Tropical North Africa, c) Ethiopian Highlands , d) tropical rainforest, e) tropical Southern Africa and f) Tropical East Africa F).

soil moisture and vegetation cover of the region will provide information on the responsible drivers for the observed CO_2 flux. Fig. 5.9 shows a time series of interannual fluctuations of temperature, precipitation, natural CO_2 flux and Niño 3.4 index since 2000 in tropical Africa (Fig. 5.9h) and subregions of tropical Africa (Fig. 5.9a-g). Mostly, the temperature was found in-phase with Niño 3.4 index while precipitation is out-phase. Anomalously high atmospheric CO_2 flux was found in response to strong El Niño (Niño 3.4 index greater than 1.0) during 2009 and 2015/16 in most sub-regions of tropical Africa. Conversely, low CO_2 flux was observed in 2014. For example, during the strongest El Niño (2015/16) on average, the tropical Africa released about 0.2 mol/m^2 CO_2 flux per month to the atmosphere during the peak time. The strongest flux (0.5 $mol/m^2/month$) was released from a tropical rain forest. In addition, Ethiopian highlands and tropical Southern Africa also release 0.4 $mol/m^2/month$ CO_2 flux. However, the response of tropical northern Africa was found to be a net CO_2 flux sink and shows no CO_2 anomalous peak during the study period. Tropical rain forest regions and tropical East Africa experience warm and wet conditions during this strong El Niño. Hirons and Klingaman (2016) also noted that these regions were vulnerable to warm and wet conditions during this El Niño event. Therefore, the temperature was the dominant driver of the atmospheric CO_2 flux over the tropical rain forest and tropical East Africa at interannual scale. West Africa and the Ethiopian highlands have experienced warm and dry conditions during the 2009 and 2015/16 strong El Niño years indicating both temperature and precipitation were the dominant drivers for the observed high CO_2 flux in the regions. On the other hand, reduced precipitation during early 2015 most likely led to a rise in CO_2 flux over tropical southern Africa. Mean over the 17 years shows that tropical Africa can be considered as a net CO_2 flux sink (-7.02 $gC/m^2/year$). However, due to reduced biosphere uptake during El Niño years tropical Africa acts as a source of atmospheric CO_2. For example, tropical Africa releases 29.12 $gC/m^2/year$ which was almost comparable to the contribution of interannual fluctuation during these years (see Table 5.2). The highest contribution of interannual variability was from tropical West Africa (94.17 $gC/m^2/year$) and Tropical rain forest (76.24 $gC/m^2/year$) but annual average emission from this region was not significant (see Table 5.2). On the other hand, reduced CO_2 uptake at seasonal and interannual scale over Tropical South Africa, Ethiopian highlands and Tropical East Africa were the highest during the 2015/16 El Niño year. Using an approximate area of tropical Africa (16740777.41 km^2) 487.49 $Tg\ C\ y^{-1}$ was released from tropical Africa during the 2015/16 El Niño year, which was twice the carbon budget of Africa (240 $Tg\ C\ y^{-1}$) for the period from 2000 to 2005 from land-use change (Canadell, Raupach, and Houghton, 2009).

5.3.5 Influence of El Niño induced temperature on CO_2 flux fluctuation

Temperature signals of the region were decomposed into its seasonal and interannual variabilities using EEMD. Fig. 5.10 shows the correlation of interannual temperature fluctuation with Niño 3.4 index (Fig. 5.10a) and the corresponding lag time in units of months (Fig. 5.10c). The correlation of interannual fluctuations of temperature with CO_2 flux (Fig. 5.10b) and the corresponding lag time in units of months (Fig. 5.10d) are also depicted in Fig. 5.10. Following El Niño events heat from the ocean is redistributed and warming at the surface progressively extends to about $\pm 30^\circ$ latitude with lags of several months. Previous studies revealed that the global mean temperature lag Niño 3.4 by 4 (Trenberth et al., 2002) and more strong correlation was found at 7 months lag (Wigley, 2000). Therefore, in this study, a maximum of nine-month lag in temperature is allowed in finding the maximum correlation between interannual temperature fluctuation and Niño 3.4 index. A positive correlation ranging from 0.2- 0.6 was found in Western tropical Africa, Northern tropical Africa, and tropical rainforest regions. This positive correlation indicates El Niño is associated with above normal temperature in these regions. Moreover, a positive correlation between temperature and CO_2 flux was found over the tropical rainforest and Northern tropical Africa. Thus, the positive correlation of temperature with both Niño 3.4 index and CO_2 flux implies El Niño induced temperature change drives interannual CO_2 flux variability in the tropical rainforest and Northern tropical Africa. A significant positive correlation between a warming temperature and interannual CO_2 flux over tropical regions was also noted by Wang et al. (2014) and Wang et al. (2013). On the other hand, a negative and near-zero correlation was observed in Southern tropical Africa and tropical East Africa. Typically, the correlation reaches up to -0.2 in regions like Angola and Tanzania, suggesting that temperature has a weak contribution to interannual CO_2 flux variability in Southern tropical Africa and tropical East Africa.

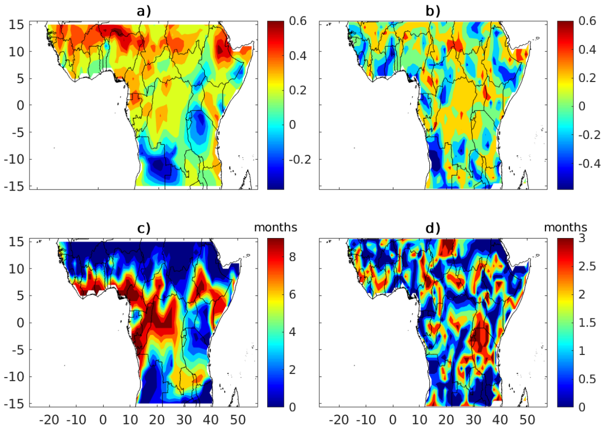

FIGURE 5.10: a) Correlation of interannual temperature fluctuation with Niño 3.4 index, and c) the corresponding lag time in units of months; b) correlation of interannual fluctuations of temperature with CO_2 flux and d) the corresponding lag time in units of months.

5.3.6 Influence of El Niño induced precipitation on CO_2 flux fluctuation

Precipitation signal of the region was decomposed into its seasonal and interannual variability using EEMD, which shows that precipitation has strong seasonal and interannual fluctuations. The interannual fluctuation of precipitation over the region was correlated with Niño 3.4 index and interannual fluctuation of CO_2 over the region during the same period. Fig. 5.11 shows these correlations. The correlation between the interannual fluctuation of precipitation with Niño 3.4 ranges from -0.5 to 0.5 with a lag time ranging from 0 to 9 months. A positive correlation was obtained in tropical Western Africa, East Africa regions and the Democratic Republic of Congo. Previous studies also confirmed tropical East Africa regions received above-average rainfall during El Niño while below-average rainfall during La Niña events (Endris et al., 2013; Nicholson and Selato, 2000, and references therein). Surface ocean warming in the western Indian Ocean leads to intensification and shift of the ITCZ, bringing more precipitation to eastern Africa (Mengistu Tsidu, 2017; Wolff et al., 2011; Mutai and Ward, 2000) during El Niño events. In tropical East Africa region, El Niño has a negative and near zero correlation implying the El Niño induced precipitation, which results in a rising of net atmospheric CO_2 flux within 3 months after the occurrence of El Niño. However, El Niño induced precipitation over tropical rain forest (Fig. 5.11b) leads a net CO_2 flux sink. Therefore, El Niño induced precipitation can be considered as the main driver of rising CO_2 flux variability at interannual scale over Tropical East and tropical West Africa. In contrast, the rising precipitation is responsible for lowering atmospheric CO_2 flux in the Democratic Republic of Congo at the interannual time scale.

5.3.7 Influence of El Niño induced soil moisture on CO_2 flux fluctuation

Fig. 5.12 shows the correlations and corresponding lag months of interannual fluctuation of root zone soil moisture signals with Niño 3.4 index and interannual CO_2 flux. A positive correlation between interannual variability of root zone soil moisture and Niño 3.4 observed over tropical West Africa and tropical East Africa (Fig. 5.12a) with a lag month ranging from 0 to 9 months (Fig. 5.12c). In contrast, a negative correlation between interannual variability of CO_2 and root zone soil moisture was observed over tropical East Africa (Fig. 5.12b). Therefore, the rising moisture increases terrestrial uptake of CO_2 by reducing soil CO_2 emission and enhancing the vegetation cover of tropical East Africa.

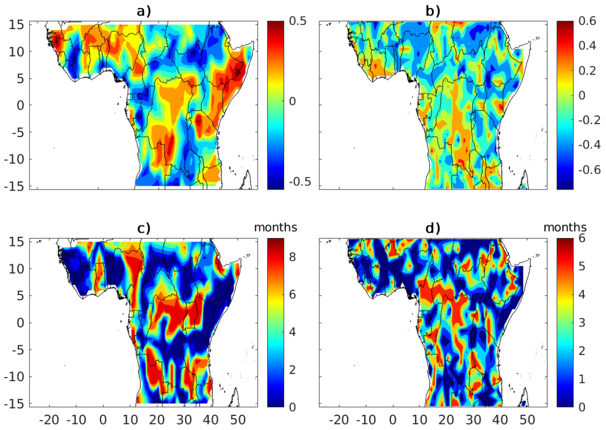

FIGURE 5.11: The same as Fig. 5.10 but with interannual fluctuation of precipitation.

On the other hand, the negative correlation between root zone soil moisture and Niño 3.4 (Fig. 5.12a) was found over Ethiopian highlands. Moreover, the region also experienced a positive correlation between soil moisture and CO_2 (Fig. 5.12b) suggesting that more CO_2 flux was added to the atmosphere due to enhanced microbial activity and reduced uptake of CO_2 by the land biosphere from the Ethiopian Highlands.

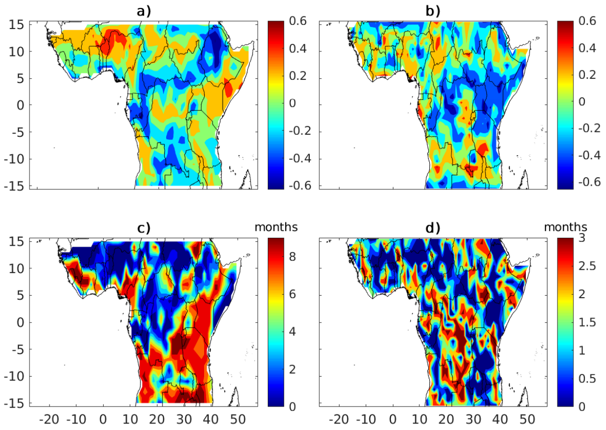

FIGURE 5.12: The same as Fig. 5.10 but with root zone soil moisture.

5.3.8 Influence of El Niño induced enhanced vegetation index on CO_2 flux fluctuation

Fig. 5.13a shows a negative and near-zero correlation between the interannual variability of EVI and Niño 3.4 over tropical Western Africa, tropical North

Africa, Ethiopian highlands and tropical rainforest with a lag time ranging from 2 to 6 months. These regions also show a positive correlation between temperature and precipitation with Niño 3.4 index respectively (see Figs. 5.10a and 5.11a). indicating the warm atmospheric condition creates a favourable condition for plant growth over these regions. In addition, Fig. 5.13b shows EVI has a negative correlation with CO_2 flux which suggests El Niño induced temperature change decreases the vegetation cover and enhances atmospheric CO_2 growth over tropical Northern Africa. On the other hand, a positive correlation was observed between EVI and Niño 3.4 which is most probably driven by increased precipitation and soil moisture over tropical East Africa regions (Fig. 5.13a). Moreover, EVI has a negative correlation with CO_2 implying enhanced vegetation growth over the region increases CO_2 uptake.

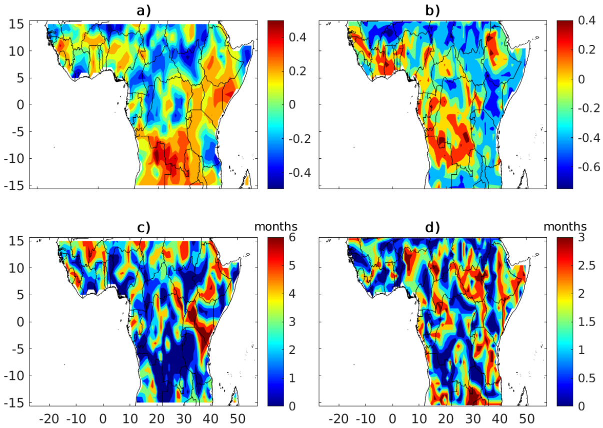

FIGURE 5.13: The same as Fig. 5.10 but with enhanced vegetation index.

5.4 Summary

We discuss the response of terrestrial atmospheric exchange of CO_2 flux at various localities over tropical Africa with ENSO events, temperature, precipitation, vegetation index, and soil moisture. Concurrent and lag correlations of temperature, precipitation, soil moisture, EVI and Niño 3.4 indices with CO_2 flux over Equatorial Africa landmass covering the period from 2000 to 2016 at the pixel scale are analyzed. Natural CO_2 flux has six periodicities over tropical Africa in response to different drivers at seasonal and interannual scales. In general, tropical Africa is a net sink of 7.2 $gC/m^2/yr$ but in recent years this CO_2 uptake of the region has been declining. Furthermore, during the strongest El Niño years of 2015/16 tropical Africa releases 29.12 $gC/m^2/yr$ into the atmosphere. The natural CO_2 flux shows a good correlation coefficient of -0.6, 0.4, -0.6, -0.6 with precipitation, temperature, enhanced vegetation index and root zone soil moisture at seasonal scale respectively. At seasonal time CO_2 fluctuation is strongly controlled by precipitation over tropical East Africa and tropical rain forest regions. However, both precipitation and temperature play a significant role over the tropical savanna regions. Interannual temperature variability was found to be the most dominant driver for the rising of atmospheric CO_2 flux at this time scale in most regions of the tropical rain forest and tropical North Africa. A significant positive correlation between interannual temperature variability and Niño 3.4 index over the tropical rain forest and tropical north Africa implies El Niño induced temperature change drives interannual CO_2 variability over these regions. On the other hand, precipitation plays a significant role in tropical southern Africa. In tropical East Africa, the rising of El Niño induced precipitation favours greening and enhancement of soil moisture which improves CO_2 uptake of the region. In contrast, a warm and dry condition associated with less soil moisture and vegetation cover reduces CO_2 uptake over Ethiopian Highlands.

Chapter 6

Conclusions

This graduation thesis aims to study the dynamics of CO_2 flux over Africa's landmass. The CO_2 flux due to the biosphere-atmosphere exchange (GPP, TER, NEE) is the most uncertain flux in the carbon study. These flux components are the major components in CO_2 fluctuation and result from the land-use change by natural phenomena or human intervention. The study uses the NOAA's Carbon Tracker CO_2 flux data of version CT2017-flux covering the period from 2000 - 2016 and also employed the advantage of SIF and NIRv to investigate the spatiotemporal dynamics and drivers of these CO_2 fluxes for major biomes in Africa. This chapter discusses to what extent our research questions in section 1.1 were addressed.

The first step before the use of data from models requires the assessment of model skills in simulating limited existing observations reasonably well. In this study, we have assessed how good enough are the XCO_2 data from satellite observations in comparison with the CT model and in-situ flask observations over Africa. Our result reveals that XCO_2 from NOAA's Carbon Tracker has biases of -0.28 and 0.34 ppm, correlations of 0.83 and 0.60 and root mean square deviations of 2.30 and 2.57 ppm with respect to GOSAT's and OCO-2's XCO_2 respectively averaged over Africa's landmass. These results indicate that these datasets are consistent at the continental scale. However, we illustrate that the time-series comparison at pixel scale suffers from a large inconsistency in between the model simulation and the satellite observations. We also found that these strong discrepancies occurred during the high vegetation productivity season and/or during seasons of high aerosol loading. The relationship between seasonal dynamics of vegetation and aerosol loading with XCO_2 will help further understanding of the source of these deviations. We also compared satellite observations and CT with ground-based flask observation and found that CT has a better performance over sites located in North Africa (IZO, ASK) as determined from a good agreement with flask observations where satellite observations underestimate. Conversely, satellite observations have better performance over island sites (ASC and SEY).

We understand that neither the model simulation nor satellite observations are a metric for XCO_2 estimation. However, consistency is expected among datasets. We, therefore, assessed the consistency of XCO_2 from the CT model simulation to that of XCO_2 from GOSAT/OCO-2 satellite observations in capturing the amplitudes and phases of observed seasonal cycles over different parts of Africa landmass. The study showed that the timeseries of XCO_2 from the model and these satellites have a good agreement in capturing the pattern and amplitude of observed seasonal cycles over different parts of the continent. However, we found that this agreement deteriorates over equatorial and southern Africa in terms of amplitude. We also found that there is a seasonally dependent bias between them, which is negative during dry seasons while it is positive during the wet season. These results suggest additional studies should be done to further understand the root causes of discrepancy and seasonal dependent bias in the datasets.

In general, the study revealed that XCO_2 from NOAA's CT shows a very small bias and regionally consistent with respect to GOSAT and OCO-2 observations over Africa's landmass. Moreover, the study illustrated that the expected seasonal variability was captured by both model simulation and satellite observations, which are higher in winter and drought seasons, but lower in summer. These results suggest that both datasets can be used to understand the carbon budget and climate change at regional to global scales. On top of satellite observations, CT model products have a spatially regular and high temporal resolution, which suggests that CT products are the preferred dataset to study the carbon cycle of Africa. On the other hand, the study also showed that there are some discrepancies between the model and the two XCO_2 datasets from GOSAT and OCO-2 along with the annual mean ITCZ location and during high productivity seasons. Even good consistency among these datasets may not guarantee the XCO_2 values of the region are accurately estimated. For that, both datasets should be compared against independent ground measurements such as TCCON. Unfortunately, there are no TCCON stations over Africa's mainland and very few flask observations. Therefore, it is difficult to conclude whether the satellite observation or the model simulation is accurate at this stage. Our study indicates a spatiotemporal consistency among these datasets, which provides information for both modeller and satellite retrieval experts where/when the magnitudes of biases are high. However, additional studies are needed to further demonstrate the capacity of the model simulation and satellite observations by strengthening ground-based observations to further investigate their accuracy over the region. For example, the accuracy of the model data needs further improvement for the rainforest regions (e.g., Congo) through assimilation of in-situ observations and tuning of the model through process studies. Recent studies have suggested that current aerosol loading can significantly affect the carbon flux and atmospheric CO_2 concentrations by diffuse radiation, fertilization effects and hydro-meteorological feedback. These effects also need to be considered in future studies.

The amount of carbon absorbed by terrestrial plants via photosynthesis constitutes the largest CO_2 flux between the terrestrial biosphere and the atmosphere. The lack of a reliable GPP proxy with sufficient resolution and global coverage makes it the most uncertain in the carbon budget study. In this thesis, we, therefore, illustrate the usefulness of SIF and NIRv as GPP proxies over Africa. We compared SIF and NIRv with flux tower measurements from six EC flux sites in Africa. Our results reveal that SIF and NIRv can capture the seasonality of measured GPP over most sites. The relationship between SIF/NIRv and GPP was stronger ($R > 0.90$) in C4 vegetation were examined at both Sudan (SD-Dem) and Senegal (SN-Dhr) sites. However, we found the seasonal dynamics of the tower GPP from Ghana (GH-Ank) were not captured. Additional studies are required to explain the main causes for the disagreement among these datasets in capturing the GPP patterns for this GH-Ank flux tower.

Our study also shows that SIF and NIRv capture the seasonal cycle well while the model and vegetation index shows saturation when production is high. SIF and NIRv also show slightly higher correlations with tower GPP than EVI, indicating that these two show better performance than the greenness index. Our study evidenced that SIF and NIRv are robust in estimating GPP for a wide variety of Africa's biomes and illustrates the great potential of SIF and NIRv in ecosystem functioning and carbon cycling studies. We demonstrated that SIF and NIRv do a better job than EVI and NDVI in capturing the seasonal dynamics of GPP. However, a performance comparison of SIF and NIRv against VI's (EVI or NDVI) is needed to conclude which one is better than the other more quantitatively. The thesis also evidenced that a weak relationship between all GPP proxies used in the study and EC-GPP for broadleaf evergreen vegetation that was examined in Ghana (GH-Ank). These results are illustrative for tropical ecosystems, where GPP variations are irregular and strongly coupled to the leaf phenology of vegetation. We recommend future work based on a higher resolution of SIF along with process-based modelling or considering the synergy use of SIF with spatially and temporally continuous remote sensing products (e.g., MODIS NIRv) and SIF observations from other missions (e.g., OCO-2, TROPOMI, FLEX) to improve our understanding of GPP more robustly.

The effect of environmental stress factors such as the amount of solar illumination, amount of water content in the soil in relation to GPP should be assessed. For that reason, we investigated the response of SIF and NIRv to the amount of soil moisture and shortwave radiation. Our results imply that SIF and NIRv are strongly controlled by the seasonality of soil moisture, with a weak influence of light availability superimposed. This is recognized by the positive correlation between SIF/NIRv, which independently display the same patterns and soil moisture in both hemispheres. Peak productivity coincides with the peak soil moisture that occurs in September on the northern hemisphere of Africa, and in March on the southern hemisphere of Africa. Despite the substantial value and potential of SIF in assessing terrestrial photosynthesis and its response to environmental stresses, there are still challenges due to gaps in the data. We showed that SIF/NIRv explains the seasonal variance of GPP. However, further studies should be done to investigate how anomalies in the soil moisture, absorbed photosynthetically active radiation and other environmental stress factors (e.g., vapour pressure deficiency and temperature) are captured by SIF/NIRv.

The thesis has also shown that the mean climatology map of SIF, NIRv and GPP from the MPI-BGC agree widely in large parts of Africa, suggesting that these products are more robust GPP proxies. We estimate SIF/NIRv based GPP using a simple linear model and demonstrated that the aggregated SIF and NIRv based GPP over the six major biomes well captures the aggregated GPP from MPI-BGC. We also demonstrated that the predicted GPP from SIF and NIRv effectively track the magnitude and seasonal dynamics of the towers GPP. The seasonality of GPP well captures the beginning period, thriving period, and the end period of the growing season. These results suggest that the SIF and NIRv based GPP shows a reasonable first estimate of spatiotemporal GPP patterns without the need for the more complex and data-intensive machine-learning approach. At least, it captures the large differences between the major biomes of Africa, allowing further study of their seasonal dynamics, drought response, and contribution to tropical GPP. A more accurate estimation of GPP from SIF/NIRv can be achieved through a process-based modelling approach, which was not the objective of this thesis. Especially, the possibility of calculating NIRv from the existing satellites allows estimating satellite-derived plant photosynthesis going back to some decades. This provides a chance to directly use satellite measurements of SIF and NIRv to improve the estimation of GPP from ecosystem models which in turn improves our understanding of the plant evolutionary and physiological processes.

Understanding of CO_2 flux fluctuations in response to the main drivers is paramount to quantify the sensitivity of the carbon cycle to climate variability. In this study, we apply an Ensemble Empirical Mode Decomposition (EEMD) and obtained CO_2 flux fluctuations at seasonal, interannual, and decadal time scales. Our results showed that tropical Africa was a net CO_2 flux sink, but in recent years this CO_2 uptake of the region has been declining. We also determined that the seasonal variability of natural CO_2 flux has a strong correlation with precipitation with a correlation of up to -0.6, near-surface air temperature with a correlation of up to 0.4, root zone soil moisture with a correlation of up to -0.6 and EVI with a correlation of up to -0.6 over tropical Africa. We noted a higher correlation over the savanna grassland region than over tropical rainforest and Tropical East Africa. In contrast, low correlations were observed over the Democratic Republic of Congo (DRC), semi-desert regions of East Africa (Eastern Ethiopia, Somalia, and Northeast Kenya) and the West coast of Africa. Moreover, our analysis shows that the natural CO_2 flux is negatively correlated to precipitation, root zone soil moisture, and EVI but positively correlated with temperature. On the other hand, we also noted a reverse situation over semi-desert regions of East Africa. We analyzed the seasonal variability of CO_2 dominantly depending on precipitation over Tropical East Africa and tropical rainforest regions. However, both precipitation and temperature play a significant role over the tropical savanna regions. Our result illustrates a higher atmospheric CO_2 flux in association with warm and dry conditions. Natural CO_2 flux over tropical Africa covering the period from 2000 to 2016 shows a nonlinear downward trend, implying a reduced terrestrial CO_2 uptake and/or rising CO_2 emissions from forest fires, which need further investigation of the seasonal dynamics of vegetation and emissions from the forest fire.

The response of terrestrial-atmospheric exchange of CO_2 flux at various localities over tropical Africa to ENSO events was also investigated. Our results illustrate that carbon uptake of tropical Africa was strongly influenced by El Niño Southern Oscillation at the interannual scale. The interannual fluctuation of CO_2 flux shows a strong correlation (up to 0.6) with the Niño 3.4 index over Benin, Nigeria, Chad, and Kenya and Tanzania. We found high reductions in land uptake and strong positive anomalies in the atmospheric CO_2 flux during El Niño events. We also demonstrated that over most of the tropical Africa region, the interannual variability of CO_2 flux was found to be in-phase with interannual fluctuation of temperature while precipitation is out-phase. Moreover, tropical North Africa shows a no anomalous peak even in response to the strongest El Niño event.

We illustrated an anomalously greatest CO_2 flux during the 2015/16 El Niño year since 2000. We have also found that tropical Africa was a net CO_2 flux sink (-7.02 gC/m2/year) during the period covering from 2000 to 2016. However, during the strongest El Niño years of 2015/16, we investigated that tropical Africa releases 29.12 gC/m2/year into the atmosphere. During this particular El Niño year, we noted that dry and warm conditions cause the rising of CO_2 flux over Western Africa and Ethiopian highlands. On the other hand, warm and wet conditions were observed over the tropical rainforest and tropical East Africa, which implies that interannual temperature variability was the main driver for the observed peak in the net atmospheric CO_2 flux over these regions during this particular El Niño year.

We investigated a significant positive correlation between temperature and Niño 3.4 index over the tropical rainforest and tropical North Africa. This implies El Niño induced temperature change drives the interannual CO_2 variability over these regions. On the other hand, we noted that temperature has a weak role in tropical southern Africa. In tropical East Africa, we investigated that a significant positive correlation between interannual fluctuations of precipitation and Niño 3.4 index, suggesting that the rising of El Niño induced precipitation favours greening and enhancement of soil moisture which improve CO_2 uptake of the region. In contrast, we noted that a warm and dry condition associated with less soil moisture and vegetation cover reduces CO_2 uptake over Ethiopian Highlands. Further efforts are required to strengthen the ground observational network and develop inverse modelling algorithms to adequately study the water and carbon flux in Africa ecosystem.

Bibliography

Abdi, Abdulhakim M et al. (2017). “Evaluating water controls on vegetation growth in the semi-arid Sahel using field and Earth observation data”. In: *Remote Sensing* 9.3, p. 294.

Ahlström, Anders et al. (2015). “The dominant role of semi-arid ecosystems in the trend and variability of the land CO2 sink”. In: *Science* 348.6237, pp. 895–899.

Anav, Alessandro et al. (2015). “Spatiotemporal patterns of terrestrial gross primary production: A review”. In: *Reviews of Geophysics* 53.3, pp. 785–818.

Anderegg, William RL et al. (2012). “The roles of hydraulic and carbon stress in a widespread climate-induced forest die-off”. In: *Proceedings of the National Academy of Sciences* 109.1, pp. 233–237. DOI: `10.1073/pnas.1107891109`.

Araújo, AC et al. (2002). “Comparative measurements of carbon dioxide fluxes from two nearby towers in a central Amazonian rainforest: The Manaus LBA site”. In: *Journal Of Geophysical Research-Atmospheres* 107, pp. –.

Ardö, Jonas (2015). “Comparison between remote sensing and a dynamic vegetation model for estimating terrestrial primary production of Africa”. In: *Carbon balance and management* 10.1, p. 8.

Arvor, Damien et al. (2011). “Classification of MODIS EVI time series for crop mapping in the state of Mato Grosso, Brazil”. In: *International Journal of Remote Sensing* 32.22, pp. 7847–7871.

Bacastow, RB et al. (1980). “Atmospheric carbon dioxide, the Southern Oscillation, and the weak 1975 El Niño”. In: *Science* 210.4465, pp. 66–68.

Badgley, Grayson, Christopher B Field, and Joseph A Berry (2017). “Canopy near-infrared reflectance and terrestrial photosynthesis”. In: *Science advances* 3.3, e1602244.

Baldocchi, Dennis et al. (1996). “Strategies for measuring and modelling carbon dioxide and water vapour fluxes over terrestrial ecosystems”. In: *Global change biology* 2.3, pp. 159–168.

Baldocchi, Dennis et al. (2001). “FLUXNET: A new tool to study the temporal and spatial variability of ecosystem-scale carbon dioxide, water vapor, and energy flux densities”. In: *Bulletin of the American Meteorological Society* 82.11, pp. 2415–2434.

Ballantyne, AP, P Ciais, and JB Miller (2018). “Cautious optimism and incremental goals toward stabilizing atmospheric CO2”. In: *Earth’s Future* 6.12, pp. 1632–1637.

Bateni, SM and D Entekhabi (2012). “Relative efficiency of land surface energy balance components”. In: *Water Resources Research* 48.4. DOI: `10.1029/2011WR011357`.

Batjes, Niels H (1996). “Total carbon and nitrogen in the soils of the world”. In: *European journal of soil science* 47.2, pp. 151–163. DOI: `10.1111/j.1365-2389.1996.tb01386.x`.

Beer, Christian et al. (2010). “Terrestrial gross carbon dioxide uptake: global distribution and covariation with climate”. In: *Science* 329.5993, pp. 834–838.

Bhargava, Sujata and Kshitija Sawant (2013). “Drought stress adaptation: metabolic adjustment and regulation of gene expression”. In: *Plant Breeding* 132.1, pp. 21–32. DOI: `10.1111/pbr.12004`.

Bhattacharya, Amitav (2018). *Changing Climate and Resource Use Efficiency in Plants*. Academic Press.

Bie, Nian et al. (2018). “Regional uncertainty of GOSAT XCO_2 retrievals in China: quantification and attribution”. In: *Atmospheric Measurement Techniques* 11.3, pp. 1251–1272. DOI: `10.5194/amt-11-1251-2018`.

Blunden, Jessica and Derek S Arndt (2019). “State of the Climate in 2018”. In: *Bulletin of the American Meteorological Society* 100.9, Si–S306.

Bobe, R (2006). “The evolution of arid ecosystems in eastern Africa”. In: *Journal of Arid Environments* 66.3, pp. 564–584.

Boesch, Hartmut et al. (2011). “Global characterization of CO2 column retrievals from shortwave-infrared satellite observations of the Orbiting Carbon Observatory-2 mission”. In: *Remote Sensing* 3.2, pp. 270–304.

Bonal, Damien et al. (2016). “The response of tropical rainforests to drought—lessons from recent research and future prospects”. In: *Annals of forest science* 73.1, pp. 27–44.

Bonan, Gordon B (2008). “Forests and climate change: forcings, feedbacks, and the climate benefits of forests”. In: *science* 320.5882, pp. 1444–1449.

Boretti, Albert and Singarayer Florentine (2019). “Atmospheric CO2 concentration and other limiting factors in the growth of C3 and C4 plants”. In: *Plants* 8.4, p. 92.

Bousquet, Philippe et al. (2000). “Regional changes in carbon dioxide fluxes of land and oceans since 1980”. In: *Science* 290.5495, pp. 1342–1346.

Callies, J et al. (2000). “GOME-2-Metop’s second-generation sensor for operational ozone monitoring”. In: *ESA bulletin* 102, pp. 28–36.

Camberlin, Pierre (1995). "June-september rainfall in north-eastern Africa and atmospheric signals over the tropics: A zonal perspective". In: *International Journal of Climatology* 15.7, pp. 773–783.

Canadell, JG, MR Raupach, and RA Houghton (2009). "Anthropogenic CO 2 emissions in Africa". In: *Biogeosciences* 6.3, pp. 463–468.

Canadell, Josep G et al. (2007). "Contributions to accelerating atmospheric CO2 growth from economic activity, carbon intensity, and efficiency of natural sinks". In: *Proceedings of the national academy of sciences* 104.47, pp. 18866–18870.

Cane, Mark A (2005). "The evolution of El Niño, past and future". In: *Earth and Planetary Science Letters* 230.3-4, pp. 227–240.

Carré, F et al. (2010). "Background guide for the calculation of land carbon stocks in the biofuels sustainability scheme: drawing on the 2006 IPCC guidelines for national greenhouse gas inventories". In: *Luxembourg: Joint Research Center, European Commission, EUR* 24573.10.2788, p. 34463.

Ceccato, Pietro et al. (2001). "Detecting vegetation leaf water content using reflectance in the optical domain". In: *Remote sensing of environment* 77.1, pp. 22–33.

Chambers, J Q et al. (2004). "Respiration from a Tropical Forest Ecosystem: Partitioning of Sources and Low Carbon Use Efficiency". In: *Ecological Applications* 14.4, S72–S88.

Chatterjee, A et al. (2017). "Influence of El Niño on atmospheric CO2 over the tropical Pacific Ocean: Findings from NASA's OCO-2 mission". In: *Science* 358.6360, eaam5776.

Chen, Xuejuan et al. (2019). "Drought detection and assessment with solar-induced chlorophyll fluorescence in summer maize growth period over North China Plain". In: *Ecological Indicators* 104, pp. 347–356.

Chevallier, Frédéric (2007). "Impact of correlated observation errors on inverted CO2 surface fluxes from OCO measurements". In: *Geophysical Research Letters* 34.24.

— (2015). "On the statistical optimality of CO 2 atmospheric inversions assimilating CO 2 column retrievals". In: *Atmospheric Chemistry and Physics* 15.19, pp. 11133–11145.

Churkina, Galina and Steven W Running (1998). "Contrasting climatic controls on the estimated productivity of global terrestrial biomes". In: *Ecosystems* 1.2, pp. 206–215.

Ciais, P et al. (1996). “A large northern hemisphere terrestrial CO 2 sink indicated by the 1 3 C 1 2 C ratio of atmospheric CO 2”. In: *Oceanographic Literature Review* 2.43, pp. 123–124.

Ciais, P et al. (2011). “The carbon balance of Africa: synthesis of recent research studies”. In: *Philosophical Transactions of the Royal Society of London A: Mathematical, Physical and Engineering Sciences* 369.1943, pp. 2038–2057.

Clark, David A et al. (2003). “Tropical rain forest tree growth and atmospheric carbon dynamics linked to interannual temperature variation during 1984–2000”. In: *Proceedings of the national academy of sciences* 100.10, pp. 5852–5857.

Connor, Brian J et al. (2008). “Orbiting Carbon Observatory: Inverse method and prospective error analysis”. In: *Journal of Geophysical Research: Atmospheres* 113.D5.

Cox, Peter M et al. (2000). “Acceleration of global warming due to carbon-cycle feedbacks in a coupled climate model”. In: *Nature* 408.6809, pp. 184–187. DOI: `10.1038/35041539`.

Cox, Peter M et al. (2013a). “Sensitivity of tropical carbon to climate change constrained by carbon dioxide variability”. In: *Nature* 494.7437, p. 341.

Cox, PM et al. (2013b). “Carbon dioxide variability constrains the sensitivity of tropical carbon to climate change”. In: *Nature* 494, pp. 341–344.

Crisp, David et al. (2012). “The ACOS CO2 retrieval algorithm-Part II: Global XCO2 data characterization”. In:

Damm, Alexander et al. (2015). “Far-red sun-induced chlorophyll fluorescence shows ecosystem-specific relationships to gross primary production: An assessment based on observational and modeling approaches”. In: *Remote Sensing of Environment* 166, pp. 91–105.

Dee, Dick P et al. (2011). “The ERA-Interim reanalysis: Configuration and performance of the data assimilation system”. In: *Quarterly Journal of the royal meteorological society* 137.656, pp. 553–597.

Deng, Anjian et al. (2016a). “Intercomparison of Carbon Dioxide Products Retrieved from GOSAT Short-Wavelength Infrared Spectra for Three Years (2010–2012)”. In: *Atmosphere* 7.9, p. 109.

Deng, Feng et al. (2016b). “Combining GOSAT XCO2 observations over land and ocean to improve regional CO2 flux estimates”. In: *Journal of Geophysical Research: Atmospheres* 121.4, pp. 1896–1913.

Dobbs, ME et al. (2008). “A modulated CW fiber laser-lidar suite for the ASCENDS mission”. In: *Proc. 24th International Laser Radar Conference*.

Doney, Scott C and David S Schimel (2007). "Carbon and climate system coupling on timescales from the Precambrian to the Anthropocene". In: *Annu. Rev. Environ. Resour.* 32, pp. 31–66.

Doughty, Russell et al. (2019). "TROPOMI reveals dry-season increase of solar-induced chlorophyll fluorescence in the Amazon forest". In: *Proceedings of the National Academy of Sciences* 116.44, pp. 22393–22398.

Duveiller, Gregory et al. (2019). "A spatially downscaled sun-induced fluorescence global product for enhanced monitoring of vegetation productivity". In:

Ekwurzel, Brenda et al. (2017). "The rise in global atmospheric CO 2, surface temperature, and sea level from emissions traced to major carbon producers". In: *Climatic Change* 144.4, pp. 579–590.

Endris, Hussen Seid et al. (2013). "Assessment of the performance of CORDEX regional climate models in simulating East African rainfall". In: *Journal of Climate* 26.21, pp. 8453–8475.

Falge, Eva et al. (2001). "Gap filling strategies for defensible annual sums of net ecosystem exchange". In: *Agricultural and forest meteorology* 107.1, pp. 43–69.

Feely, Richard A et al. (1995). "CO2 distributions in the equatorial Pacific during the 1991–1992 ENSO event". In: *Deep Sea Research Part II: Topical Studies in Oceanography* 42.2-3, pp. 365–386.

Feist, D G. et al. (2014). *TCCON data from Ascension Island (SH), Release GGG2014R0. TCCON data archive, hosted by CaltechDATA*. DOI: `10.14291`.

Field, CB, J Sarmiento, and B Hales (2007). "The carbon cycle of North America in a global context". In: *The First State of the Carbon Cycle Report (SOCCR): The North American Carbon Budget and Implications for the Global Carbon Cycle*, pp. 21–28.

Fisher, Joshua B et al. (2013). "African tropical rainforest net carbon dioxide fluxes in the twentieth century". In: *Philosophical Transactions of the Royal Society B: Biological Sciences* 368.1625, p. 20120376.

Foken, Thomas, Marc Aubinet, and Ray Leuning (2012). "The eddy covariance method". In: *Eddy covariance*. Springer, pp. 1–19. DOI: `10.1007/978-94-007-2351-1_1`.

Francey, RJ et al. (1995). "Changes in oceanic and terrestrial carbon uptake since 1982". In: *Nature* 373.6512, p. 326.

Frankenberg, C et al. (2012). "Remote sensing of near-infrared chlorophyll fluorescence from space in scattering atmospheres: implications for its retrieval and interferences with atmospheric CO_2 retrievals". In: *Atmospheric Measurement Techniques* 5.8, pp. 2081–2094.

Frankenberg, Christian et al. (2011). “New global observations of the terrestrial carbon cycle from GOSAT: Patterns of plant fluorescence with gross primary productivity”. In: *Geophysical Research Letters* 38.17.

Frankenberg, Christian et al. (2014). “Prospects for chlorophyll fluorescence remote sensing from the Orbiting Carbon Observatory-2”. In: *Remote Sensing of Environment* 147, pp. 1–12.

Frankenberg, Christian et al. (2016). “Using airborne HIAPER Pole-to-Pole Observations (HIPPO) to evaluate model and remote sensing estimates of atmospheric carbon dioxide”. In: *Atmospheric Chemistry and Physics* 16.12, pp. 7867–7878.

Friedlingstein, Pierre et al. (2006). “Climate–carbon cycle feedback analysis: results from the C4MIP model intercomparison”. In: *Journal of climate* 19.14, pp. 3337–3353.

Gaubert, Benjamin et al. (2019). “Global atmospheric CO2 inverse models converging on neutral tropical land exchange, but disagreeing on fossil fuel and atmospheric growth rate”. In: *Biogeosciences* 16.1, pp. 117–134.

Gentine, Pierre, Dara Entekhabi, and Jan Polcher (2011). “The diurnal behavior of evaporative fraction in the soil–vegetation–atmospheric boundary layer continuum”. In: *Journal of Hydrometeorology* 12.6, pp. 1530–1546. DOI: `10.1175/2011JHM1261.1`.

Giannini, Alessandra, R Saravanan, and Ping Chang (2005). “Dynamics of the boreal summer African monsoon in the NSIPP1 atmospheric model”. In: *Climate Dynamics* 25.5, pp. 517–535.

Gilmanov, Tagir G, Douglas A Johnson, and Nicanor Z Saliendra (2003). “Growing season CO2 fluxes in a sagebrush-steppe ecosystem in Idaho: Bowen ratio/energy balance measurements and modeling”. In: *Basic and applied ecology* 4.2, pp. 167–183.

Girardin, Cécile AJ et al. (2016). “Seasonal trends of Amazonian rainforest phenology, net primary productivity, and carbon allocation”. In: *Global Biogeochemical Cycles* 30.5, pp. 700–715.

Good, Peter et al. (2015). “Nonlinear regional warming with increasing CO 2 concentrations”. In: *Nature Climate Change* 5.2, p. 138.

Goody, Richard M and Yuk Ling Yung (1995). *Atmospheric radiation: theoretical basis*. Oxford university press.

Green, Julia K et al. (2019). “Large influence of soil moisture on long-term terrestrial carbon uptake”. In: *Nature* 565.7740, p. 476. DOI: `10.1038/s41586-018-0848-x`.

Guanter, Luis et al. (2014). "Global and time-resolved monitoring of crop photosynthesis with chlorophyll fluorescence". In: *Proceedings of the National Academy of Sciences* 111.14, E1327–E1333.

Guntinas, ME et al. (2013). "Sensitivity of soil respiration to moisture and temperature". In: *Journal of soil science and plant nutrition* 13.2, pp. 445–461. DOI: `10.4067/S0718-95162013005000035`.

Gurney, Kevin R et al. (2008). "Interannual variations in continental-scale net carbon exchange and sensitivity to observing networks estimated from atmospheric CO2 inversions for the period 1980 to 2005". In: *Global biogeochemical cycles* 22.3.

Hamazaki, Takashi et al. (2005). "Fourier transform spectrometer for greenhouse gases observing satellite (GOSAT)". In: *Enabling sensor and platform technologies for spaceborne remote sensing*. Vol. 5659. International Society for Optics and Photonics, pp. 73–81.

Hao, Wei Min and Mei-Huey Liu (1994). "Spatial and temporal distribution of tropical biomass burning". In: *Global biogeochemical cycles* 8.4, pp. 495–503. DOI: `10.1029/94GB02086`.

Hayek, Matthew N et al. (2018). "A novel correction for biases in forest eddy covariance carbon balance". In: *Agricultural and Forest Meteorology* 250, pp. 90–101.

Hew, Choy-Sin, Go Krotkov, and David T Canvin (1969). "Effects of temperature on photosynthesis and CO2 evolution in light and darkness by green leaves". In: *Plant physiology* 44.5, pp. 671–677.

Hirons, Linda and Nick Klingaman (2016). "El Niño 2015/2016 impact analysis, monthly outlook March 2016". In:

Hoerling, Martin P and Arun Kumar (2000). *Understanding and predicting extratropical teleconnections related to ENSO*. Cambridge University Press.

Hollinger, DY et al. (1999). "Seasonal patterns and environmental control of carbon dioxide and water vapour exchange in an ecotonal boreal forest". In: *Global Change Biology* 5.8, pp. 891–902.

Houghton, RA (2007). "Balancing the global carbon budget". In: *Annu. Rev. Earth Planet. Sci.* 35, pp. 313–347.

Houghton, Richard A and George M Woodwell (1989). "Global climatic change". In: *Scientific American* 260.4, pp. 36–47.

Houweling, S et al. (2004). "Inverse modeling of CO 2 sources and sinks using satellite data: a synthetic inter-comparison of measurement techniques and their performance as a function of space and time". In: *Atmospheric Chemistry and Physics* 4.2, pp. 523–538.

Huang, Norden E and Zhaohua Wu (2008). "A review on Hilbert-Huang transform: Method and its applications to geophysical studies". In: *Reviews of geophysics* 46.2.

Huang, Norden E et al. (1998). "The empirical mode decomposition and the Hilbert spectrum for nonlinear and non-stationary time series analysis". In: *Proceedings of the Royal Society of London A: mathematical, physical and engineering sciences*. Vol. 454. 1971. The Royal Society, pp. 903–995.

Huang, Norden E et al. (2003). "A confidence limit for the empirical mode decomposition and Hilbert spectral analysis". In: *Proceedings of the Royal Society of London A: Mathematical, Physical and Engineering Sciences*. Vol. 459. 2037. The Royal Society, pp. 2317–2345.

Huang, Xiaojuan, Jingfeng Xiao, and Mingguo Ma (2019). "Evaluating the Performance of Satellite-Derived Vegetation Indices for Estimating Gross Primary Productivity Using FLUXNET Observations across the Globe". In: *Remote Sensing* 11.15, p. 1823.

Huete, Alfredo et al. (2002). "Overview of the radiometric and biophysical performance of the MODIS vegetation indices". In: *Remote sensing of environment* 83.1-2, pp. 195–213.

Huete, Alfredo R et al. (2006). "Amazon rainforests green-up with sunlight in dry season". In: *Geophysical research letters* 33.6.

Humlum, Ole, Kjell Stordahl, and Jan-Erik Solheim (2013). "The phase relation between atmospheric carbon dioxide and global temperature". In: *Global and Planetary Change* 100, pp. 51–69.

Hungershoefer, K et al. (2010). "Evaluation of various observing systems for the global monitoring of CO 2 surface fluxes". In: *Atmospheric chemistry and physics* 10.21, pp. 10503–10520.

Idso, Craig D, Sherwood B Idso, and Robert C Balling Jr (1999). "The relationship between near-surface air temperature over land and the annual amplitude of the atmosphere's seasonal CO2 cycle". In: *Environmental and Experimental Botany* 41.1, pp. 31–37.

Inoue, M et al. (2013). "Validation of XCO 2 derived from SWIR spectra of GOSAT TANSO-FTS with aircraft measurement data". In: *Atmospheric Chemistry and Physics* 13.19, pp. 9771–9788.

Jia, Dongxiao et al. (2017). "Nonlinearity analysis and multi-model modeling of CO2 capture system". In: *Chinese Automation Congress (CAC), 2017*. IEEE, pp. 7129–7134.

Jiang, Chongya and Youngryel Ryu (2016). "Multi-scale evaluation of global gross primary productivity and evapotranspiration products derived from

Breathing Earth System Simulator (BESS)". In: *Remote Sensing of Environment* 186, pp. 528–547. DOI: `10.1016/j.rse.2016.08.030`.

Jiang, Xun et al. (2010). "Interannual variability of mid-tropospheric CO2 from Atmospheric Infrared Sounder". In: *Geophysical Research Letters* 37.13.

Jing, Yingying et al. (2018). "Global Atmospheric CO2 Concentrations Simulated by GEOS-Chem: Comparison with GOSAT, Carbon Tracker and Ground-Based Measurements". In: *Atmosphere* 9.5, p. 175.

Joiner, J et al. (2013). "Global monitoring of terrestrial chlorophyll fluorescence from moderate-spectral-resolution near-infrared satellite measurements: methodology, simulations, and application to GOME-2". In: *Atmospheric Measurement Techniques* 6.10, pp. 2803–2823.

Joiner, Joanna et al. (2016). "New methods for the retrieval of chlorophyll red fluorescence from hyperspectral satellite instruments: simulations and application to GOME-2 and SCIAMACHY." In: *Atmospheric Measurement Techniques* 9.8.

Jones, Chris D et al. (2001). "The carbon cycle response to ENSO: A coupled climate–carbon cycle model study". In: *Journal of Climate* 14.21, pp. 4113–4129.

Joos, Fortunat et al. (2013). "Carbon dioxide and climate impulse response functions for the computation of greenhouse gas metrics: a multi-model analysis". In: *Atmospheric Chemistry and Physics* 13.5, pp. 2793–2825.

Jung, Martin et al. (2010). "Recent decline in the global land evapotranspiration trend due to limited moisture supply". In: *Nature* 467.7318, pp. 951–954. DOI: `10.1038/nature09396`.

Jung, Martin et al. (2011). "Global patterns of land-atmosphere fluxes of carbon dioxide, latent heat, and sensible heat derived from eddy covariance, satellite, and meteorological observations". In: *Journal of Geophysical Research: Biogeosciences* 116.G3.

Keeling, CD and R Revelle (1985). "Effects of El Nino/Southern Oscillation on the atmospheric content of carbon dioxide". In: *Meteoritics* 20, pp. 437–450.

Keeling, Charles D (1960). "The concentration and isotopic abundances of carbon dioxide in the atmosphere". In: *Tellus* 12.2, pp. 200–203.

Keeling, Charles D, JFS Chin, and TP Whorf (1996). "Increased activity of northern vegetation inferred from atmospheric CO2 measurements". In: *Nature* 382.6587, p. 146.

Keeling, Charles D et al. (1976). "Atmospheric carbon dioxide variations at Mauna Loa observatory, Hawaii". In: *Tellus* 28.6, pp. 538–551.

Keeling, Charles D et al. (1989). "A three-dimensional model of atmospheric CO2 transport based on observed winds: 1. Analysis of observational data". In: *Aspects of climate variability in the Pacific and the Western Americas* 55, pp. 165–236.

Keeling, Charles D et al. (1995). "Interannual extremes in the rate of rise of atmospheric carbon dioxide since 1980". In: *Nature* 375.6533, p. 666.

Keppel-Aleks, G, PO Wennberg, and T Schneider (2011). "Sources of variations in total column carbon dioxide". In: *Atmospheric Chemistry and Physics* 11.8, pp. 3581–3593.

Keppel-Aleks, G et al. (2012). "The imprint of surface fluxes and transport on variations in total column carbon dioxide". In: *Biogeosciences* 9.3, pp. 875–891.

Knorr, Wolfgang and Martin Heimann (1995). "Impact of drought stress and other factors on seasonal land biosphere CO2 exchange studied through an atmospheric tracer transport model". In: *Tellus B* 47.4, pp. 471–489.

Köhler, Philipp et al. (2018). "Global retrievals of solar-induced chlorophyll fluorescence with TROPOMI: First results and intersensor comparison to OCO-2". In: *Geophysical Research Letters* 45.19, pp. 10–456.

Kong, Fanjie et al. (2016). "Land cover classification based on fused data from GF-1 and MODIS NDVI time series". In: *Remote Sensing* 8.9, p. 741.

Kong, ShaoFei et al. (2010). "Seasonal variation analysis of atmospheric CH 4, N 2 O and CO 2 in Tianjin offshore area". In: *Science China earth sciences* 53.8, pp. 1205–1215.

Koren, Gerbrand et al. (2018). "Widespread reduction in sun-induced fluorescence from the Amazon during the 2015/2016 El Niño". In: *Philosophical Transactions of the Royal Society B: Biological Sciences* 373.1760, p. 20170408.

Körner, Ch (1995). "Leaf diffusive conductances in the major vegetation types of the globe". In: *Ecophysiology of photosynthesis*. Springer, pp. 463–490.

Kottek, Markus et al. (2006). "World map of the Köppen-Geiger climate classification updated". In: *Meteorologische Zeitschrift* 15.3, pp. 259–263.

Krishnapriya, M. et al. (2017). "Seasonal and inter-annual variability of atmosphere CO2 based on NOAA Carbon Tracker analysis and satellite observations". In: *Journal of the Indian Society of Remote Sensing*, pp. 1–12.

Krol, MSBMAPWFP et al. (2005). "The two-way nested global chemistry-transport zoom model TM5: algorithm and applications". In: *Atmospheric Chemistry and Physics* 5.2, pp. 417–432.

Kruijt, B et al. (2004). "The robustness of eddy correlation fluxes for Amazon rain forest conditions". In: *Ecological Applications* 14.4, S101–S113.

Kulawik, SS et al. (2015). “Consistent evaluation of GOSAT, SCIAMACHY, CarbonTracker, and MACC through comparisons to TCCON”. In: *Atmospheric Measurement Techniques Discussions (Online)* 8.6.

Kulawik, Susan et al. (2016). “Consistent evaluation of ACOS-GOSAT, BESD-SCIAMACHY, CarbonTracker, and MACC through comparisons to TCCON”. In: *Atmospheric Measurement Techniques* 9.2, pp. 683–709.

Kuze, Akihiko et al. (2009). “Thermal and near infrared sensor for carbon observation Fourier-transform spectrometer on the Greenhouse Gases Observing Satellite for greenhouse gases monitoring”. In: *Applied optics* 48.35, pp. 6716–6733.

Lambert, G et al. (1995). “Year-to-year changes in atmospheric CO2”. In: *Tellus B* 47.1-2, pp. 53–55.

Lasslop, Gitta et al. (2010). “Separation of net ecosystem exchange into assimilation and respiration using a light response curve approach: critical issues and global evaluation”. In: *Global Change Biology* 16.1, pp. 187–208.

Lasslop, Gitta et al. (2012). “On the choice of the driving temperature for eddy-covariance carbon dioxide flux partitioning”. In: *Biogeosciences* 9, pp. 5243–5259.

Le Quere, C et al. (2013). *Global Carbon Project: the 2013 Global Carbon Budget (Version 2.3, issued June 2014)*. Tech. rep. Carbon Dioxide Information Analysis Center (CDIAC), Oak Ridge National ...

Le Quéré, Corinne et al. (2015). “Global carbon budget 2015”. In: *Earth System Science Data* 7, pp. 349–396.

Lee, Jung-Eun et al. (2013). “Forest productivity and water stress in Amazonia: Observations from GOSAT chlorophyll fluorescence”. In: *Proceedings of the Royal Society B: Biological Sciences* 280.1761, p. 20130171.

Lei, LiPing et al. (2014). “A comparison of atmospheric CO2 concentration GOSAT-based observations and model simulations”. In: *Science China. Earth Sciences* 57.6, p. 1393.

Li, Xing et al. (2018). “Solar-induced chlorophyll fluorescence is strongly correlated with terrestrial photosynthesis for a wide variety of biomes: First global analysis based on OCO-2 and flux tower observations”. In: *Global change biology* 24.9, pp. 3990–4008.

Liang, Ailin et al. (2017). “Comparison of Satellite-Observed XCO2 from GOSAT, OCO-2, and Ground-Based TCCON”. In: *Remote Sensing* 9.10, p. 1033.

Lin, JC et al. (2011). “Attributing uncertainties in simulated biospheric carbon fluxes to different error sources”. In: *Global Biogeochemical Cycles* 25.2.

Lindqvist, Hannakaisa et al. (2015). "Does GOSAT capture the true seasonal cycle of carbon dioxide?" In:

Lindsey, Rebecca (2009). "Climate and Earth's energy budget". In: *NASA Earth Observatory, Greenbelt, MD, accessed Oct* 9, p. 2017.

Liu, Junjie et al. (2017). "Contrasting carbon cycle responses of the tropical continents to the 2015–2016 El Niño". In: *Science* 358.6360, eaam5690.

Liu, LiXin et al. (2009). "The characteristics of atmospheric CO 2 concentration variation of four national background stations in China". In: *Science in China Series D: Earth Sciences* 52.11, pp. 1857–1863.

Lloyd, John and JA Taylor (1994). "On the temperature dependence of soil respiration". In: *Functional ecology*, pp. 315–323.

Lopes, Aline Pontes et al. (2016). "Leaf flush drives dry season green-up of the Central Amazon". In: *Remote Sensing of Environment* 182, pp. 90–98.

Luus, KA et al. (2017). "Tundra photosynthesis captured by satellite-observed solar-induced chlorophyll fluorescence". In: *Geophysical Research Letters* 44.3, pp. 1564–1573.

Maheras, P, Elena Xoplaki, and Haim Kutiel (1999). "Wet and dry monthly anomalies across the Mediterranean basin and their relationship with circulation, 1860–1990". In: *Theoretical and Applied Climatology* 64.3-4, pp. 189–199.

Maksyutov, S et al. (2013). "Regional CO2 flux estimates for 2009-2010 based on GOSAT and ground-based CO2 observations". In: *Atmospheric Chemistry and Physics* 13.18, pp. 9351–9373.

Malhi, Yadvinder and James Wright (2004). "Spatial patterns and recent trends in the climate of tropical rainforest regions". In: *Philosophical Transactions of the Royal Society B: Biological Sciences* 359.1443, pp. 311–329.

Malhi, Yadvinder et al. (2013). "African rainforests: past, present and future". In: *Philosophical Transactions of the Royal Society B: Biological Sciences* 368.1625, p. 20120312. DOI: `10.1098/rstb.2012.0312`.

Martiny, Nadège et al. (2006). "Compared regimes of NDVI and rainfall in semiarid regions of Africa". In: *International Journal of Remote Sensing* 27.23, pp. 5201–5223.

Mascorro, Vanessa S et al. (2015). "Choice of satellite imagery and attribution of changes to disturbance type strongly affects forest carbon balance estimates". In: *Carbon balance and management* 10.1, p. 30.

Mengistu, A. G. and G. Mengistu Tsidu (2018). "Comparison of CO2 from NOAA Carbon Tracker reanalysis model and satellites over Africa". In: *Atmospheric*

Measurement Techniques Discussions 2018, pp. 1–31. DOI: `10.5194/amt-2018-84`.

Mengistu, A. G. and G. Mengistu Tsidu (2019). "On the performance of satellite-based observations of XCO2 in capturing the NOAA Carbon Tracker model and ground-based flask observations over Africa land mass". In: *Atmospheric Measurement Techniques Discussions* 2019, pp. 1–33. DOI: `10.5194/amt-2019-390`.

Mengistu Tsidu, G. (2012). "High-resolution monthly rainfall database for Ethiopia: Homogenization, reconstruction, and gridding". In: *Journal of Climate* 25.24, pp. 8422–8443.

Mengistu Tsidu, G., T. Blumenstock, and F. Hase (2015). "Observations of precipitable water vapour over complex topography of Ethiopia from ground-based GPS, FTIR, radiosonde and ERA-Interim reanalysis". In: *Atmospheric Measurement Techniques* 8.8, p. 3277.

Mengistu Tsidu, Gizaw (2017). "Secular spring rainfall variability at local scale over Ethiopia: trend and associated dynamics". In: *Theoretical and Applied Climatology* 130.1-2, pp. 91–106.

Menon, Surabi et al. (2007). *Couplings between changes in the climate system and biogeochemistry*. Tech. rep. Ernest Orlando Lawrence Berkeley National Laboratory, Berkeley, CA (US).

Mercado, Lina et al. (2006). "Modelling Amazonian forest eddy covariance data: a comparison of big leaf versus sun/shade models for the C-14 tower at Manaus I. Canopy photosynthesis". In: *Acta Amazonica* 36.1, pp. 69–82.

Michalak, Anna M et al. (2011). *A US carbon cycle science plan*. Citeseer.

Mitchell, Todd (2001). *Africa Rainfall Climatology. University of Washington*.

Monteith, JL (1972). "Solar radiation and productivity in tropical ecosystems". In: *Journal of applied ecology* 9.3, pp. 747–766.

Morino, I et al. (2010). "Preliminary validation of column-averaged volume mixing ratios of carbon dioxide and methane retrieved from GOSAT short-wavelength infrared spectra". In:

Munro, Rosemary et al. (2006). "GOME-2 on MetOp". In: *Proc. of The 2006 EUMETSAT Meteorological Satellite Conference, Helsinki, Finland*. Vol. 1216, p. 48.

Murray, James W et al. (1994). "Physical and biological controls on carbon cycling in the equatorial Pacific". In: *Science* 266.5182, pp. 58–65.

Mutai, Charles C and M Neil Ward (2000). "East African rainfall and the tropical circulation/convection on intraseasonal to interannual timescales". In: *Journal of Climate* 13.22, pp. 3915–3939.

Myneni, Ranga B et al. (1997). "Increased plant growth in the northern high latitudes from 1981 to 1991". In: *Nature* 386.6626, p. 698.

Nayak, RK et al. (2014). "Evaluation of NOAA Carbon Tracker Global Carbon Dioxide Products". In: *The International Archives of Photogrammetry, Remote Sensing and Spatial Information Sciences* 40.8, p. 287.

Nemani, Ramakrishna R et al. (2003). "Climate-driven increases in global terrestrial net primary production from 1982 to 1999". In: *science* 300.5625, pp. 1560–1563.

Nemry, B et al. (1996). "The seasonality of the CO2 exchange between the atmosphere and the land biosphere: a study with a global mechanistic vegetation model". In: *Journal of Geophysical Research: Atmospheres* 101.D3, pp. 7111–7125.

Ngomanda, Alfred et al. (2009). "Seasonality change and the third millennium BP rainforest crisis in southern Cameroon (Central Africa)". In: *Quaternary Research* 71.3, pp. 307–318.

Nicholson, Sharon E and JC Selato (2000). "The influence of La Nina on African rainfall". In: *International Journal of Climatology: A Journal of the Royal Meteorological Society* 20.14, pp. 1761–1776.

NIES GOSAT Project, : (2012). "Summary of the GOSAT Level 2 data Products Validation Activity". In: *Center for Global Environmental Research*, pp. 1–10.

Norton, Alexander J et al. (2018). "Estimating global gross primary productivity using chlorophyll fluorescence and a data assimilation system with the BETHY-SCOPE model". In: *Biogeosciences Discussions*, pp. 1–40.

Nydahl, Anna, Satya Panigrahi, and Johan Wikner (2013). "Increased microbial activity in a warmer and wetter climate enhances the risk of coastal hypoxia". In: *FEMS microbiology ecology* 85.2, pp. 338–347.

O'Dell, Christopher et al. (2018). "Improved retrievals of carbon dioxide from Orbiting Carbon Observatory-2 with the version 8 ACOS algorithm". In:

O'Dell, CW et al. (2012). "The ACOS CO 2 retrieval algorithm-Part 1: Description and validation against synthetic observations". In:

Olsen, Seth C and James T Randerson (2004). "Differences between surface and column atmospheric CO2 and implications for carbon cycle research". In: *Journal of Geophysical Research: Atmospheres* 109.D2.

Pacala, Stephen et al. (2007). "The North American carbon budget past and present". In: *In: King, AW; Dilling, L.; Zimmerman, GP; Fairman, DM; Houghton, RA; Marland, G.; Rose, AZ; Wilbanks, TJ, eds. The First State of the Carbon Cycle Report (SOCCR): The North American Carbon Budget and Implications for the*

Global Carbon Cycle. National Oceanic and Atmospheric Administration, National Climatic Data Center, Asheville, NC: 29-36, 167-170.

Page, Y Le et al. (2008). "Global fire activity patterns (1996–2006) and climatic influence: an analysis using the World Fire Atlas". In: *Atmospheric Chemistry and Physics* 8.7, pp. 1911–1924.

Palmer, Paul I et al. (2019). "Net carbon emissions from African biosphere dominate pan-tropical atmospheric CO 2 signal". In: *Nature communications* 10.1, pp. 1–9.

Patra, Prabir K et al. (2017). "The Orbiting Carbon Observatory (OCO-2) tracks 2–3 peta-gram increase in carbon release to the atmosphere during the 2014–2016 El Niño". In: *Scientific reports* 7.1, p. 13567.

Peters, Glen P et al. (2012). "Rapid growth in CO 2 emissions after the 2008–2009 global financial crisis". In: *Nature Climate Change* 2.1, p. 2.

Peters, W et al. (2005). "An ensemble data assimilation system to estimate CO2 surface fluxes from atmospheric trace gas observations". In: *Journal of Geophysical Research: Atmospheres* 110.D24. DOI: `10.1029/2005JD006157`.

Peters, Wouter et al. (2007). "An atmospheric perspective on North American carbon dioxide exchange: CarbonTracker". In: *Proceedings of the National Academy of Sciences* 104.48, pp. 18925–18930.

Peters-Lidard, Christa D et al. (2007). "High-performance Earth system modeling with NASA/GSFC's Land Information System". In: *Innovations in Systems and Software Engineering* 3.3, pp. 157–165.

Peylin, P et al. (2013). "Global atmospheric carbon budget: results from an ensemble of atmospheric CO2 inversions". In: *Biogeosciences* 10, pp. 6699–6720.

Philippon, Nathalie et al. (2007). "Characterization of the interannual and intraseasonal variability of West African vegetation between 1982 and 2002 by means of NOAA AVHRR NDVI data". In: *Journal of Climate* 20.7, pp. 1202–1218.

Piao, Shilong et al. (2013). "Evaluation of terrestrial carbon cycle models for their response to climate variability and to CO2 trends". In: *Global Change Biology* 19.7, pp. 2117–2132.

Plisnier, PD, S Serneels, and EF Lambin (2000). "Impact of ENSO on East African ecosystems: a multivariate analysis based on climate and remote sensing data". In: *Global Ecology and Biogeography* 9.6, pp. 481–497.

Pomposi, Catherine et al. (2018). "Distinguishing southern Africa precipitation response by strength of El Nino events and implications for decision-making". In: *Environmental Research Letters* 13.7, p. 074015.

Porcar-Castell, Albert et al. (2014). "Linking chlorophyll a fluorescence to photosynthesis for remote sensing applications: mechanisms and challenges". In: *Journal of experimental botany* 65.15, pp. 4065–4095.

Prather, Michael J, Christopher D Holmes, and Juno Hsu (2012). "Reactive greenhouse gas scenarios: Systematic exploration of uncertainties and the role of atmospheric chemistry". In: *Geophysical Research Letters* 39.9.

Prentice, IC et al. (2001). "The carbon cycle and atmospheric carbon dioxide. p. 182–237. JT Houghton et al.(ed.) Climate change 2001: The scientific basis. Contribution of Working Group I to the Third Assessment Report of the Intergovernmental Panel on Climate Change. Cambridge Univ. Press, Cambridge, UK." In: *The carbon cycle and atmospheric carbon dioxide. p. 182–237. In JT Houghton et al.(ed.) Climate change 2001: The scientific basis. Contribution of Working Group I to the Third Assessment Report of the Intergovernmental Panel on Climate Change. Cambridge Univ. Press, Cambridge, UK.*

Propastin, Pavel (2009). "Monitoring system for assessment of vegetation sensitivity to El-Nino over Africa". In: *Advances in GIScience*. Springer, pp. 329–344.

Pumphrey, Hugh C et al. (2018). "MLS measurements of stratospheric hydrogen cyanide during the 2015-2016 El Nino event". In: *Atmospheric Chemistry and Physics* 18.2.

Quéré, C Le et al. (2015). "Global carbon budget 2015". In: *Earth System Science Data* 7.2, pp. 349–396.

Raupach, Michael R et al. (2007). "Global and regional drivers of accelerating CO2 emissions". In: *Proceedings of the National Academy of Sciences* 104.24, pp. 10288–10293.

Rayner, PJ and DM O'Brien (2001). "The utility of remotely sensed CO2 concentration data in surface source inversions". In: *Geophysical research letters* 28.1, pp. 175–178.

Reichstein, Markus et al. (2005). "On the separation of net ecosystem exchange into assimilation and ecosystem respiration: review and improved algorithm". In: *Global change biology* 11.9, pp. 1424–1439.

Restrepo-Coupe, Natalia et al. (2013). "What drives the seasonality of photosynthesis across the Amazon basin? A cross-site analysis of eddy flux tower measurements from the Brasil flux network". In: *Agricultural and Forest Meteorology* 182, pp. 128–144.

Restrepo-Coupe, Natalia et al. (2017). "Do dynamic global vegetation models capture the seasonality of carbon fluxes in the Amazon basin? A data-model intercomparison". In: *Global change biology* 23.1, pp. 191–208.

Richardson, Mark (2013). "Comment on "The phase relation between atmospheric carbon dioxide and global temperature" by Humlum, Stordahl and Solheim". In: *Global and planetary change* 107, pp. 226–228.

Rodgers, Clive D (2000). *Inverse methods for atmospheric sounding: theory and practice*. Vol. 2. World scientific.

Rodgers, Clive D and Brian J Connor (2003). "Intercomparison of remote sounding instruments". In: *Journal of Geophysical Research: Atmospheres* 108.D3.

Sabine, Christopher L et al. (2004). "Current status and past trends of the global carbon cycle". In: *Scope-scientific committee on problems of the environment international council of scientific unions* 62, pp. 17–44.

Saeki, T et al. (2013). "Inverse modeling of CO2 fluxes using GOSAT data and multi-year ground-based observations". In: *Sola* 9, pp. 45–50.

Saitoh, Naoko et al. (2009). "CO2 retrieval algorithm for the thermal infrared spectra of the Greenhouse Gases Observing Satellite: Potential of retrieving CO2 vertical profile from high-resolution FTS sensor". In: *Journal of Geophysical Research: Atmospheres* 114.D17.

Sanders, Abram et al. (2016). "Spaceborne sun-induced vegetation fluorescence time series from 2007 to 2015 evaluated with Australian flux tower measurements". In: *Remote Sensing* 8.11, p. 895.

Santer, Benjamin D et al. (2013). "Human and natural influences on the changing thermal structure of the atmosphere". In: *Proceedings of the National Academy of Sciences* 110.43, pp. 17235–17240.

Sayer, AM et al. (2014). "MODIS Collection 6 aerosol products: Comparison between Aqua's e-Deep Blue, Dark Target, and "merged" data sets, and usage recommendations". In: *Journal of Geophysical Research: Atmospheres* 119.24, pp. 13–965.

Schaaf, C. and Z. Wang (2015). *MCD43C4 MODIS/Terra+Aqua BRDF/Albedo Nadir BRDF-Adjusted Ref Daily L3 Global 0.05Deg CMG V006 [Data set]. NASA EOSDIS Land Processes DAAC. Accessed 2019-02-12.* `https://doi.org/10.5067/MODIS/MCD43C4.006`.

Schaik, E. van et al. (2020). "Improved SIFTER v2 algorithm for long-term GOME-2A satellite retrievals of fluorescence with a correction for instrument degradation". In: *Atmospheric Measurement Techniques Discussions* 2020, pp. 1–33. DOI: `10.5194/amt-2019-384`. URL: `https://www.atmos-meas-tech-discuss.net/amt-2019-384/`.

Schimel, David et al. (2015). "Observing terrestrial ecosystems and the carbon cycle from space". In: *Global Change Biology* 21.5, pp. 1762–1776.

Schlau-Cohen, Gabriela S and Joseph Berry (2015). “Photosynthetic fluorescence, from molecule to planet”. In: *Physics Today* 68.66.

Sheffield, Justin and Eric F Wood (2008). “Global trends and variability in soil moisture and drought characteristics, 1950–2000, from observation-driven simulations of the terrestrial hydrologic cycle”. In: *Journal of Climate* 21.3, pp. 432–458. DOI: `10.1175/2007JCLI1822.1`.

Siegenthaler, U and Jorge Louis Sarmiento (1993). “Atmospheric carbon dioxide and the ocean”. In: *Nature* 365.6442, p. 119.

Smith, Pete et al. (2008). “Impact of global warming on soil organic carbon”. In: *Advances in agronomy* 97, pp. 1–43.

Stephenson, Nathan L (1990). “Climatic control of vegetation distribution: the role of the water balance”. In: *The American Naturalist* 135.5, pp. 649–670.

Stocker, Benjamin D et al. (2013). “Multiple greenhouse-gas feedbacks from the land biosphere under future climate change scenarios”. In: *Nature Climate Change* 3.7, pp. 666–672.

Stocker, Benjamin D et al. (2018). “Quantifying soil moisture impacts on light use efficiency across biomes”. In: *New Phytologist* 218.4, pp. 1430–1449. DOI: `10.1111/nph.15123`.

Stocker, Benjamin D et al. (2019). “Drought impacts on terrestrial primary production underestimated by satellite monitoring”. In: *Nature Geoscience* 12.4, pp. 264–270.

Sun, Ying et al. (2017). “OCO-2 advances photosynthesis observation from space via solar-induced chlorophyll fluorescence”. In: *Science* 358.6360, eaam5747.

Sundquist, Eric T (1993). “The global carbon dioxide budget”. In: *Science*, pp. 934–941.

Takahashi, Taro et al. (2003). “Decadal variation of the surface water pCO2 in the western and central equatorial Pacific”. In: *Science* 302.5646, pp. 852–856.

Tang, Hao and Ralph Dubayah (2017). “Light-driven growth in Amazon evergreen forests explained by seasonal variations of vertical canopy structure”. In: *Proceedings of the National Academy of Sciences* 114.10, pp. 2640–2644.

Taylor, Karl E (2001). “Summarizing multiple aspects of model performance in a single diagram”. In: *Journal of Geophysical Research: Atmospheres* 106.D7, pp. 7183–7192.

Taylor, Karl E, Ronald J Stouffer, and Gerald A Meehl (2012). “An overview of CMIP5 and the experiment design”. In: *Bulletin of the American Meteorological Society* 93.4, pp. 485–498. DOI: `10.1175/BAMS-D-11-00094.1`.

Teskey, Robert et al. (2015). “Responses of tree species to heat waves and extreme heat events”. In: *Plant, cell & environment* 38.9, pp. 1699–1712.

Tian, Feng et al. (2020). "Exceptional Drought across Southeastern Australia Caused by Extreme Lack of Precipitation and Its Impacts on NDVI and SIF in 2018". In: *Remote Sensing* 12.1, p. 54.

Trenberth, Kevin E and Timothy J Hoar (1996). "The 1990–1995 El Niño-southern oscillation event: longest on record". In: *Geophysical research letters* 23.1, pp. 57–60.

Trenberth, Kevin E et al. (1998). "Progress during TOGA in understanding and modeling global teleconnections associated with tropical sea surface temperatures". In: *Journal of Geophysical Research: Oceans* 103.C7, pp. 14291–14324.

Trenberth, Kevin E et al. (2002). "Evolution of El Niño–Southern Oscillation and global atmospheric surface temperatures". In: *Journal of Geophysical Research: Atmospheres* 107.D8, AAC–5.

Tsutsumi, Yukitomo et al. (2006). "Long-term trends of greenhouse gases in regional and background events observed during 1998–2004 at Yonagunijima located to the east of the Asian continent". In: *Atmospheric Environment* 40.30, pp. 5868–5879.

Tucker, Compton J (1979). "Red and photographic infrared linear combinations for monitoring vegetation". In: *Remote sensing of Environment* 8.2, pp. 127–150.

Turner, Alexander J et al. (2019). "A double peak in the seasonality of California's photosynthesis as observed from space". In: *Biogeosciences Discussions*, pp. 1–27.

Velazco, Voltaire A et al. (2017). "Total carbon column observing network Philippines: Toward quantifying atmospheric carbon in southeast asia". In: DOI: `10.18783/cddj.v002.i02.a01`.

Vermote, EF et al. (1997). "Atmospheric correction of visible to middle-infrared EOS-MODIS data over land surfaces: Background, operational algorithm and validation". In: *Journal of Geophysical Research: Atmospheres* 102.D14, pp. 17131–17141.

Vincens, Annie, Yannick Garcin, and Guillaume Buchet (2007). "Influence of rainfall seasonality on African lowland vegetation during the Late Quaternary: pollen evidence from Lake Masoko, Tanzania". In: *Journal of Biogeography* 34.7, pp. 1274–1288.

Wang, Jun, Ning Zeng, and Meirong Wang (2016). "Interannual variability of the atmospheric CO 2 growth rate: roles of precipitation and temperature". In: *Biogeosciences* 13.8, pp. 2339–2352.

Wang, Jun et al. (2018). “Contrasting interannual atmospheric CO 2 variabilities and their terrestrial mechanisms for two types of El Niños”. In: *Atmospheric Chemistry and Physics* 18.14, pp. 10333–10345.

Wang, Weile et al. (2013). “Variations in atmospheric CO2 growth rates coupled with tropical temperature”. In: *Proceedings of the National Academy of Sciences* 110.32, pp. 13061–13066.

Wang, Xuhui et al. (2014). “A two-fold increase of carbon cycle sensitivity to tropical temperature variations”. In: *Nature* 506.7487, p. 212.

Werf, Guido R Van der et al. (2010). “Global fire emissions and the contribution of deforestation, savanna, forest, agricultural, and peat fires (1997–2009)”. In: *Atmospheric chemistry and physics* 10.23, pp. 11707–11735.

Wigley, TML (2000). “ENSO, volcanoes and record-breaking temperatures”. In: *Geophysical Research Letters* 27.24, pp. 4101–4104.

Williams, CA et al. (2007). *Africa and global carbon cycle, Carbon Balance and Manag., 2 (3), 1–13.*

Wolff, Christian et al. (2011). “Reduced interannual rainfall variability in East Africa during the last ice age”. In: *Science* 333.6043, pp. 743–747.

Wu, Xiuchen et al. (2016). “Seasonal divergence in the interannual responses of Northern Hemisphere vegetation activity to variations in diurnal climate”. In: *Scientific reports* 6, p. 19000. DOI: `10.1038/srep19000`.

Wu, Zhaohua and Norden E Huang (2004). “A study of the characteristics of white noise using the empirical mode decomposition method”. In: *Proceedings of the Royal Society of London A: Mathematical, Physical and Engineering Sciences*. Vol. 460. 2046. The Royal Society, pp. 1597–1611.

— (2005). “Statistical significance test of intrinsic mode functions”. In: *Hilbert-Huang Transform and its applications*. World Scientific, pp. 107–127.

— (2009). “Ensemble empirical mode decomposition: a noise-assisted data analysis method”. In: *Advances in adaptive data analysis* 1.01, pp. 1–41.

Wunch, D et al. (2011). “A method for evaluating bias in global measurements of CO 2 total columns from space”. In: *Atmospheric Chemistry and Physics* 11.23, pp. 12317–12337.

Xiao, Xiangming et al. (2005). “Modeling gross primary production of an evergreen needleleaf forest using MODIS and climate data”. In: *Ecological Applications* 15.3, pp. 954–969.

Xiao, Xiangming et al. (2006). “Detecting leaf phenology of seasonally moist tropical forests in South America with multi-temporal MODIS images”. In: *Remote Sensing of Environment* 103.4, pp. 465–473.

Yan, Zhifeng et al. (2018). “A moisture function of soil heterotrophic respiration that incorporates microscale processes”. In: *Nature communications* 9.1, pp. 1–10. DOI: `10.1038/s41467-018-04971-6`.

Yokota, T et al. (2009). “Global concentrations of CO2 and CH4 retrieved from GOSAT: First preliminary results”. In: *Sola* 5, pp. 160–163.

Yokota, Yasuhiro et al. (2011). “Lunar photometric properties at wavelengths 0.5–1.6 μm acquired by SELENE Spectral Profiler and their dependency on local albedo and latitudinal zones”. In: *Icarus* 215.2, pp. 639–660.

Yoshida, Y et al. (2011). “Retrieval algorithm for CO2 and CH4 column abundances from short-wavelength infrared spectral observations by the Greenhouse gases observing satellite”. In: *Atmospheric Measurement Techniques* 4.4, p. 717.

Yoshida, Y et al. (2013). “Improvement of the retrieval algorithm for GOSAT SWIR XCO2 and XCH4 and their validation using TCCON data”. In:

Zarco-Tejada, Pablo J et al. (2000). “Chlorophyll fluorescence effects on vegetation apparent reflectance: I. Leaf-level measurements and model simulation”. In: *Remote Sensing of Environment* 74.3, pp. 582–595.

Zeng, Yelu et al. (2019). “A practical approach for estimating the escape ratio of near-infrared solar-induced chlorophyll fluorescence”. In: *Remote Sensing of Environment* 232, p. 111209.

Zhang, Linjing, Hong Jiang, and Xiuying Zhang (2015). “Comparison analysis of the global carbon dioxide concentration column derived from SCIAMACHY, AIRS, and GOSAT with surface station measurements”. In: *International Journal of Remote Sensing* 36.5, pp. 1406–1423.

Zhang, Quan et al. (2018a). “Changes in photosynthesis and soil moisture drive the seasonal soil respiration-temperature hysteresis relationship”. In: *Agricultural and Forest Meteorology* 259, pp. 184–195. DOI: `10.1016/j.agrformet.2018.05.005`.

Zhang, Xuanze et al. (2018b). “Dominant regions and drivers of the variability of the global land carbon sink across timescales”. In: *Global change biology*.

Zhang, Zhen et al. (2018c). “Enhanced response of global wetland methane emissions to the 2015–2016 El Nino-Southern Oscillation event”. In: *Environmental Research Letters* 13.7, p. 074009.

Zhou, Tao et al. (2008). “Links between global CO 2 variability and climate anomalies of biomes”. In: *Science in China Series D: Earth Sciences* 51.5, pp. 740–747.

Zhu, Chunmei, Tereza Cavazos, and Dennis P Lettenmaier (2007). "Role of antecedent land surface conditions in warm season precipitation over northwestern Mexico". In: *Journal of Climate* 20.9, pp. 1774–1791. DOI: `10.1175/JCLI4085.1`.

Zimov, SA et al. (1999). "Contribution of disturbance to increasing seasonal amplitude of atmospheric CO2". In: *Science* 284.5422, pp. 1973–1976.